ORNL/SPR-2020/1940

Progression to Compatibility Evaluations in Flowing Molten Salts

Bruce A. Pint

July 2020

Approved for public release.
Distribution is unlimited.

OAK RIDGE NATIONAL LABORATORY
MANAGED BY UT-BATTELLE FOR THE US DEPARTMENT OF ENERGY

ORNL/SPR-2020/1940

Solar Energy Technology Office

PROGRESSION TO COMPATIBILITY EVALUATIONS IN FLOWING MOLTEN SALTS

Bruce A. Pint

Date Published:

July 2020

Prepared by
OAK RIDGE NATIONAL LABORATORY
Oak Ridge, TN 37831-6283
managed by
UT-BATTELLE, LLC
for the
US DEPARTMENT OF ENERGY
under contract DE-AC05-00OR22725

Final Technical Report (FTR)

Project Title: Progression to Compatibility Evaluations in Flowing Molten Salts

Project Period: 2/01/18 – 1/31/20

Submission Date: 6/25/2020

Recipient: Oak Ridge National Laboratory

Address: 1 Bethel Valley Rd.
Oak Ridge, TN 37831-6156

Website (if available) www.ornl.gov

Award Number: CPS 33873

Project Team: Oak Ridge National Laboratory

Principal Investigator: Bruce A. Pint, Distinguished Research Staff
Phone: 865-576-2897
Email: pintba@ornl.gov

Business Contact: Dominic F. Lee, Program Manager
Phone: 865-241-0775
Email: leedf@ornl.gov

Technology Manager: Levi Irwin

Project Officer: Christine Bing

Progression to Compatibility Evaluations in Flowing Molten Salts

Executive Summary

Molten salt compatibility with structural alloys has been identified as a key issue for the development of Generation 3 concentrating solar power (CSP) systems with thermal storage. To accelerate this evaluation to pumped systems, the goal of this project was to conduct thermal convection loop (TCL) experiments with a peak temperature of ≥700°C and a typical temperature gradient of ~100°C. The experiments indicated that conventional ~16wt.%Cr Ni-based alloys are compatible up to 700°C with purified (i.e. low O) or dried (low H_2O) industrial-sourced Mg-K-Na chloride salt with <10 µm/yr loss.

This two-year project was conducted based on the experimental and mechanistic understanding developed more than 60 years ago at Oak Ridge National Laboratory (ORNL). The first TCL experiment met the <15 µm/yr corrosion metric for this project with specimens of Ni-based alloy 600 exposed at 580°-700°C for 1000 h and post-exposure room temperature tensile tests showed minimal degradation. The second TCL experiment successfully deployed an electrochemical sensor from Argonne National Laboratory and had a peak temperature of 750°C but only ran for ~110 h due to a furnace failure. Both experiments used highly purified industrial-sourced salt with an O content of ~3 µg O/g salt and a Mg addition of 0.04 wt.%. In the second year, the Chloride Collective developed a more economical drying procedure such that the O content was much higher (>20,000 µg O/g salt). A third TCL experiment was conducted with a sensor and a peak temperature of 700°C using dried salt from the same industrial source and increased NaCl content (~20 wt.%). In addition to a 0.05% Mg addition to the salt, a Mg coupon was added in the coldest part of the loop which dissolved during the experiment. Again, small mass changes were noted for specimens of alloys 600 and C276 but the values were slightly higher than those measured in purified salt with Mg. A thin non-continuous and non-adherent oxide layer was deposited on most specimens containing Mg, Si and Al but Cr depletion also was observed.

Both years included facilities qualification crucible experiments and then capsule experiments to confirm a baseline isothermal reaction rate. The first year capsule experiment led to the conclusion that the two-stage ORNL purification process using NH_4Cl and CCl_4 left the salt with a high Cl potential and a Mg addition (~0.05wt.%) was needed to lower the potential. The second year capsule experiments at 600° and 700°C found little difference in depth of attack for 0-0.25%Mg additions. In general, the complex reactions where salt can be trapped in the porous surface layer of metal indicated that mass change is an unreliable metric and average depth of Cr depletion is a better metric for assessing the extent of attack.

These results have created a new baseline that is contrary to the recent published literature for chloride salts where mass losses have been reported that can be extrapolated to very significant annual metal loss rates. Chloride salt corrosion can be controlled and the results also indicate that salt purification to low O levels may not be necessary. However, additional TCL experiments are needed at different times and temperatures to generate important engineering information such as temperature dependent corrosion rates and reaction rate laws for extrapolation to long-term behavior and isolate the effect of salt additives and impurities.

Table of Contents

Background

Several key points should be made to understand the philosophy behind the approach to this project. The first is that the molten salt research community collapsed several decades ago. While this may be difficult for non-experts to perceive or appreciate, what this unfortunately means is that there are no current standards for molten salt experimental work, there are very few people with formal training in molten salt research standard practices, and there are no journals with obvious editorial expertise in this area. Thus, much of the research is misguided with low quality and the status of molten salts in the 2017 CSP Generation 3 roadmap is not surprising. Most importantly, the roadmap has no discussion about moving to a flowing salt experiment, which has long been the ultimate test for molten salt compatibility [Susskind 1960, DeVan 1979, Keiser 1979, Bradshaw 1987]. Like liquid metals, molten salts represent a unique form of corrosion, which is better described as compatibility or limited (i.e. acceptable) interaction/degradation. The goal is to identify structural materials, claddings or coatings that are compatible for extended periods with molten salts such that they can operate as required. Molten salts don't operate in a quartz capsule or in an electrochemical cell. They flow within structural components with a temperature gradient. A major concern with liquid metals or salts is dissolution and solubility affects the rate of dissolution. For molten salts, oxidation of conventional alloying elements like Cr, Al, Ti and Mn leads to their selective removal from the containing material unless highly reducing conditions are maintained, i.e. low impurity levels of O_2 and H_2O [DeVan 1979]. If impurities cannot be controlled in a commercial process, then it may not be possible to deploy a chloride salt.

The ORNL paradigm for molten salt compatibility revolves around several fundamental concepts:

1. Salts must be purified to achieve good compatibility, HF was used for fluoride salts but a similar process with HCl for chloride salts has not been found
2. Once purified, impurity ingress must be eliminated during experiments by welding shut capsules and evacuating a thermal convection loop (TCL) prior to operation
3. The Cl (or F) potential must be lowered to inhibit reaction with alloying elements in structural alloys such as Cr, Al, Ti and Mn.
4. Low Cr, Ni-base alloys provided the best compatibility among structural alloys in fluoride salts
5. Compatibility is affected by solubility of the diffusing species in the liquid, therefore, in an isothermal, static system the salt saturates with time slowing the reaction, preventing a relevant reaction rate from being determined and obviating the need for long static corrosion experiments
6. A temperature gradient is needed to assess the mass transfer behavior in a molten salt where dissolution can continue at the highest temperatures and precipitation can occur as the liquid cools and the solubility decreases.
7. The container in a molten salt experiment should either be inert to the salt (e.g. Mo) or the same material as the specimen to prevent unintended reactions.

These concepts are based on more than a decade of experience leading up to the Molten Salt Reactor Experiment at ORNL (Haubenreich 1970) where FLiBe was contained by Hastelloy N (Ni-7%Cr-16%Mo-4%Fe), an alloy that was specifically developed for this application. Unfortunately, the preliminary data to explicitly prove or demonstrate these points is not readily available and there are no specific criteria for "pure" salt. The older literature predominantly provides results for purified fluoride salts with Hastelloy N. It must also be acknowledged that for all of the expertise that was developed, it appears that no specific mechanism was ever clearly identified for the metal-salt reaction to specify, for example, how a Cr atom in the metal is transferred to the salt. The lack of mechanistic understanding has led to confusion about which parameters to control and sometimes makes it difficult to design experiments and interpret results. Ongoing research is attempting to improve that understanding.

It appears that some researchers do not believe that chloride salts need to be purified and/or make no effort to quantify the starting salt impurity levels [Vignarooban 2014, Gomez-Vidal 2017, Ding 2018, Sun 2018]. Alternatively, they may not have the ability or an understanding of how to purify these salts. Relatively few studies have reported in-depth details on salt purification methods in molten chloride salts as well as mass change data from capsule experiments where the ingress of impurities was prevented. Although not published in the open literature, James Ambrosek's Ph.D. dissertation [2011] details a comparison of several salt purification methods, including sparging with argon, an HCl sparge, a CCl_4 sparge, and contacting with Mg. It was found that Mg treatment and sparging with CCl_4 produced the best (i.e. lowest mass loss) results, and the Mg method was chosen due to its easier implementation. Susskind et al. [1960] contacted their salt that included Bi with trace amounts of Mg, U, and Zr to remove impurities. While Ambrosek found a simple Ar sparge to be less effective, Indacochea et al. [1999] reported low corrosion rates in Ar sparged chloride salts. ORNL has a strong advantage in that expertise in salt purification has been retained and passed along to a new generation of researchers and the current techniques are outlined in the report.

To understand the potential metal-salt reactions, thermodynamic calculations were conducted using FactSage (version 7.2, FactPS database) [Pint 2019]. Figure 1a shows the relative stability of some of the various metal chlorides of interest. The salt components KCl and NaCl are some of the most stable chlorides followed by $MgCl_2$, i.e. they have the most negative Gibbs energy relative to elements in the standard state. Some of the minor additions such as Al and Mn are next followed by Cr, which is expected to be selectively attacked and removed from alloys in contact with a chloride salt [Ding 2018, Sun 2018]. Some of the least stable chlorides are Ni and Mo. Based on Olander's analysis for fluoride salts [2002], a similar calculation was made for Cr solubility in $MgCl_2$, Figure 1b. While this may be simplistic (i.e. not considering a binary or ternary salt or the effect of impurities), it does indicate that the Cr solubility is increasing with temperature and relatively low. This change in solubility can drive mass transfer in a flowing system with a temperature gradient.

The isothermal solute driven Cr dissolution reaction should be governed by:

$$J_i = k\,(C^S_i - C_i) \qquad (1)$$

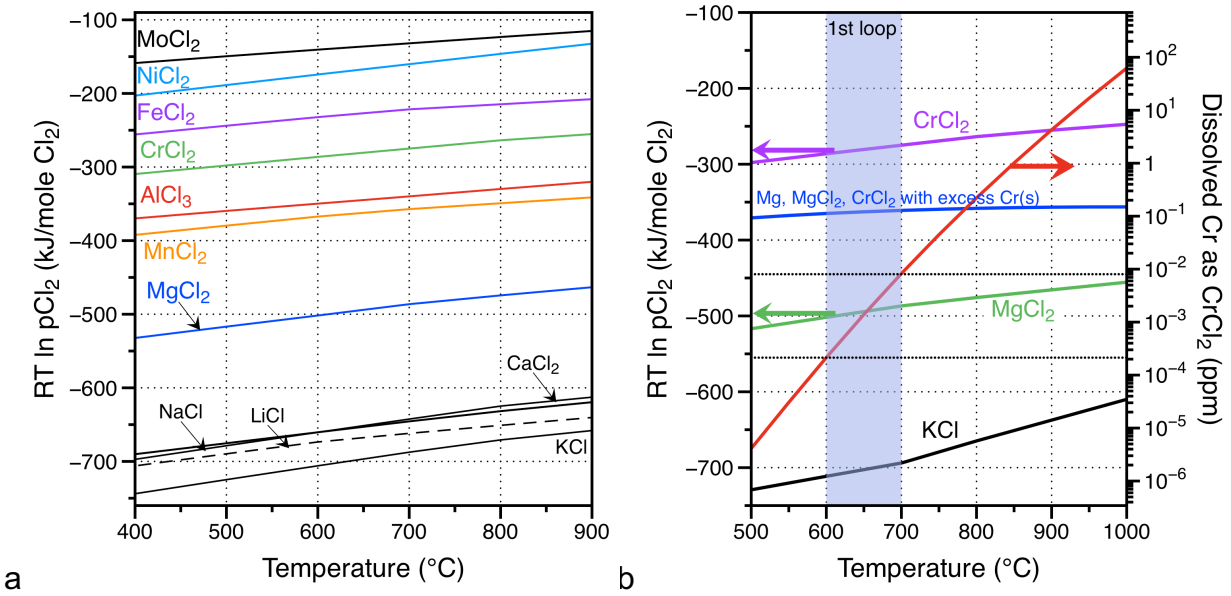

Figure 1 Thermodynamic calculations (a) Cl potential for various chlorides as a function of temperature and (b) equilibrium chlorine potential and equilibrium $CrCl_2$ activity (mole fraction) in a mixture of molten Mg, $CrCl_2$, and $MgCl_2$ using the ideal solution model and the reaction $Cr(s) + MgCl_2(l) = CrCl_2(l) + Mg(l)$.

where J_i is the flux of species i (e.g. Cr) into the liquid, k is a constant, C^S_i is the solubility limit of i in the liquid salt and C_i is the instantaneous concentration of i in the liquid [Epstein 1957, Tortorelli 1992]. Thus, as Cr dissolves into the liquid, the reaction should slow and stop as the liquid becomes saturated. This is the reason for specifying a preferred ratio of >10 between the salt volume and the specimen surface area in an isothermal capsule experiment with an inert container. A small ratio may cause quick saturation and a misleadingly small mass loss.

While measuring corrosion rates via electrochemical methods has been attempted [e.g., Vignarooban 2014], it does not appear that these data are easily relatable to more traditional mass change data from isothermal capsule or crucible “immersion” tests where the specimen is immersed in the salt for a specific period of time at an isothermal temperature. Figure 2a shows examples of the mass loss data from the literature, typically associated with the selective removal of Cr. Figure 2b shows recent data where there was little effect of measured alloy Cr content on the mass loss after 100 h at 700°C [Sun 2018]. If Cr is selectively removed, this result is difficult to explain.

While metrics are important scientific and project management tools, they must be well chosen. It is common to extrapolate these isothermal results and report an annualized rate of attack (i.e. μm/yr) as a performance metric [Vignarooban 2014, Ding 2018, Sun 2018]. That is inappropriate for several reasons: first, an assumption must be made about the kinetics and the assumption of a linear extrapolation is not based on any mechanistic understanding or data. Second, a review of the literature shows that most

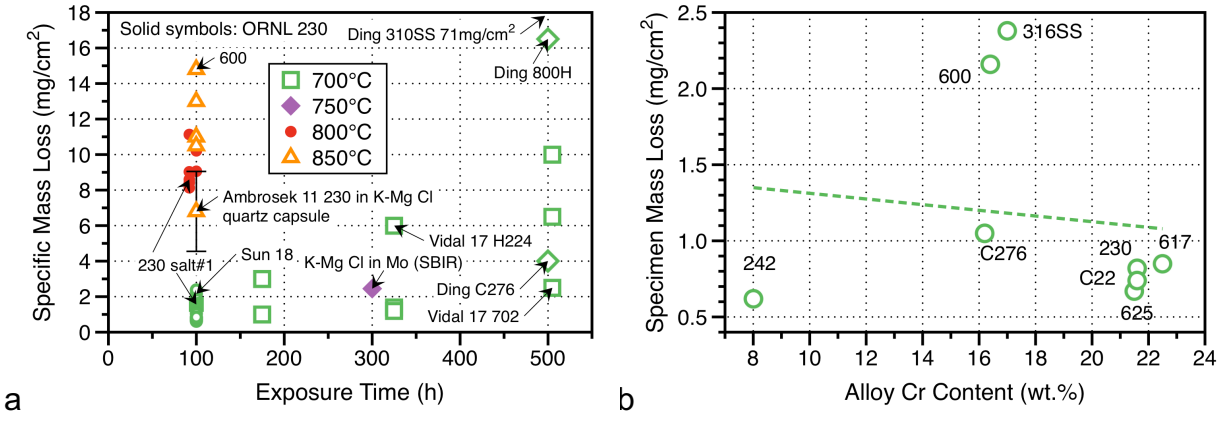

Figure 2. (a) Mass loss as a function of total exposure time for several chloride salt studies [Ambrosek 2011, Gomez-Vidal 2017, Ding 2018, Sun 2018, Raiman 2019] including some results from this study. (b) Mass loss after 100 h at 700°C [Sun 2018].

rates are calculated by using the alloy density and the mass loss data like that shown in Figure 2. However, as mentioned above, there is not uniform dissolution of the alloy, but rather selective attack of Cr so the behavior is much more complex. Third, when the specimens are characterized after salt exposure, it appears that salt or some type of M-O-Cl species (perhaps forming as a precursor to dissolution) is actually trapped in the porous sample. An example is shown in Figure 3. Thus, simple mass change is a poor metric for quantifying the extent of attack. Instead, affected alloy microstructure would be a much better parameter to assess the amount of attack.

If there is any question if Equation 1 is applicable, time series experiments show decreasing mass change or rate with increasing exposure time as the salt becomes

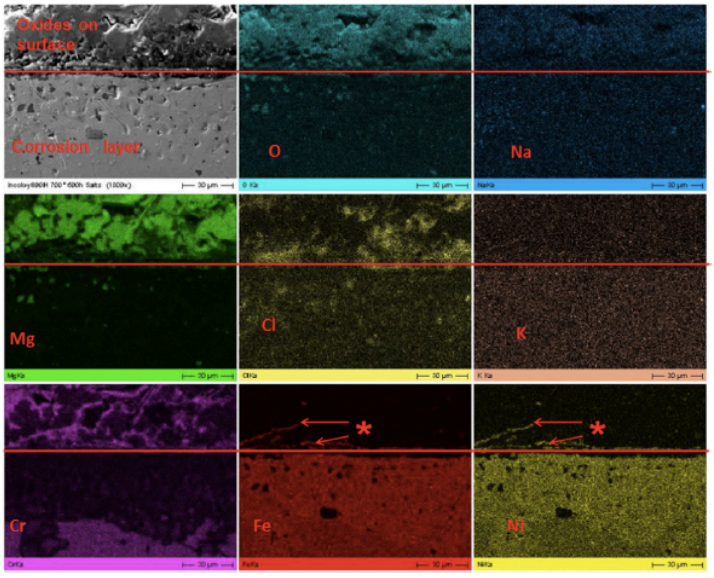

Figure 3. SEM/EDX maps of alloy 800H cross-section exposed for 500 h at 700°C in 60/20/20 Mg/K/Na salt [Ding 2018].

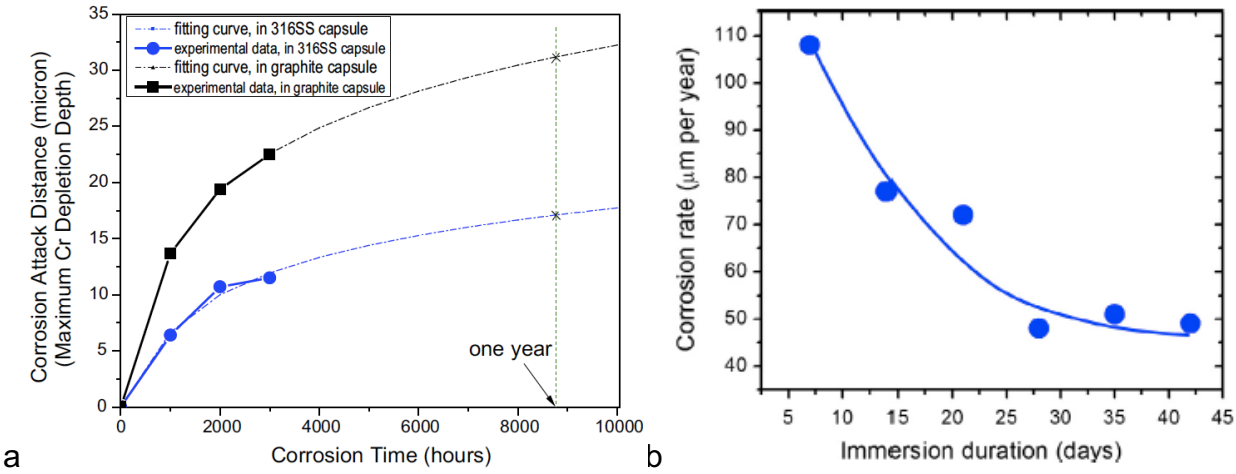

Figure 4. Literature examples showing decreasing (a) attack in FLiBe [Zheng 2018] or (b) rate in Zn-K-Na Cl salt at 500°C [Vignarooban 2014].

saturated, Figure 4. At a minimum, it must be concluded that linear extrapolations are incorrect. Furthermore, a recent analysis of the molten salt literature review concluded that purified salts and sealed containers had a significant effect on corrosion rates [Raiman 2018].

The ORNL paradigm derived from the MSRE is largely forgotten in the current literature. It is much more common to discuss molten salt results in terms of a conventional corrosion problem where a protective oxide is needed to protect the underlying alloy and the salt exposure is a form of hot corrosion [e.g. Ding 2018]. The thermodynamics in Figure 1a indicate that conventional protective oxides rich in Al or Cr are readily attacked by chloride salts and the protective oxide strategy has never been successful for flowing halide salts.

In summary,

1. Several groups are studying molten salt compatibility but most of the experiments are isothermal with low purity salt. The TCL work at ORNL will be an important step forward in understanding chloride salt compatibility.
2. Few groups have adequately studied salt chemistry and purification techniques in order to document the salt condition for their compatibility experiment or explain why that particular salt condition was used (other than expediency).
3. There appear to be significant gaps in understanding that remain, particularly in how alloy composition affects compatibility, particularly as the temperature increases to 800°C.
4. Another gap regards how salt chemistry affects compatibility and the interrelationship between impurities (e.g. O, H, S) and additives (i.e. Mg and Zr) including identifying the optimal salt as well as the most economical purification process.

Introduction

The first year of this project was designed to quickly transition from isothermal to flowing experiments. The first two tasks involved static experiments. Task 1.0 was the "facility qualification" test for all of the "Chloride Collective" consisting of ORNL, NREL and SRNL. Task 1.1 was to explore the conditions expected in the first flowing test (i.e. Ni-based alloy 600 at 600°-700°C). Task 1.2 was the first thermal convection loop (TCL) and Task 1.3 the second TCL, which was originally intended to include some type of corrosion mitigation but instead targeted a higher temperature and deploying a sensor.

In the second year of the project, the tasks were restructured to use the more economical salt drying process developed by the Chloride Collective and a higher Na content salt. Task 2.0 repeated the facility qualification experiment with new parameters and the new salt. Task 2.1 conducted capsule experiments with the dried salt to optimize the Mg addition and create a baseline for the flowing experiment. Task 2.2 was the third TCL experiment with a peak temperature of 700°C and a sensor.

Project Objective**:**

Molten salt compatibility with structural alloys has been identified as a key issue for the development of Generation 3 concentrated solar power (CSP) systems with thermal storage. To accelerate this evaluation to pumped systems, the goal of this project was to identify salt-alloy combinations that are sufficiently compatible in isothermal capsule tests and then conduct thermal convection loop (TCL) experiments with a peak temperature of ≥700°C and a typical temperature gradient of ~100°C. The second TCL deployed a sensor and had a peak temperature of 750°C. The third TCL experiment in Phase 2 used a different salt and a 700°C peak temperature with a sensor.

Tasks were broken down per the following:

- Task 1.0 Chloride corrosion facilities qualification
- Task 1.1 Capsule testing to support loop experiment
- Task 1.2 First thermal convection loop test
- Task 1.3 Second thermal convection loop test
- Task 2.0 Chloride corrosion facilities qualification
- Task 2.1 Capsule testing to support loop experiment
- Task 2.2 Third thermal convection loop test

Project Results and Discussion:

This section is broken down by task.

Task 1.0 Chloride corrosion facilities qualification

The parameters for this isothermal demonstration experiment were defined by DOE SETO and the Chloride Collective. They included a Ni container, Haynes 230 specimen (from the same heat) with 120 grit surface finish, industrial-sourced salt provided by ICL to each participant and an exposure of 800°C for 100 h. Originally, salt purification was

determined by each participant but the salt was to contain no additives. The task was later redefined to include a ~1.7%Mg addition. The task criteria are shown in Table 1.

Table 1. Project Evaluation Criteria for Task 1.0

Task	Description	Criteria	Measured values	Goal Met?	Supporting data
1.0	Complete qualification capsule testing: conduct tests based on set parameters and report results	1. Specimen mass loss 2. < 15µm/yr 3. Repeat ≥3	Figure 11	Yes	Figure 13 Figure 16

Subtask 1.0.1 Preparation of chloride corrosion crucibles.

Initially, samples were exposed to molten chloride salt in Alloy 200 (>99% Ni, ≤0.15% C) capsules measuring 2.54 cm in diameter and 10.2 cm length, with one sample per capsule. Experiments in molybdenum (LCAC, low carbon arc-cast) capsules also were included for comparison to the ORNL standard protocol that the capsule be inert. A schematic of the capsule design is shown in Fig. 5a. Samples were tethered to one endcap of the capsule using Ni wire. Once the capsule was loaded it was welded shut and then welded inside a type 316 stainless steel capsule to prevent oxidation of the Ni capsule and provide secondary containment during the experiment, Fig. 5b. Graphite spacers were used to ensure that no interaction occurred between the inner and outer capsules.

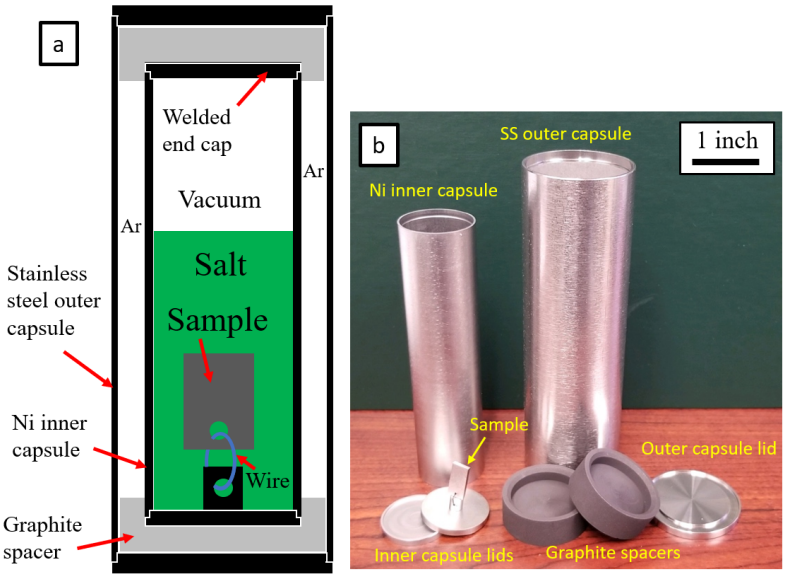

Figure 5. (a) A schematic diagram of a filled capsule (not to scale) and (b) a photograph showing a disassembled capsule with a sample attached to the lid of the inner capsule

In a second type of experiment, a 250 ml Ni crucible and lid were purchased per instructions from the Chloride Collective and Savannah River National Laboratory (SRNL). In addition, a stainless steel (SS) "bag" was used to reduce contamination during the experiment. As ORNL does not have a furnace inside a glove box, a SS container was fabricated to hold the bagged crucible during the 100 h at 800°C exposure, Figures 6a and 6b. A piece of Ta sheet was added to getter residual O.

Subtask 1.0.2 Accept, characterize, and prepare chloride corrosion salts.

The standard ORNL process for preparing "laboratory" eutectic KCl-$MgCl_2$ salt consists of using ACS-grade potassium chloride (KCl) and 98% pure anhydrous magnesium chloride ($MgCl_2$) purchased from Fisher Scientific (KCl) or Milipore-Sigma ($MgCl_2$). The water content of the anhydrous $MgCl_2$ is reported as ≤0.5%. For purification, carbochlorination via carbon tetrachloride (CCl_4) is used to remove oxides based on the work of Young and Mamantov [Young 1990, Chen 1993]. The KCl was melted and equilibrated at 850°C followed by sparging the molten salt with carbon tetrachloride (CCl_4) for 3 h, argon for 0.5 h, argon with 4% hydrogen in argon for 1 h, and argon again for 0.5 h. All gases were Ultra-high Purity (UHP) grade from Airgas and further purified to remove trace moisture with phosphorus pentoxide (P_2O_5) layered with Drierite™. The $MgCl_2$ was purified with the carnallite method, in which the salt is physically mixed with ammonium chloride (NH_4Cl) in a 2:1 $MgCl_2$:NH_4Cl ratio, heated to 450°C for 2 h followed by 1 h at 750°C. The mixture was then sparged with CCl_4 at 850°C for 35-40 h, followed by argon for 0.5 h. The mixture was then sparged with Ar-4%H_2 for 12-15 h, followed by argon for 0.5 h. Lastly, the KCl and $MgCl_2$ were mixed together in the desired 68/32 eutectic composition, heated to 850°C, and sparged with Ar for 0.5 h to effectively mix the salts. In Table 2, this is salt #3.

(a) 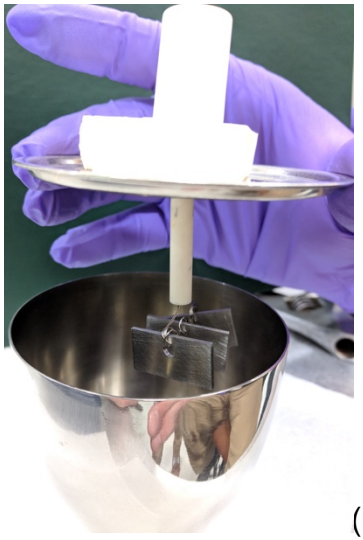 (b) 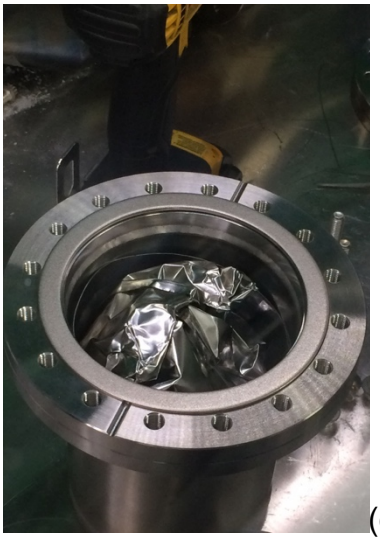 (c) 

Figure 6. Images of (a) Ni crucible, samples and lid, (b) SS vessel with crucible loaded in SS bag before sealing and (c) loaded capsules before heating in box furnace to 800°C.

The “CSP Salt,” described as Na-K-Mg-Cl, was provided by the program and used herein, the starting composition is show in Table 2. It was dried via the carnallite method due to the 4.5% water present, as reported by the supplied elemental analysis, followed by carbochlorination via sparging the molten salt with CCl_4 as described above for the anhydrous $MgCl_2$ with the exception of time. The as-received salt was analyzed by inductively coupled plasma optical emission spectroscopy (ICP-OES) in the as-received condition and after the carnallite process (Salt #2 in Table 2) and after the carnallite and sparging processes (Salt #1 in Table 2). The laboratory eutectic salt is shown for comparison (Salt #3). Unfortunately, ICP-OES was not adequate for determining the composition, particularly the Fe, Mn and Zn contents at ppm levels. Inductively coupled plasma mass spectroscopy (ICP-MS) also was attempted to resolve that issue but was not successful. Also, because of the high Cl content, it was not possible to determine the SO_4^{2-} content.

In order to determine the oxide content of the salt at various processing stages, an acid-base titration process was used. (NREL recently developed a different procedure [Klammer 2020].). A known amount of salt was dissolved in deionized water (18.2 MΩ resistivity). The pH and potential (mV) of the solution was measured with a calibrated pH probe. The solution was titrated with aliquotes of HCl until neutral pH was obtained. As this is a strong acid-weak base titration, complex equilibria exist between the magnesium oxide (MgO), magnesium hydroxide ($Mg(OH)_2$), and $MgCl_2$ in the solution. Attention to the equilibration time was required and each salt tested required an equilibration study to determine an effective equilibration time that did not result in significant pH probe signal drift. For these salts, 5-10 min was adequate. After titration, the amount of HCl consumed was equated to the amount of MgO present within the salt. The use of MgO for the calculations was based upon the thermodynamics of the salt wherein at the temperatures used for carbochlorination, MgO is the thermodynamically preferred species and thus the basicity is assumed to be due to the presence of MgO. While MgO does precipitate out of the salt, there is reported to be a high solubility of MgO within chloride salts [Ostvold 1972, Boghosian 1991, Mediaas 1997, Vindstad 1997, Ito 2004]. It has not been established if the

Table 2. Chemical composition of the industrial-sourced salt determined by mass spectrometry and acid-base titration for the O_2 content for each of the salt variations.

Element	K (%)	Mg (%)	Na (%)	B (ppm)	Fe (ppm)	Mn (ppm)	SO_4 (ppm)	Zn (ppm)	Br (%)	Cl (%)	H_2O (%)	O_2 (µmol/kg)
Specification[1]	21.2	12.8	1.33	2.5	4	2.8	186	1	0.58	58.2	5	
As Received	19.7	12.8	1.55	**	4.67	3.36	^	0.3	0.61	61	5	
Salt #1	20.1	12.9	1.62	**	1.65	1.20	^	0.04	n.d.	65	*	197
Salt #2	18.4	11.9	1.76	**	5.63	2.46	^	0.31	0.39	n/a	*	3934
Salt #3	29.3	9.1	n/a	**	**	**	^	**	n/a	n/a	*	298

[1]as received from industrial salt manufacturer (ICL) documentation
*below detection limits
**below detection limits of ICP-OES & ICP-MS
^Sulfate determination could not be performed on IC due to chloride concentration (resulting in salting out Cl); ICP analysis indicated presence of sulfur but was not quantifiable.

precipitated MgO contributes to the corrosion of structural alloys in the salt. However, it will influence the MgO equilibrium within the melt. If MgO is consumed in the corrosion process, the insoluble MgO will ensure the maximum solubilized MgO is present within the melt, perhaps further enhancing the corrosion. To fully understand the influence of oxide content on corrosion, a method to relate the oxide content is required. In the case of the eutectic KCl-$MgCl_2$ "bottled" salt #3, a molecular formula can be proposed that allows an oxide measurement as parts per million (24 ppm for salt #3). However, for the industrial-sourced salts #1 and #2, a molecular formula is harder to propose because of the complex composition. Therefore, micro-molal (μm), *i.e.* micromoles of MgO per kg of salt, was used as the unit of measure for oxide content for the salts studied to date, Table 2. After only the carnallite process, the oxide content was still 3934 μmol/kg. The additional CCl_4 sparging process dropped the O content to 197 μmol/kg, lower than the eutectic laboratory (bottled) salt. A second batch of salt #1 (#1A) showed an even lower oxide content that could not be quantified.

For the crucible test, the SRNL procedure was followed to slowly heat the salt with N_2 purge to 600°C and drive off water. Per instructions, 5.1 g of Mg was added to 300 g of salt (>1.7 wt.%) and slowly heated to 850°C. After cooling, 170 g of salt was selected for the corrosion experiment.

Subtask 1.0.3. Accept, characterize, and prepare Haynes 230 control samples.

Samples were prepared from ~12 mm thick Haynes™ 230™ plate (pieces of the same plate were delivered to all participants), which was cut into specimens measuring 12.5 x 6.2 x 1.6 mm with a 0.5 mm-diameter hole for the capsule experiments. The chemical composition of the 230 plate is shown in Table 3. Prior to loading in the capsule, all of the coupons were ground to 120-grit finish, except one sample which was ground to a 600 grit finish for comparison. The specimens were weighed using a Mettler Toledo model XP205 balance with an accuracy of ~±0.04 mg.

For the crucible experiment, larger alloy 230 specimens measuring 12.8 x 25.6 x 1.7 mm with a 4 mm diameter hole were used. Figure 6a shows specimens hung together on Ni wire with an alumina holder to electrically isolate the specimens from the crucible.

Subtask 1.0.4. Run & analyze results from H230 chloride corrosion experiments.

Each capsule was filled with 48 g of a mixture of lump and powdered salt, with a volume of 31.9 cm^3 at 800°C, based on a temperature-dependent density of 1.5 g/cm^2 [Williams 2006]. Based on the salt volume, the inner capsule area in contact with the salt was 61 cm^2. Using an average sample surface area of 2.2 cm^2, Table 4 shows various ratios calculated for the capsule (Figure 5) and crucible (Figure 6) experiments:

Table 3. Alloy chemical composition in weight % measured using inductively coupled plasma and combustion analyses.

Alloy	Ni	Cr	Fe	Al	W	Mo	Ti	Mn	Si	S(ppm)	Other
230	58.4	23.1	1.5	0.3	14.0	1.3	0.01	0.49	0.34	<3	0.11C,0.01La
600T	75.5	15.3	9.4	0.2	0.01	0.01	0.15	0.60	0.16	<3	0.05C
600S	77.1	14.4	7.3	0.2	<0.01	<0.01	0.20	0.37	0.30	4	0.08C
244	62.2	8.1	1.0	0.1	5.9	22.4	0.002	0.29	0.04	<3	0.002C
C276	57.7	16.0	5.7	0.2	3.5	15.3	0.005	0.57	0.06	<3	0.002C

Table 4. Various ratios calculated for the capsule and crucible experiments used in these experiments.

	Capsule	Crucible
Salt volume / sample area (cc/cm^2):	14.6	4.9
Salt volume / container surface contacting salt (cc/cm^2):	0.5	1.0
Container surface in contact with the salt / sample area:	28.1	4.7

Both capsules and the crucible were filled in an Ar-filled glovebox with dynamic moisture and oxygen removal. Capsule lids were press fit onto the open end of the capsules. Capsules were then transported under Ar gas in Mason-style jars to an electron-beam (EB) welder where they were removed from the jar, placed in the welding chamber and pumped down to vacuum. The chamber was allowed to pump overnight before welding the lids shut. Subsequently, the Ni and Mo capsules were welded inside a stainless steel outer capsule with graphite spacers to prevent any interaction between the inner and outer capsules during the thermal exposure, Figure 5b.

The capsules were heated in a box furnace at 800°C. Due to an error, the first capsules with CSP salt #1 (carnallite + sparging in Table 2) were removed after 92 h instead of 100 h. At the end of the exposure, the capsules were inverted to allow the salt to drain away from the specimen. After cooling, samples were removed from the capsules and cleaned with 40°C water to remove any residual salt. The mass loss was measured, and the specific mass loss results are presented in Figure 7 with 5 capsules repeating the same conditions. Subsequently, three capsules were run with CSP salt #2 (carnallite only) for 100 h at 800°C. Given the oxide contents measured in Table 2, it was surprising that mass losses were similar in the two salts. To better understand the other parameters being used for this task, several other capsules also were exposed. Mass losses using a Mo capsule and salt #1 or a Ni capsule with eutectic laboratory salt both showed slightly lower mass losses but not the order of magnitude decrease needed to meet the 15 µm/year task goal. Finally, one coupon was exposed with a 600 grit finish using a Ni capsule and salt #1, which also showed a similar mass loss as the 120 grit specimens.

To complete the prescribed characterization, each sample was metallographically mounted in epoxy and polished. Figure 8 shows example sections with the dark areas indicating porosity where Cr was selectively removed from the alloy, particularly along alloy grain boundaries. Figure 9 shows box and whisker plots of ~30 measurements from each specimen with the median value noted. For the five repeat capsules, the median value was 92 µm (larger shaded box). For comparison, alloy 230 samples exposed to eutectic KCl-$MgCl_2$ at 750°C for 300 h in Mo capsules also are shown. The correlation between mass loss and median depth of depletion will be discussed below.

The depth of ≥2% Cr depletion was quantified using electron microprobe analysis (EPMA) with standard-based wavelength dispersive spectroscopy (WDS) or scanning electron microscopy (SEM) with standardless energy dispersive spectroscopy (EDS). Figure 10a shows typical WDS spectra where the Cr content has dropped at the surface to 0-10% after 92 h in salt #1 at 800°C and the depth of ≥2% Cr varied locally depending on the location of grain boundaries. SEM/EDS analysis of each specimen is

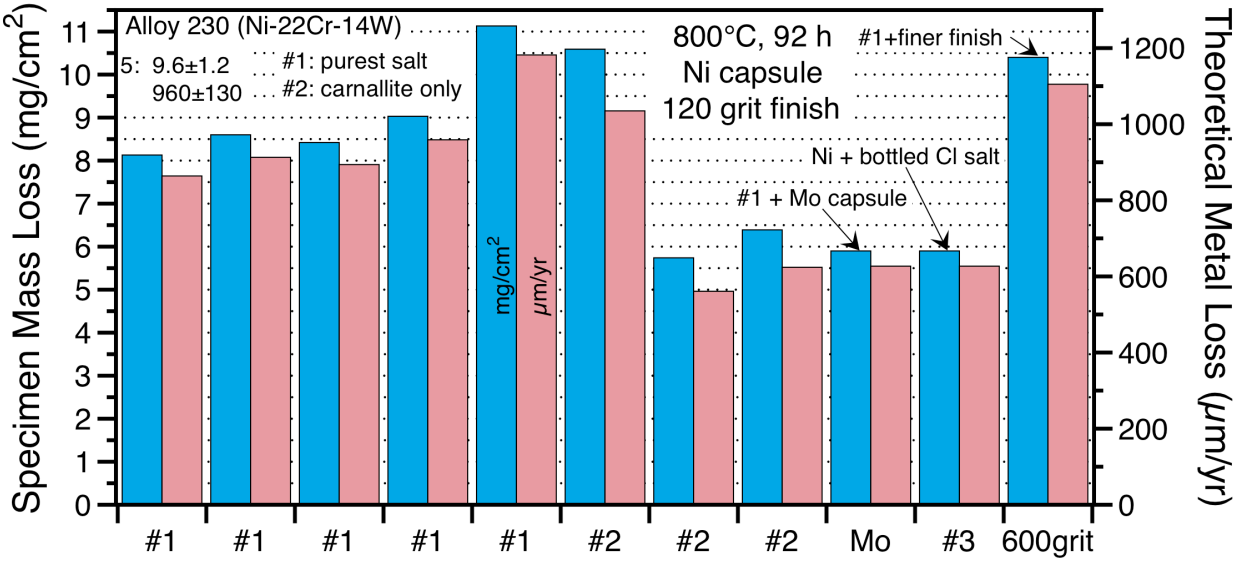

Figure 7. Specimen mass loss and calculated theoretical uniform metal loss converted to μm/yr assuming a linear rate law. Salt #2 was purified using only the carnallite process and those capsules ran for 100 h. Salt #1 used in all of the other capsules used the carnallite plus sparging.

resource intensive. Figure 10b shows the relationship between average void depth and EDS depth where the Cr level had dropped ≥2% and the results are fairly similar. Therefore, the median void depth was used for subsequent experiments and SEM/EDS was reserved for the most critical specimens.

After the unexpected high mass losses in the capsule experiments, the crucible experiment was conducted to repeat the results of the other laboratories in the Chloride Collective using the same alloy 230 specimens exposed for 100 h at 800°C in the Mg-modified industrial-sourced salt prepared by the procedure described above. Figure 11 shows the mass loss data from all three national laboratory members of the Chloride Collective. All of the mass changes (gains and losses) are relatively low and similar.

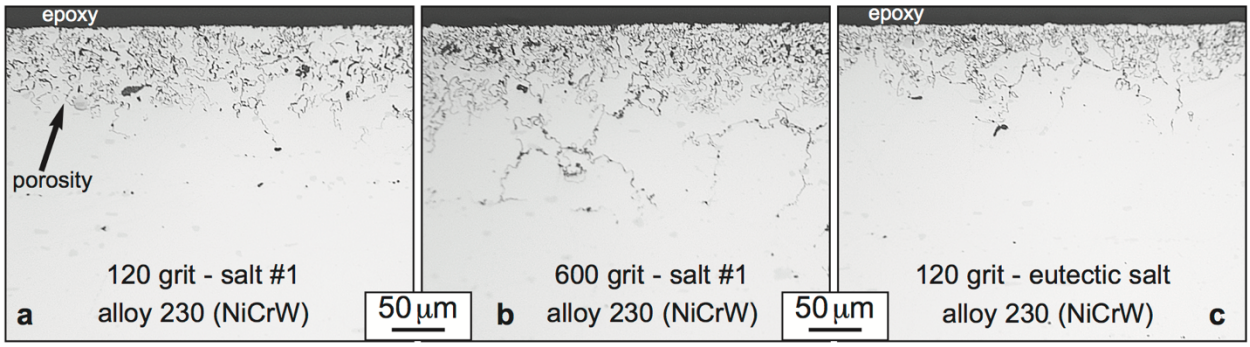

Figure 8. Representative light microscopy of polished sections of alloy 230 after 92 h at 800°C (a) 120 grit, salt #1, (b) 600 grit, salt #1, (c) 120 grit, eutectic salt.

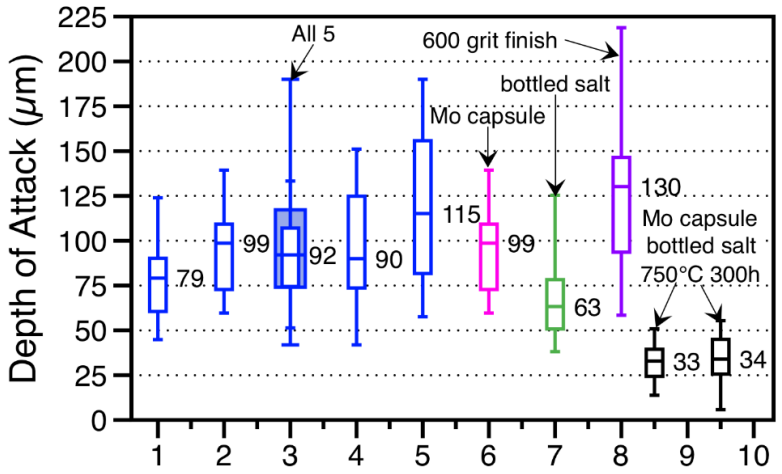

Figure 9. Measured depth of attack for 8 alloy 230 specimens shown in Figure 2 exposed for 92 h at 800°C. For comparison, two 750°C/300 h exposures of a different alloy 230 heat are shown.

Rather than mass losses in Figure 7, the ORNL experiments showed a mass gain after 100 h at 800°C. The standard deviation for the ORNL experiments is similar to that for NREL but the average mass gain was slightly higher. The surface of one specimen was examined by x-ray photoelectron spectroscopy (XPS) prior to mounting. The surface had measurable levels of Zn, Cu and Cl which sputtered away very quickly. An O signal was gone by 20-30 nm of sputtering. However, the underlying surface contained ~18%Mg and <1%Cr to a depth of 300-500nm where the sputtering was stopped. Thus, the mass gain appears to be attributed to Mg uptake and not oxide formation. Also, the lack of Cr and W suggests that Ni diffused outward to react with the Mg in the salt. The mass change variations in Figure 11 may be due to the amount of Mg

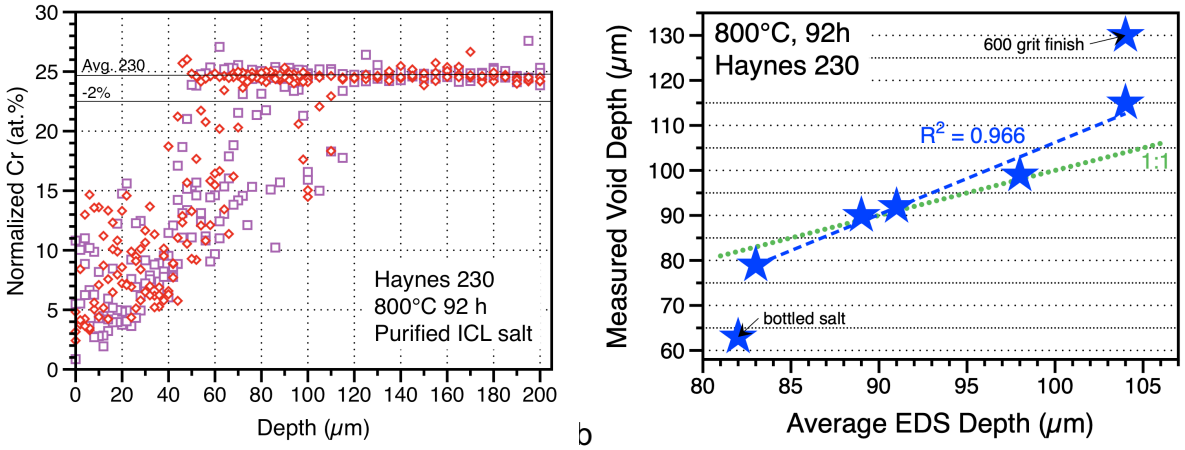

Figure 10. (a) EPMA Cr line profiles from several alloy 230 specimens exposed for 92 h and (b) comparison between depth of 2% depletion by WDS/EDS and average measured void depth from image analysis of light microscopy.

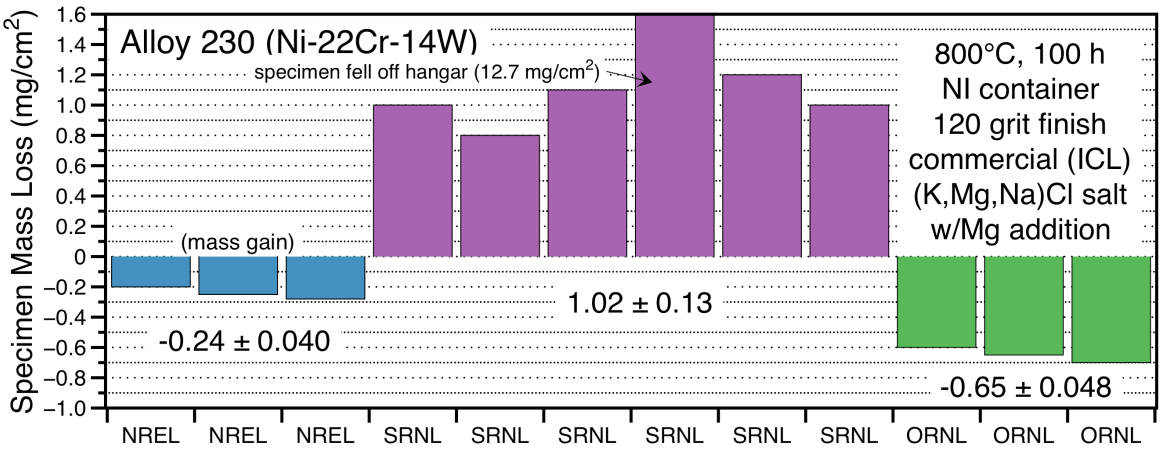

Figure 11. Specimen mass loss for alloy 230 specimens after 100 h at 800°C in industrial-sourced salt with a Mg addition. Additional results shown for SRNL and NREL.

retained in the salt for the experiment or the salt volume/specimen surface area (V/SA) in each experiment. SRNL was able to remove excess Mg from their salt in their process resulting in a small mass loss. However, NREL and ORNL did not remove the Mg and both found mass gains after exposure. Also, since the ORNL procedure did not expose the salt to ambient air, the impurities may have been lower.

Figure 12b shows a cross-section of one of the alloy 230 specimens exposed in the crucible with the high Mg salt for 100 h at 800°C. The surface layer appears to be ~10 µm thick with an intermixed layer beneath it. For comparison, Figure 7a shows the much deeper attack observed in salt #1. Figure 13 shows line profiles from one specimen that are representative of the other measurements. The outermost layer appeared to contain only Ni and ~18%Mg. Very little Cr or W was observed in the outer layer. The inner layer was enriched in Cr, apparently due to the outward diffusion of Ni and also contained some Mg. Figures 14 and 15 show EDX maps of this region on a second specimen. The maps confirm that the outer layer is rich in Ni and Mg and depleted in Cr and W compared to the adjacent substrate. The inner layer is enriched in Cr, W and Mo. The map in 14d also indicates the Fe is enriched in the inner layer. The alloy contains 1.5%Fe, Table 3.

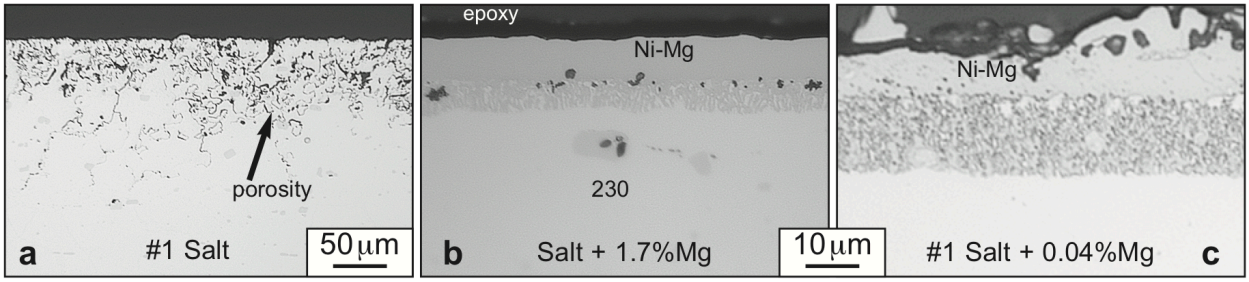

Figure 12. Light microscopy of polished sections of alloy 230 after 100 h at 800°C in (a) salt #1 (V/SA=14.6) in a Ni capsule, (b) salt + 1.7%Mg (V/SA=4.9) in a Ni crucible, (c) salt #1 + 0.04%Mg (V/SA=14.6) in a Mo capsule.

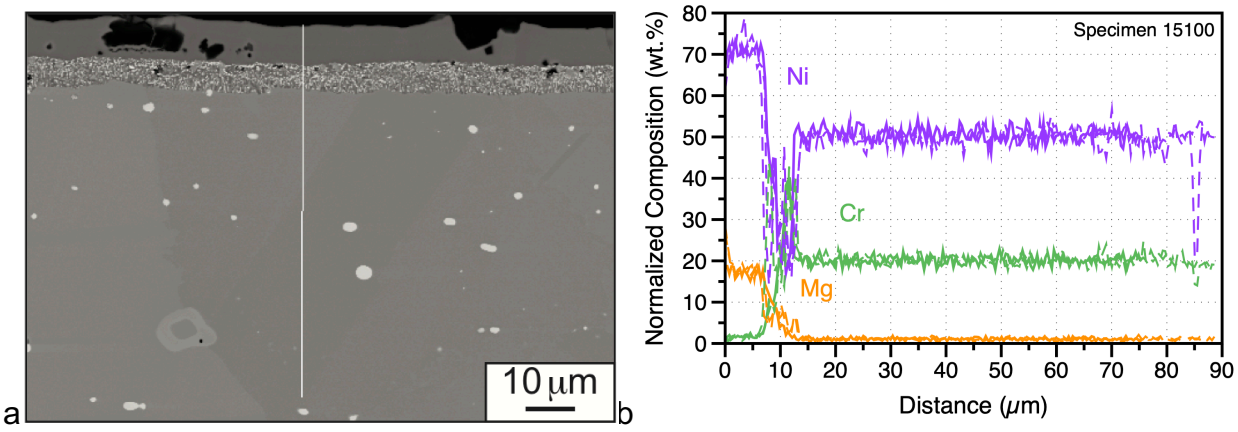

Figure 13. (a) SEM backscattered electron image of a polished section of alloy 230 after 100 h at 800°C in industrial-sourced salt + 1.7%Mg and (b) three SEM/EDX profiles from sample, sold line is from line shown in (a) and dashed lines are from other locations.

The map in Figure 14 was selected because it also showed Mg-rich oxide entrapped in the outer layer and oxide in the inner layer. Since the salt in this experiment was not purified like salt #1, it is likely that Mg-rich oxide was present in the salt and particles could be trapped in the outward growing Ni-Mg layer. However, it is more difficult to explain the O in the inner layer. Figure 15 includes higher magnification EDX maps of the inner region on the same specimen. Surprisingly, the O appears to be associated with Cr in this layer. Additional characterization is needed to resolve the composition and formation of this microstructure. A great deal could be learned from comparing the NREL specimens in Figure 11. It is possible that Cl was present in this layer but was removed

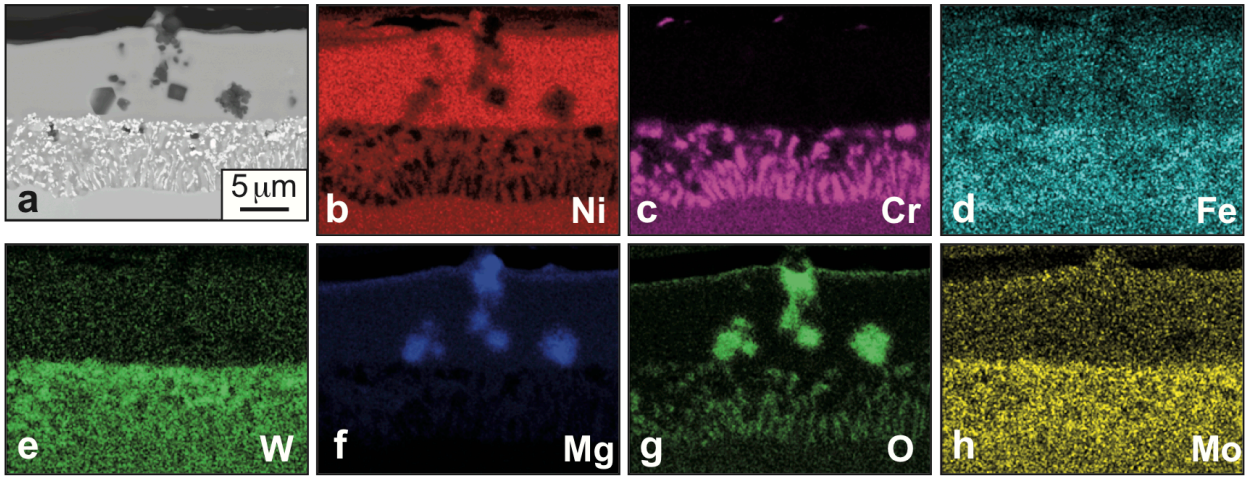

Figure 14. (a) SEM backscattered electron image of a polished section of alloy 230 after 100 h at 800°C in industrial-sourced salt + 1.7%Mg and EDX maps of the area in (a): (b) Ni, (c) Cr, (d) Fe, (e) W, (f) Mg, (g) O and (h) Mo.

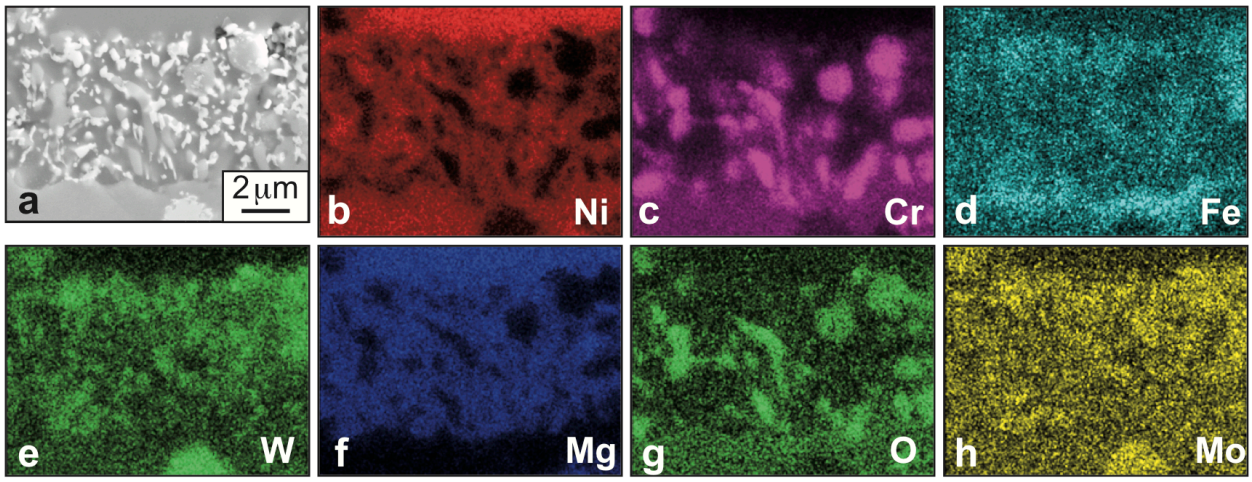

Figure 15. (a) SEM backscattered electron image of polished section of alloy 230 after 100 h at 800°C in industrial-sourced salt + 1.7%Mg and EDX maps of the area in (a): (b) Ni, (c) Cr, (d) Fe, (e) W, (f) Mg, (g) O and (h) Mo.

during cleaning or polishing.

Finally, one specimen was analyzed using glow discharge optical emission spectroscopy (GDOES), Figure 16. Qualitatively, the results were similar to those determined by SEM/EDX and are an average of a ~2 mm diameter sputter crater determined in a ~15 min analysis. Rather than Cr depletion, a Ni-Mg surface layer formed, and Cr and W were enriched in the inner layer. The concentrations of Ni, Cr and W could be calculated using the measured light intensities deep into the sample as a reference [Lance 2018], but since the base alloy contained no Mg, a similar calculation cannot be made for Mg and a Ni/Mg ratio in the layer cannot be calculated using GDOES. Based on XPS and SEM/EDS, the Mg content appears to be ~18 wt.%.

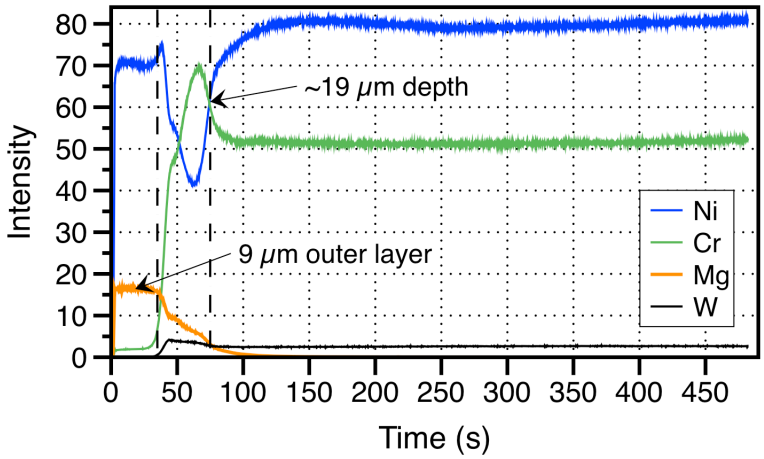

Figure 16. Glow discharge optical emission spectroscopy depth profile of an alloy 230 specimen exposed to Mg-doped salt for 100 h at 800°C.

To further understand these capsule results, a second series of experiments was conducted. Figure 17 summarizes the mass change data from all of the 800°C experiments on alloy 230 with results grouped by capsule and salt type. In one experiment, the specimen was inadvertently welded to the Mo wire and no mass change could be measured. Salt #1B is the batch of salt #1 used in the first TCL experiment. Without Mg added to any of the salts in Figure 17, all of the mass losses were relatively high compared to the small mass gains in Figure 11. The lowest mass loss was found using salt #1B in a Mo capsule. However, the scatter in the three experiments was very high. In light of the high mass losses, a thorough review of all procedures was conducted. There was a concern about the purity of Ar in the glove box during one period and the possibility that the capsules were contaminated when loaded into the EB welder when the lid was in place but not sealed. To avoid this possible source of contamination, the salt #1B capsules were conventionally welded in an Ar glove box. No dramatic impact of these procedure changes was found. However, tighter procedures were developed to prevent inadvertent contamination in future experiments.

In order to characterize the attack observed in these capsule experiments, specimens were cross-sectioned and typical light microscopy images are shown in Figure 18. As noted above, rather than performing SEM/EDX on each specimen, the average void depth was measured, Figure 19. A simple comparison of the data in Figures 17 and 19 is shown in Figure 20 immediately identifies an interesting result that salt #2 behaved differently than salts #1 and #3. One of the confusing things about the mass loss results in Figures 11 and 17 was that the salt with the lowest purity (#2) did not show the largest mass loss. Figure 20 suggests a different behavior for salt #2 in that the average void depth was deeper than expected. Further characterization of two representative specimens suggests that perhaps salt or a reaction product was trapped in the specimen. Whereas the O and Mg maps showed very little after exposure in salt #1 (Figures 21a-21d), stronger O and Na signals could be seen in the 230 sample exposed to salt #2.

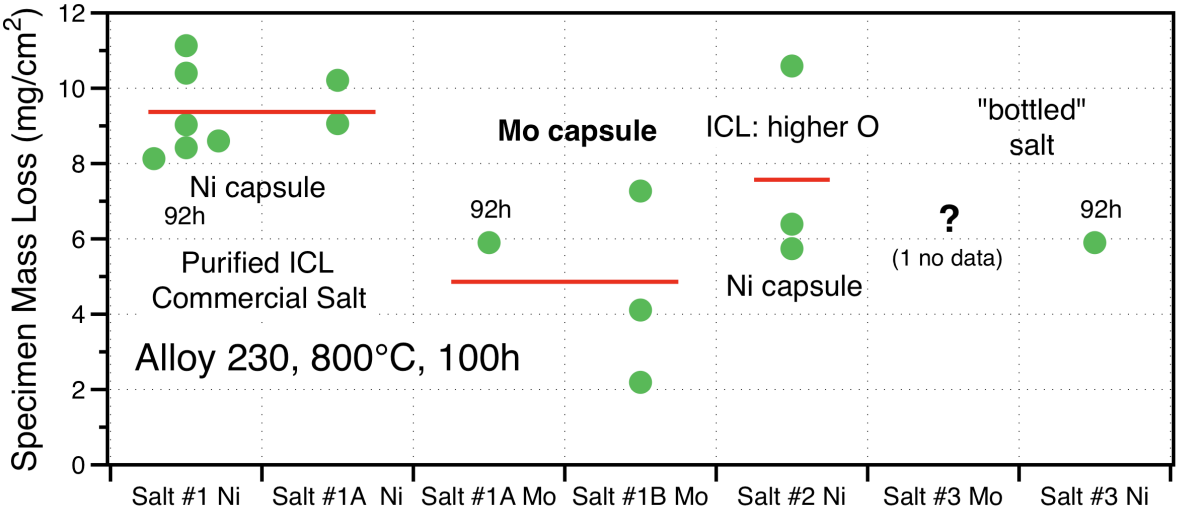

Figure 17. Specimen mass loss results for alloy 230 specimens exposed at 800°C to various salts in Ni or Mo capsules for 92-100 h.

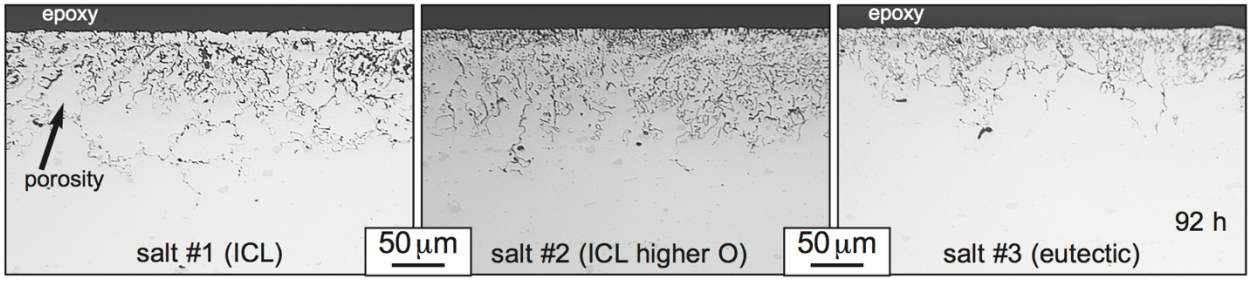

Figure 18. Light microscopy of polished cross-sections of alloy 230 exposed in Ni capsules at 800°C in (a) salt #1 for 100 h, (b) salt #2 for 100 h and (c) salt #3 for 92 h.

This appears to explain the discrepancy in Figure 20. However, comparing void depths in Figures 18 and 19 for the three salts also may not be an accurate assessment based on the Cr maps in Figure 21. The Cr depletion in the maps does not appear to be exactly consistent with void depth in the images. The relationship shown in Figure 10b was only for one salt and Ni capsules and it may not be applicable to other salts.

A second point about salt composition in Figure 19 is that the lowest void depths were observed for the eutectic KCl-$MgCl_2$ salt #3, as indicated in Figure 18. However, only two specimens were exposed to salt #3 and a wide variation was noted between the Ni and Mo capsules. A similar relationship was noted for salt #1 and Figure 22 shows representative images for Ni and Mo capsules in the two salts. In both cases, the void depth appears to be reduced in the Mo capsule. During the Collective meeting, SRNL staff mentioned that Cr can react with the Ni capsule. Based on Equation #1, if the reaction product (Cr in the salt) is being removed from the salt during the exposure then

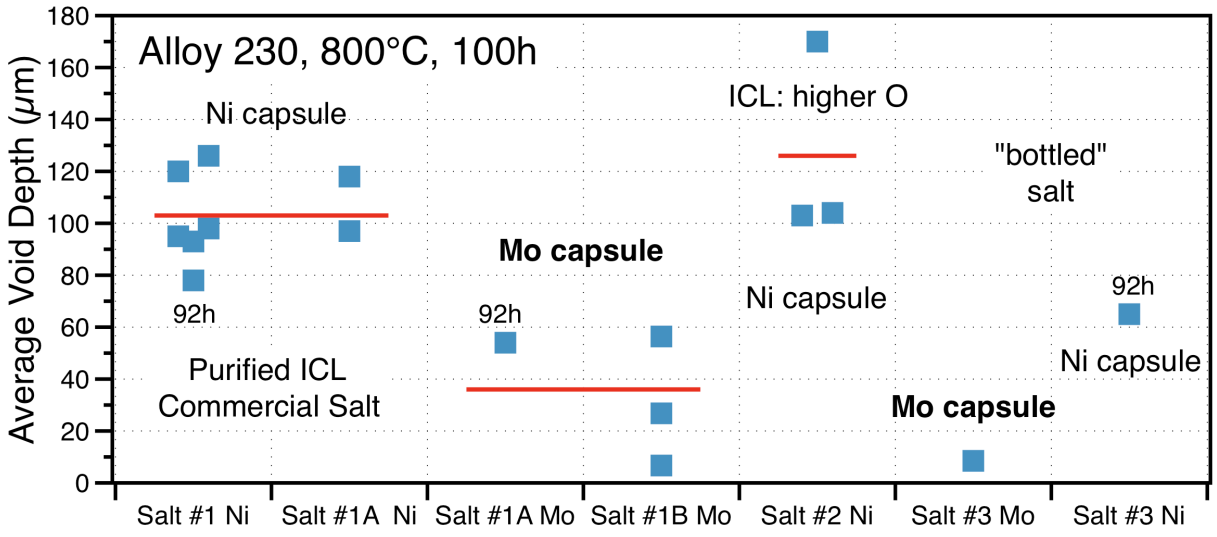

Figure 19. Summary of alloy 230 average void depth measurements after various salt and capsule exposures for 92-100 h at 800°C.

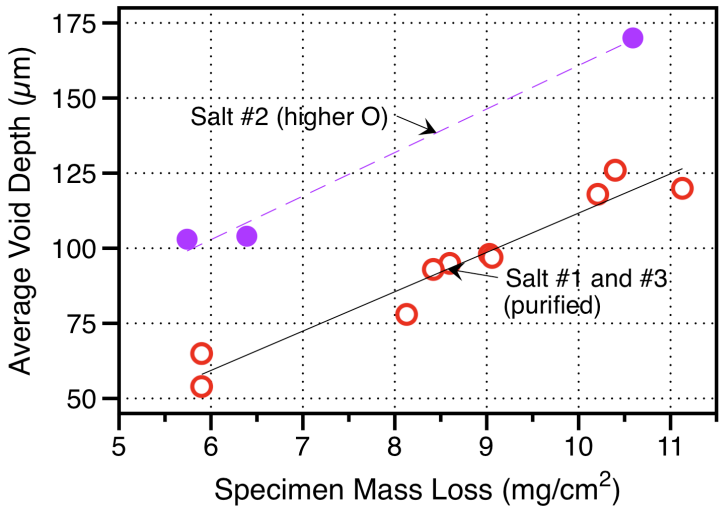

Figure 20. Specimen mass loss plotted versus measured average void depth for alloy 230 specimens exposed for 92-100 h at 800°C in salts #1-#3.

the salt will never reach saturation and the flux of Cr loss will continue at a higher rate. Alternatively, if the container is inert (i.e. Mo) and the Cr reaction product (Cr ions in solution or Cr-Cl-X compounds in the liquid) remains in solution then the liquid will become more saturated with time and the reaction will slow or stop. To test the hypothesis that Cr reacted with the Ni crucible, a 100 h capsule was analyzed, however, the Cr level in the capsule wall was difficult to detect by SEM/EDS. Figure 23b shows the result of a 500 h exposure in salt #1 with a Ni capsule. The sustained attack indicated that the salt did not appear to saturate during a longer exposure as might be expected from Equation #1. The capsule material was characterized after the 500 h

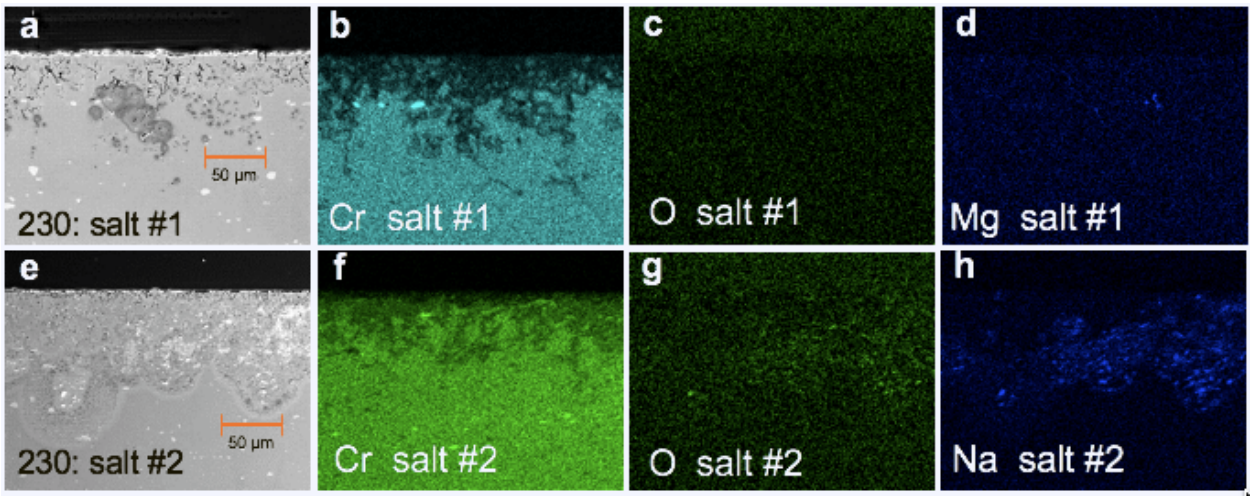

Figure 21. (a,e) SEM images and associated EDS maps of alloy 230 specimen cross-sections after exposure for 100 h at 800°C in Ni capsules to purified industrial-sourced salt (a-d) #1 and (e-h) #2.

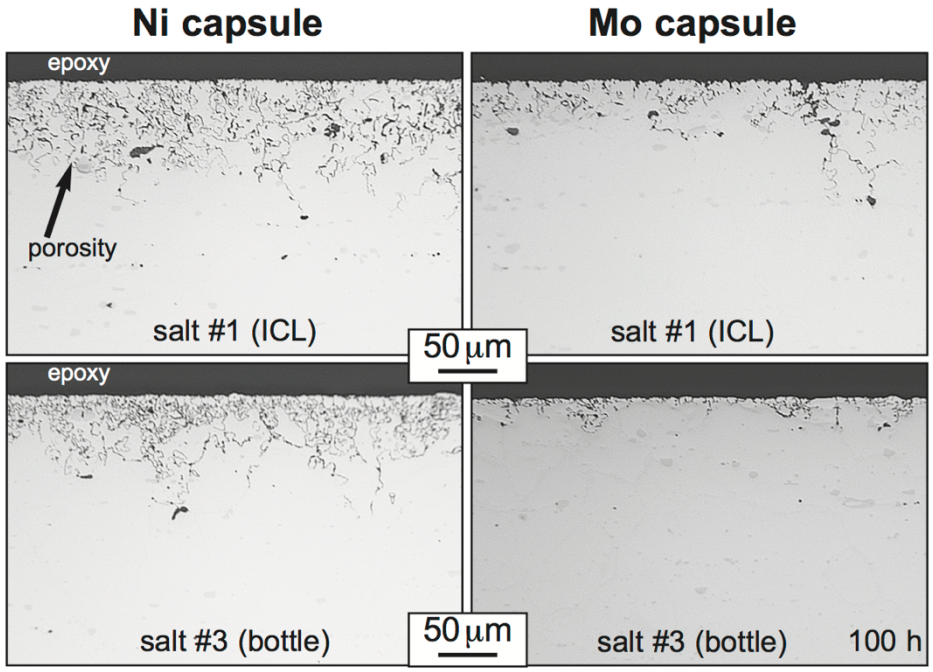

Figure 22. Light microscopy of polished cross-sections of alloy 230 exposed for 92 h at 800°C in (a,b) purified industrial-sourced salt #1 and (c,d) purified laboratory K-Mg-Cl salt #3 and (a,c) Ni capsule and (b,d) Mo capsule.

exposure and the surface adjacent to the salt was enriched in Cr, Figure 23c, indicating that Cr in the salt became incorporated into the Ni capsule wall. The amount of Cr uptake can be estimated based on the EDS data. The areal concentration of the inner surface of the Ni capsule in contact with the salt was estimated at 1.05 mg/cm^2. The 48 g of salt with a density of 1.66 g/cm^3 at 700°C [Williams 2006] had a volume of 28.9 cm^3 corresponding to 55 cm^2 of capsule surface representing a total uptake of 58 mg of Cr by the capsule compared to a measured total specimen mass loss at 800°C of 20 mg after 100 h and 69.8 mg after 500 h. No similar Cr enrichment was noted for a Mo

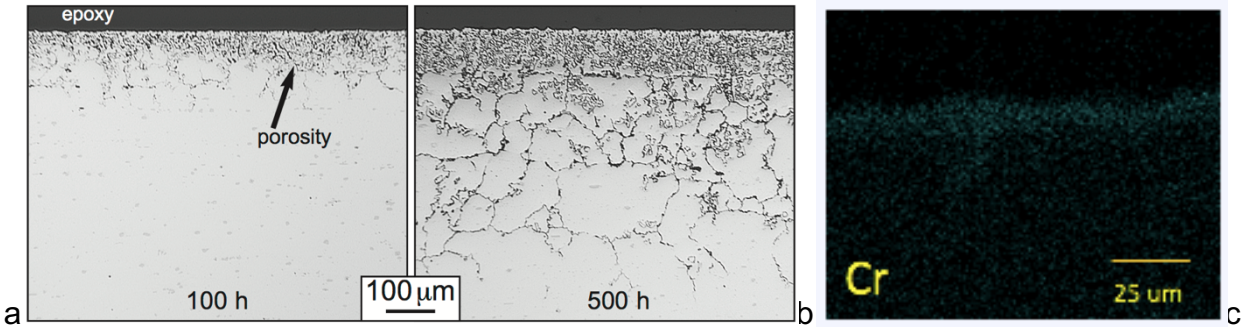

a b c

Figure 23. Light microscopy of alloy 230 specimens exposed to purified industrial-sourced salt #1 in Ni crucibles for (a) 100 h and (b) 500 h. In (c), a Cr EDS map shows Cr enrichment at the surface of the Ni crucible after the 500 h exposure.

crucible after 100 h but no longer experiments have been conducted in Mo crucibles for comparison. Thus, it appears that the Ni capsule is accelerating the reaction by not allowing the salt to saturate with the Cr reaction product. Therefore, future capsule/crucible experiments should be performed in an inert container that does not remove or add reaction products to the salt during the exposure.

Finally, to test the prior ORNL assumption that lowering alloy Cr content is beneficial to halide salt compatibility, Figure 24a shows the effect of alloy Cr content on mass loss in salt #1 after 100 h at 800°C. Similar to the prior results with fluoride salts and Hastelloy N, the low Cr alloy 244 (Table 3) showed a small mass gain rather than a mass loss. These results are contrasted to those in the literature [Sun 2018], where very little effect of alloy Cr content was observed after 100 h at 700°C, Figure 2b. Figure 25a shows no porosity and very little Cr depletion in this specimen in comparison to the alloy 230 specimens in Figure 8. It is not clear why this specimen showed a mass gain. XPS analysis of the surface showed a Ni-Mo rich layer that was enriched in O and C, but the O uptake did not appear sufficient to explain the mass gain.

Reducing the temperature also significantly reduced the mass loss, Figure 24b. After exposure at 700°C, the Cr depleted region was ~10 µm, Figure 25f. By the understanding in Equation 1, the decrease in mass loss with decreasing temperature in Figure 24b may be attributed to a decrease in the Cr solubility with temperature (Figure 1b) and the small Cr depletion at 700°C should not be interpreted as proof of compatibility. Instead, it could reflect a rapid saturation of the salt at this temperature. Actual solubility values for this salt were not determined but Equation 1 suggests an increase in the Cr content of the salt will decrease the dissolution rate.

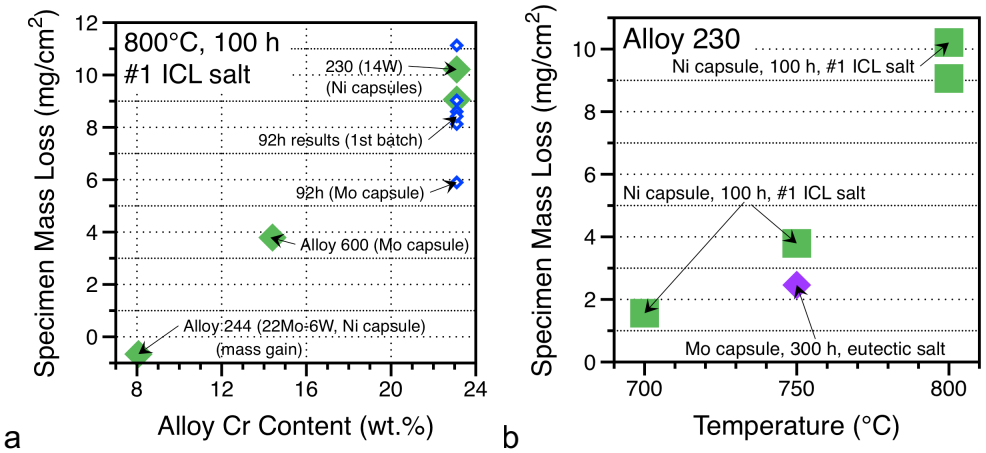

Figure 24. Specimen mass loss after 100 h isothermal salt exposures (a) at 800°C as a function of alloy Cr content in salt #1 and (b) alloy 230 as a function of temperature in salt #1.

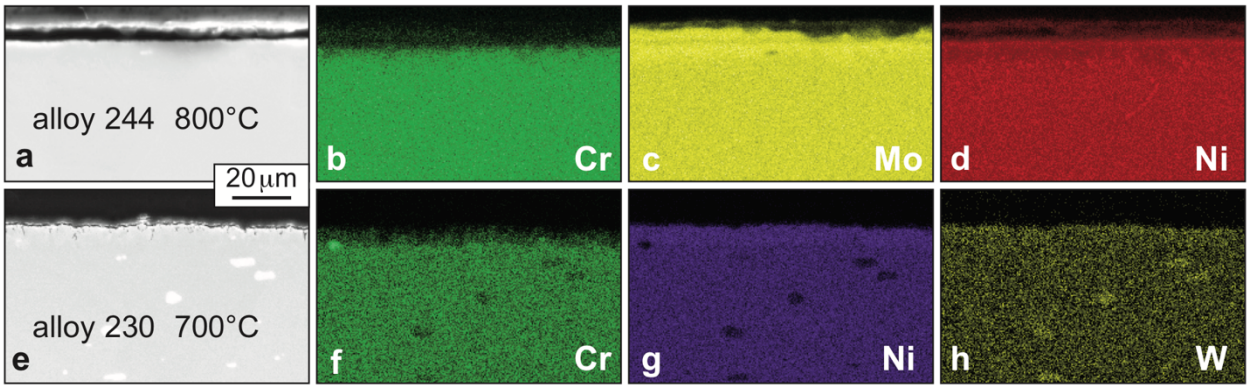

Figure 25 SEM secondary electron images and associated EDS composition maps of polished cross-sections after 100 h exposure in purified industrial-sourced salt #1 in Ni capsules: (a-d) alloy 244 at 800°C and (e-h) alloy 230 at 700°C.

Task 1.1 Capsule testing to support loop experiment

Table 5. Project Evaluation Criteria for Task 1.1

Task	Description	Criteria	Measured values	Goal Met?	Supporting data
1.1	Identify time, temperature, salt and alloys that result in suitably low reaction rates and depth of attack in candidate alloys	1. Depth of attack 2. < 100 µm at 1000 h	Figure 27	Yes	Figure 28

In preparation for the first TCL experiment, alloy 600 was selected as a likely TCL material because of its availability. One reason for choosing alloy 600 is its lower Cr content, Table 3 shows values for tube (600T) and sheet (600S) material used in all of the TCL experiments. Figure 1a shows the Cl potential for a number of different salt and alloying elements. Since Cr is a more stable chloride than Ni or Mo, one would expect selective attack of Cr in the salt. Thus, the results in Figure 24a are not surprising that the mass loss after ~100 h for an alloy 600 specimen was much lower than alloy 230 (with the added complication that alloy 600 was exposed in a Mo capsule). None of the low Cr alloys, such as Hastelloy N or alloy 244 are readily available in tube form. However, Hastelloy N tubing was recently ordered for the ORNL Office of Nuclear Energy molten salt reactor program and could be obtained if future TCL testing is needed, particularly at 800°C.

To reduce risk for the first TCL experiment, three alloy 600 specimens were exposed at 600°, 650° and 700°C in Mo capsules for 1000 h to cover the temperature range and operation time of the first TCL. Figure 26 summarizes the mass loss data after exposure, which were unexpected. The highest mass loss was observed for the specimen exposed at 600°C. However, Figure 27 shows that the depth of attack was relatively minor but unlike the void formation for alloy 230 at 800°C, a pitting type of

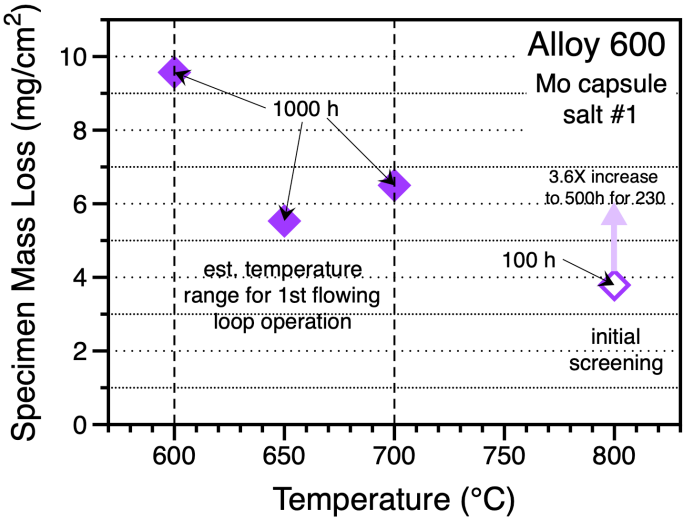

Figure 26. Specimen mass loss for alloy 600 specimens exposed in industrial-sourced salt (#1) in Mo capsules. The 800°C specimen was exposed for only 100 h for comparison to alloy 230.

attack was observed at 600°C different than the observations at 650° and 700°C. Figure 28 shows SEM/EDS analysis of the alloy 600 specimens including the 100 h at 800°C exposure in Figure 24a. Similar to alloy 230 at 800°C, the voids at 800°C appear to be associated with Cr depletion and there appears to be Cr depletion at 650°C. However, very little Cr depletion appears to have occurred for the 600°C specimen. Based on the previously observed effect of salt composition on compatibility in Figure 18 and 19, a question arises about the industrial-sourced salt and particularly its minor impurities of S, Zn, Br, etc.. Figure 29 shows that the purified eutectic “bottle” salt #3 showed considerably less attack for alloy 600 at 600°C and for alloy 230 at 800°C than the purified industrial-sourced salt #1. Nevertheless, the results in Figure 27 provided some confidence that the TCL would operate without issue at a peak temperature of 700°C for 1000 h.

In retrospect, additional capsule experiments for alloy 600 and C276 should have been run at 750°C in anticipation of the second TCL experiment at higher temperatures but the limited 800°C results suggested reasonable compatibility.

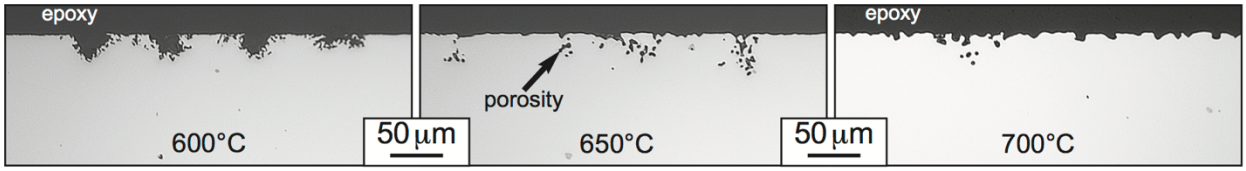

Figure 27. Light microscopy of polished cross-sections of alloy 600 specimens after 1,000 h exposures at 600°-700°C in individual Mo capsules.

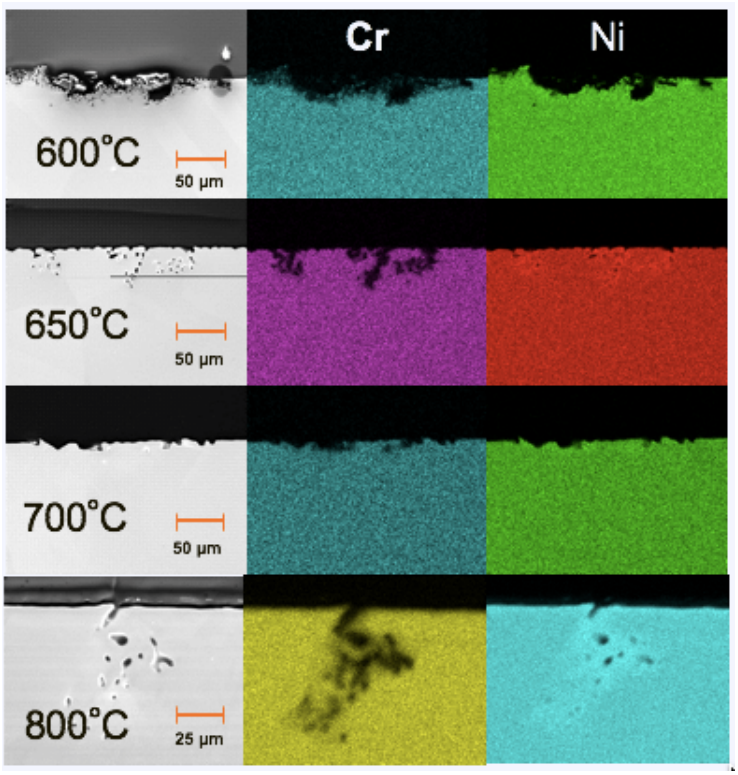

Figure 28. SEM images of alloy 600 specimens after exposures in Mo capsules at 600°-800°C in purified industrial-sourced salt #1 and associated Cr and Ni EDS maps.

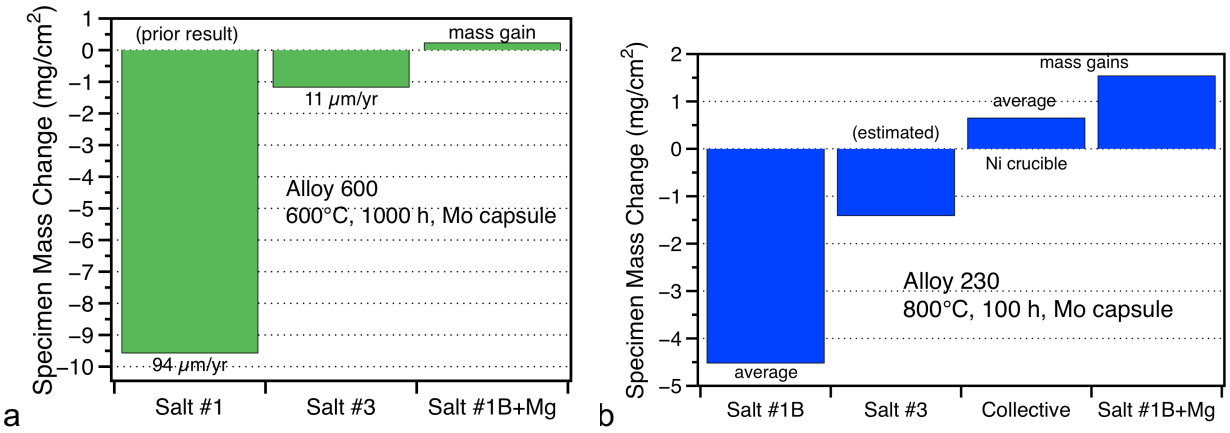

Figure 29. Specimen mass change data from Mo capsule experiments (a) alloy 600 specimens at 600°C for 1000 h and (b) alloy 230 specimens at 800°C for 100 h. Two batches of purified industrial-sourced salt (#1 and #1B) were compared to purified eutectic “bottled” salt (#3). The #1B+0.05%Mg was the salt added to the 1st TCL experiment where the surface area/volume ratio was much different than in a Mo capsule.

Task 1.2 First thermal convection loop test

Table 6. Project Evaluation Criteria for Task 1.2

Task	Description	Criteria	Measured values	Goal Met?	Supporting data
1.2	Complete first loop test of 1000 h	1. Specimen mass loss 2. < 15µm/yr 3. >30 specimens exposed	Figure 32	Yes	Figures 34-40

Figure 30a shows the hood and associated control systems that was built to house the TCL experiments for this project and used for all TCL tasks. To save floor space, the control cabinet with data acquisition and controllers (three furnaces and 10 heat tapes) was built into the hood. Exhaust and power upgrades were completed, and all of the ancillary equipment procured. All TCLs were fabricated from seamless alloy 600 tubing (25 mm outer diameter (OD) and 1.2 mm wall) and sheet (600T and 600S in Table 3) and was ~0.75 m tall by 0.5 m wide. A similar design has been used in other recent liquid metal studies [Pint 2009, Pawel 2012, Pawel 2017]. The first TCL is shown schematically in Figure 30b with the overflow tank above the hot leg. An extension was added to the cold leg to prevent the salt from contacting the stainless steel fitting. Figure 30c shows the loop with the furnaces and insulation in place inside the hood. Prior to loading, the loop was internally cleaned with water plus 20% nitric acid to remove any residual oxide from the tubing inner diameter (ID), followed by water and then acetone prior to evacuation with a turbo pump and pre-heating with heat tape

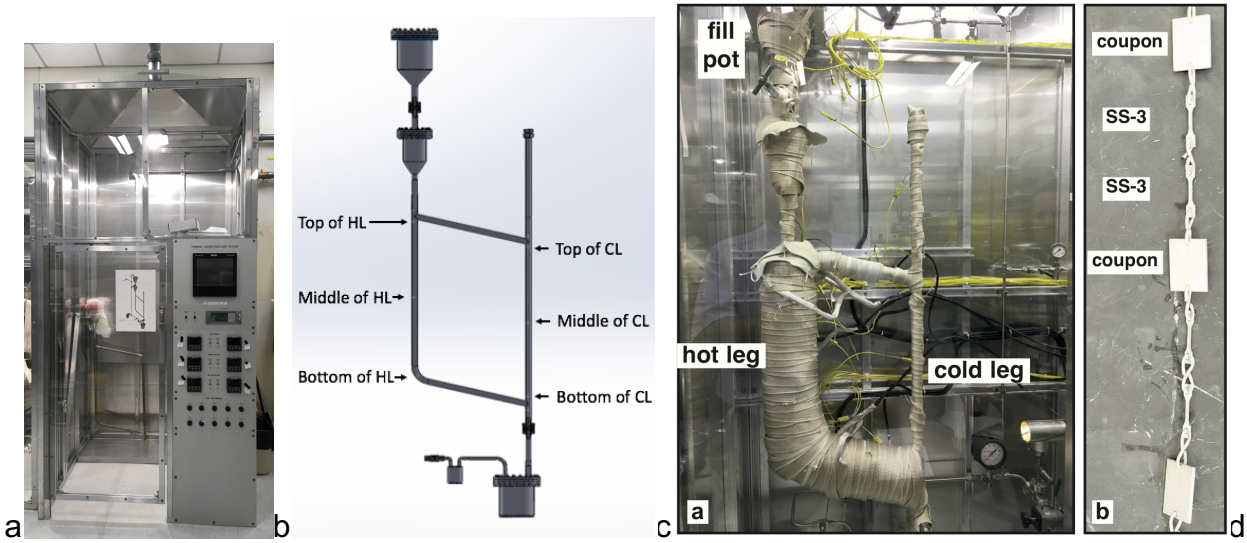

Figure 30. (a) New ORNL molten salt TCL hood, (b) TCL schematic showing location of thermowells (c) TCL during operation with furnaces on hot leg and (d) segment of alloy 600 specimen chain showing coupons and type SS-3 tensile specimens.

to >100°C to drive off any residual water. Evacuation also allows for any leak detection and repair before the salt is loaded in the melt tank.

The alloy 600S specimens in the hot and cold legs consisted of type SS-3 dogbone tensile specimens (25mm long with a 1.5 x 0.76 mm gage) and coupons (1.8 x 19 x 25 mm), Figure 30d. Identical chains of 20 specimens were suspended in the hot and cold legs using alloy 600 wire (1.6 mm diameter) and spanned the distance between the thermowells shown in Figure 30b. At the middle and bottom of each chain an alloy 600 interlocked spacer kept the chain centered in the flow path.

The loop required ~2.3 kg of purified industrial-sourced salt #1 (designated #1B) prepared in 4 batches. Excess salt was used for additional capsule testing, e.g. Figures 17 and 29. Based on the high mass losses observed for alloy 600 specimens in capsules with salt #1, Figure 26, it appeared that the salt had a high Cl potential after purification, Figure 1a. Therefore, 1 g of Mg shavings (0.04wt.% Mg) was added to the salt to lower the Cl potential for the first TCL experiment. Figure 30c shows the loop with resistively heated furnaces on the hot and bottom legs and heat tape in place as well as 24 thermocouples (TCs). The loop was pre-heated to ~500°C prior to filling. The salt was melted using heat tape in a 316L SS pot above the hot leg (Figure 30b) prior to its introduction into the TCL using a SS valve. This composition of industrial-sourced salt melted at ~475°C unlike the eutectic temperature of closer to 425°C. The temperature of the flowing salt in the TCL was monitored primarily by type K thermocouples in 6 thermowells at the top, middle and bottom of the hot and cold legs that were inserted ~3 mm into the flow path, Figure 30b. The loop temperature was controlled at the top of the hot leg to 700±1°C for 1000 h and the bottom of the cold leg was 575-590°C with an average temperature of 580°C, Figure 31. The top leg and cold leg were lightly insulted and not actively cooled or heated. The temperature difference created a density gradient resulting in flow of ~2.4 cm/s determined by monitoring a “hot spot” created by a torch applied for 60 s to the bottom of the cold leg. At the end of the experiment, the salt was dumped

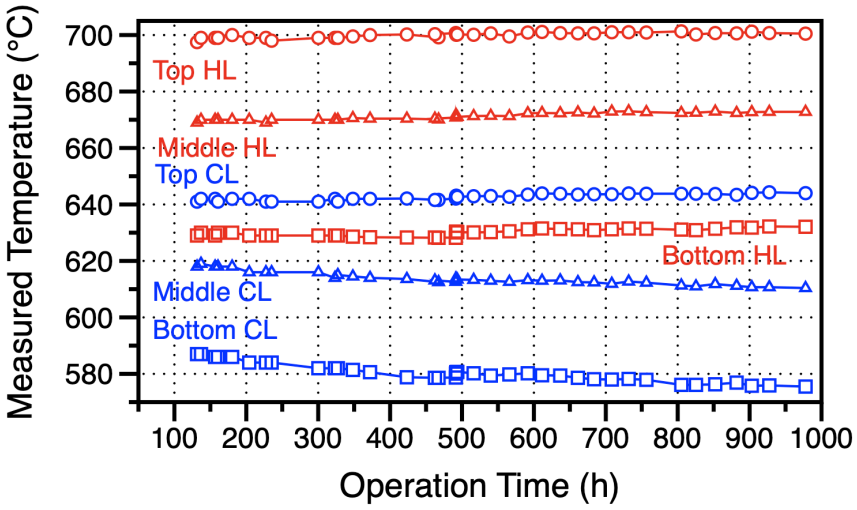

Figure 31. Measured temperatures at six thermocouples around the TCL in the hot leg (HL) and cold leg (CL) during the 1000 h experiment.

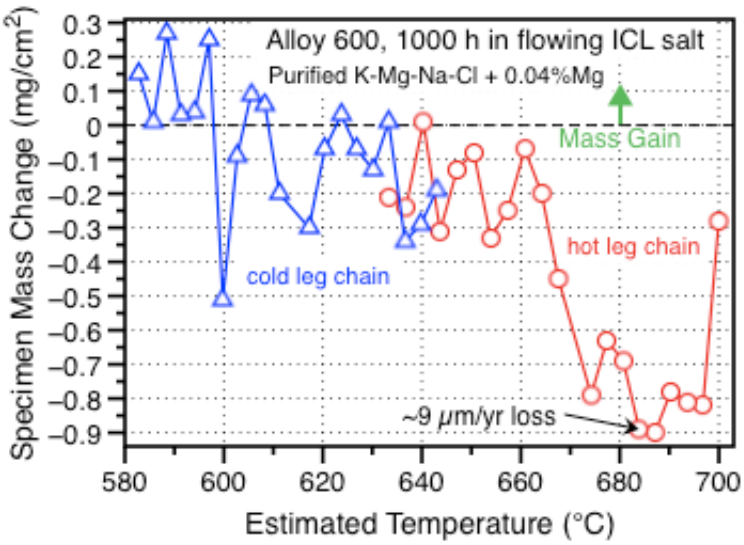

Figure 32. Specimen mass change as a function of estimated temperature for alloy 600 specimens exposed in flowing purified salt.

into a similar SS pot by opening a SS valve below the cold leg, Figure 30b. The specimens were cleaned prior to exposure using acetone and methanol and after exposure by using deionized water at 40°C. Before and after exposure, the specimens were weighed using a Mettler Toledo XP205 balance with an accuracy of ~±0.04 mg.

Figure 32 shows the mass change data obtained from the specimens in the hot leg (HL) and cold leg (CL). The individual specimen temperatures are estimated based on the temperature data from the six thermowells in the TCL. The purified salt with 0.04%Mg appeared to be relatively inert as only small mass losses were observed in the specimens exposed for 1000 h in flowing salt. The data show classic dissolution-precipitation behavior with the largest mass loss at the highest temperatures and mass gain at the coldest temperatures. In stark contrast to the recent literature, Figure 2, this result indicates that Cl salts can be compatible with a structural alloy like alloy 600. To compare these results to the recent literature [Ding 2018, Sun 2018], the mass change was converted to metal loss using the alloy density and linear kinetics were assumed (which may be a worst case scenario). The largest mass loss amounts in the TCL correspond to a ~9 μm/yr corrosion rate, which suggests that this industrial-sourced salt can be compatible with alloy 600 at up to 700°C.

Post-exposure characterization focused on the coupon specimens, which had a larger surface area. As shown in Figure 30d, the coupons were interspersed between the tensile specimens with 6 in each specimen chain. The specimens can be identified based on their estimated exposure temperature as in Figure 32. Figure 33 shows SEM secondary electron images of four specimens from different locations in the loop. The highest temperature specimen that experienced a mass loss at ~690°C showed indication of material removal, Figure 33a. The lowest temperature specimen appeared to show material deposited on the surface, Figure 33d. The other two specimens showed less change.

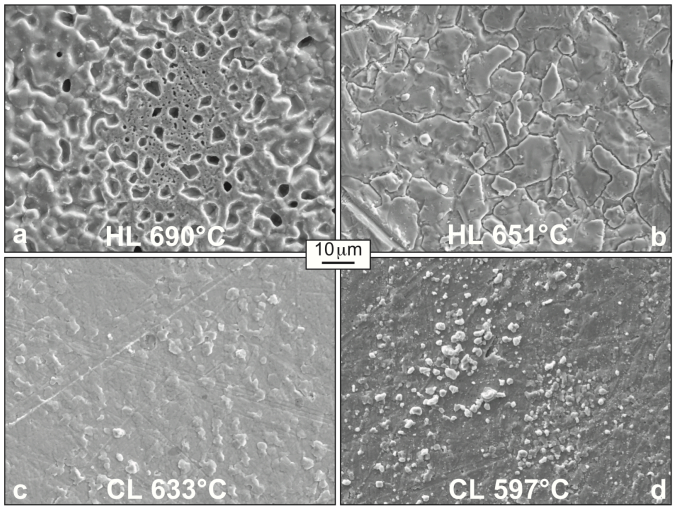

Figure 33. SEM secondary electron plan view images of alloy 600 specimens after 1,000 h exposures in flowing salt + 0.04%Mg identified by their estimated temperature in the hot leg (HL) or cold leg (CL). In (c), observed polishing marks suggested little corrosion.

Figure 34 shows cross sections of the coupons from the HL and CL. Consistent with the mass change data, the highest temperature specimen from the top of the HL (Figure 34a) showed less attack than specimens at slightly lower temperature, Figures 34b and 34c. This may be due to the 700°C specimen being at the very top of the HL perhaps not in a uniform flow region. Consistent with the plan view image in Figure 33a, the cross-section of the specimen exposed at ~690°C showed material removal. However, the pits are ≤ 10 µm in depth. The three specimens from the bottom of the CL all showed small nodules consistent with mass gain, Figures 34j, 34k and 34l. The intermediate temperature specimens showed very little attack.

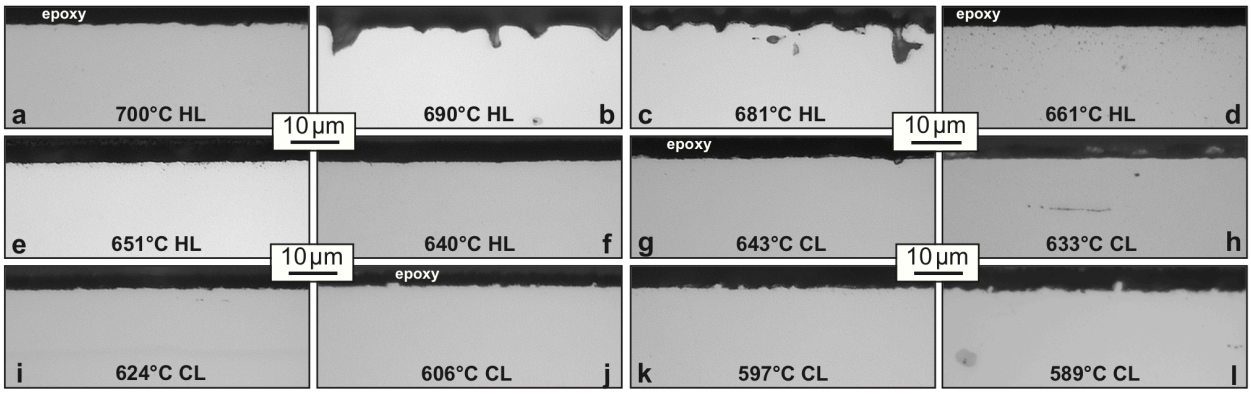

Figure 34. Light microscopy of polished cross-sections of alloy 600 specimens after 1,000 h exposures in flowing purified industrial-sourced salt + 0.04%Mg identified by their estimated temperature in the hot leg (HL) or cold leg (CL). Consistent with the mass change data in Figure 32, (b,c) show material removal at the surface, while (j,k,l) show nodules at the surface.

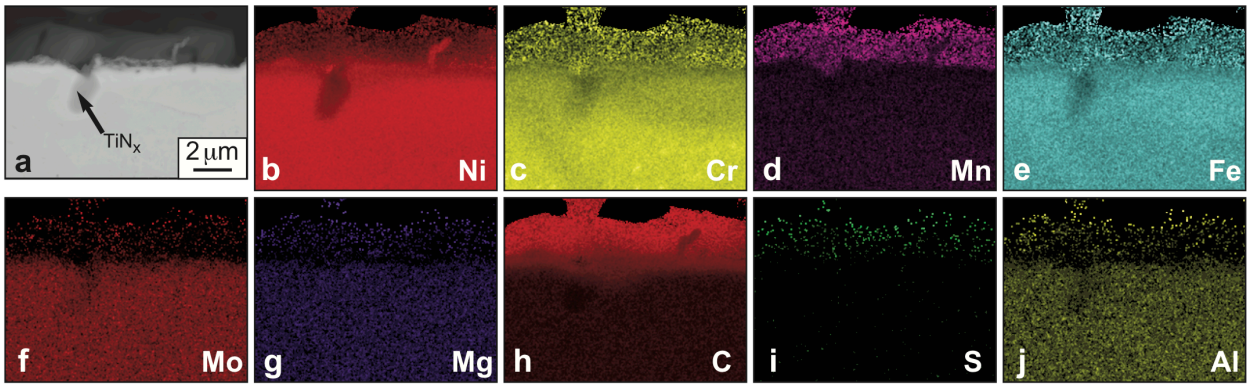

Figure 35. (a) SEM backscattered electron image of polished section of alloy 600 after 1000 h in the hot leg at ~700°C in flowing purified industrial-sourced salt + 0.04%Mg and EDX maps of the area in (a): (b) Ni, (c) Cr, (d) Mn, (e) Fe, (f) Mo, (g) Mg, (h) C, (i) S and (j) Al.

Figures 35, 37 and 38 show SEM/EDX analysis of selected specimens. Figure 35a shows a ~2 µm layer on the surface of the specimen exposed at 700°C at the top of the HL. This layer may explain the different mass change behavior of this specimen compared to the ~690°C specimen. The precipitate in the image is representative of similar Ti-rich precipitates seen throughout all of these alloy 600 specimens. It appeared to be rich in N but could also contain O and C. The outer layer is difficult to identify and may not be metallic. It appears to be depleted in Ni and Mo, although the 0.01%Mo content in alloy 600 (Table 3) makes the Mo map questionable. The layer appears to be enriched in C and Mn and have particles rich in S, Fe and Al (S is present in the industrial-sourced salt, Table 2). No Mg enrichment was detected. An EDX line profile indicated that the Cr was depleted to 10% at the surface, Figure 36a. Consistent with the map in Figure 35c, the depletion was only to a depth of ~5 µm. The area of interest is so small in these specimens that SEM/EDX quantification is somewhat unreliable due to the electron beam exciting a volume in the specimen of ~1 µm diameter. The maps provide qualitative

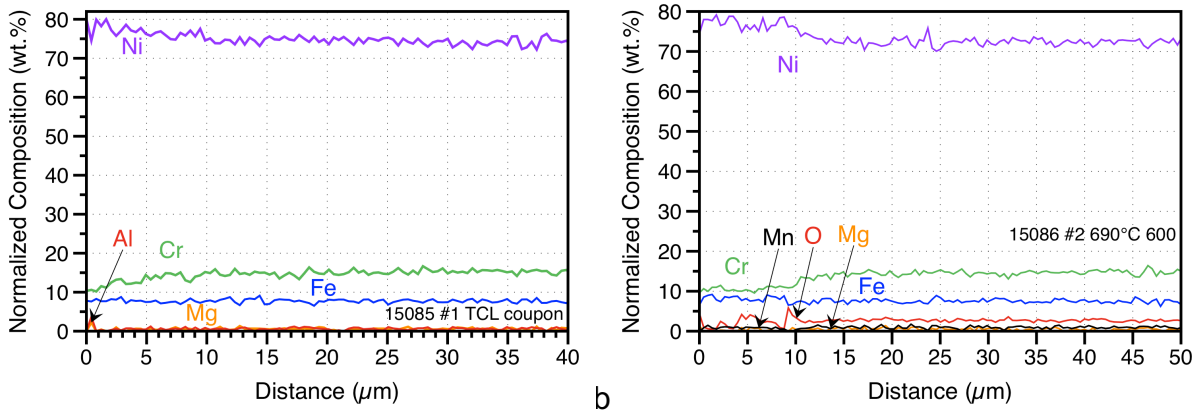

Figure 36. SEM/EDX line profiles from polished sections of alloy 600 after 1000 h in the hot leg in flowing purified industrial-sourced salt + 0.04%Mg at (a) at 700°C and (b) ~690°C.

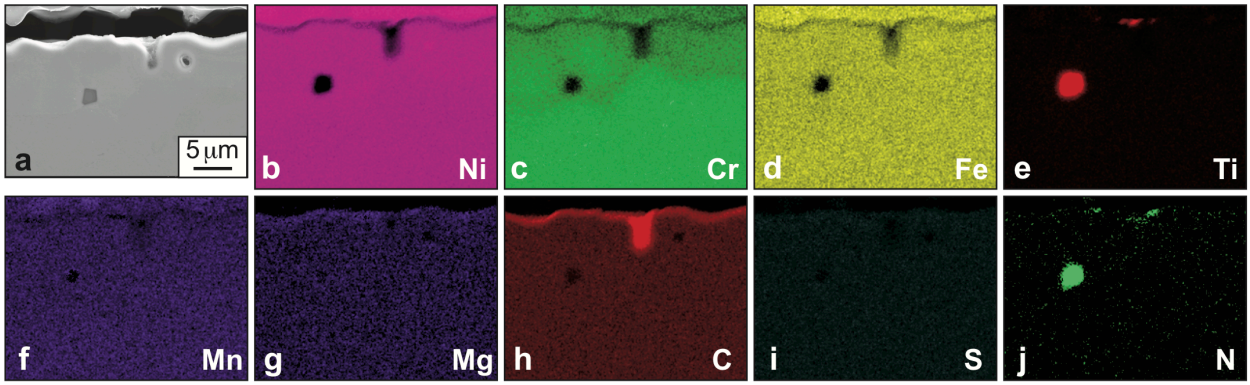

Figure 37. (a) SEM secondary electron image of polished section of alloy 600 after 1000 h in the hot leg at ~690°C in flowing purified industrial-sourced salt + 0.04%Mg and EDX maps of the area in (a): (b) Ni, (c) Cr, (d) Fe, (e) Ti, (f) Mn, (g) Mg, (h) C, (i) S and (j) N.

information but higher magnification or more surface sensitive characterization (e.g. XPS) would be needed to further characterize the surface of this specimen.

Figure 37 shows similar maps from the specimen exposed at ~690°C. In this case the Ti and N maps (Figures 37e and 37j) identify the TiN_x precipitate in Figure 37a. In these maps, the surface also appears to be enriched in C and perhaps a weak Mg signal was observed, Figures 37h and 37g. No S was detected in this specimen, Figure 37i. A line profile indicated that the Cr was depleted to ~10 wt.% at the surface but the depletion was ≤ 10 µm, Figure 36b, consistent with the map in Figure 37c.

Figure 38 shows similar EDX maps for the coupon from the bottom of the CL exposed at ~589°C. A thin outer layer appears to be rich in C and O and depleted in Ni and a deeper region of ~5 µm is rich in Fe and slightly depleted in Cr, Figures 37d and 37c, respectively. A line profile indicated the Fe enrichment was to 13-14%, higher than the 7.3% in the bulk alloy, Table 3. The Cr map shows Cr-rich precipitates that may be oxides in the Fe-rich layer. This specimen gained 0.27 mg/cm^2 and this would

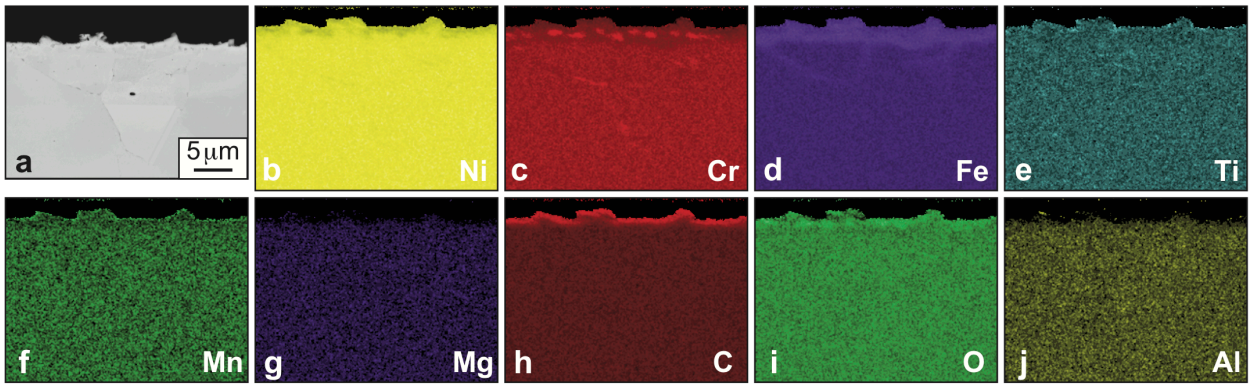

Figure 38. (a) SEM backscattered electron image of polished alloy 600 section after 1000 h in the cold leg at ~589°C in flowing purified industrial-sourced salt + 0.04%Mg and EDX maps of the area in (a): (b) Ni, (c) Cr, (d) Fe, (e) Ti, (f) Mn, (g) Mg, (h) C, (i) O and (j) Al.

correspond to <0.5 μm layer on the surface. Perhaps if Fe is being transported, it is diffusing into the surface of this specimen.

Several specimens also were analyzed by GDOES, which is difficult to quantify without standards. One of the key questions was about Mg alloying, based on the results for alloy 230 in Figure 12b. Figure 39 shows just the Mg intensity from four TCL specimens compared to an unexposed alloy 600 specimen. Almost no Mg was detected in the hot leg specimens except for a slight bump below the surface for the 681°C specimen. Based on the microstructure of this specimen in Figure 34c, this could be residual Mg trapped in the pores. The highest Mg content was observed for the coldest specimen examined, Figure 39. This could be from the material deposited on this specimen. Based on a Mg alloy specimen with an intensity of 222, the 0.55 intensity in Figure 39 would indicate the amount detected at the surface was <<1%.

Half of the 28 tensile specimens exposed were broken at room temperature using a strain rate of 10^{-3} s^{-1}. Figure 40 summarizes the results with data shown as a function of estimated exposure temperature in the HL and CL. The shaded areas show the range of data measured for two as-received alloy 600 specimens. Almost no change in the ultimate tensile strength was observed and a slight reduction in the 0.2% yield stress, Figure 40a. Likewise, almost no change in the uniform or total elongation was observed, Figure 40b.

Thus, the mass change, microstructure characterization and post-exposure tensile properties all indicate that alloy 600 was compatible with purified industrial-sourced salt at 580°-700°C for 1000 h. No Mg-rich layer was formed with a 0.04%Mg addition and very little mass transfer occurred.

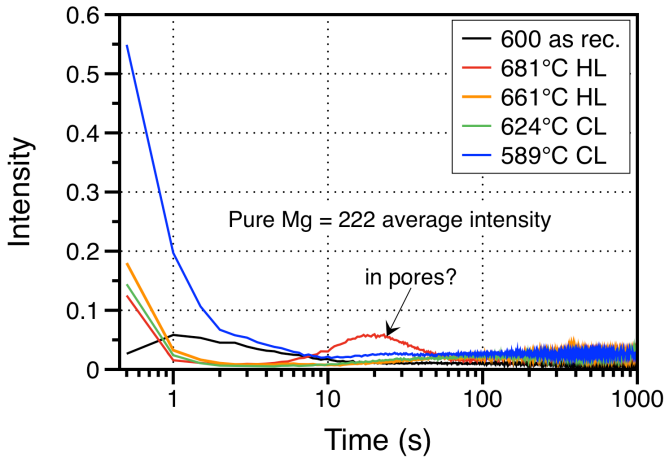

Figure 39. Glow discharge optical emission spectroscopy Mg depth profiles of alloy 600 specimens after 1,000 h exposures in flowing purified industrial-sourced salt + 0.04%Mg identified by their estimated temperature in the hot leg (HL) or cold leg (CL). An unexposed (as received) alloy 600 specimen is shown for reference. The highest Mg signal was observed for the specimen at the lowest temperature.

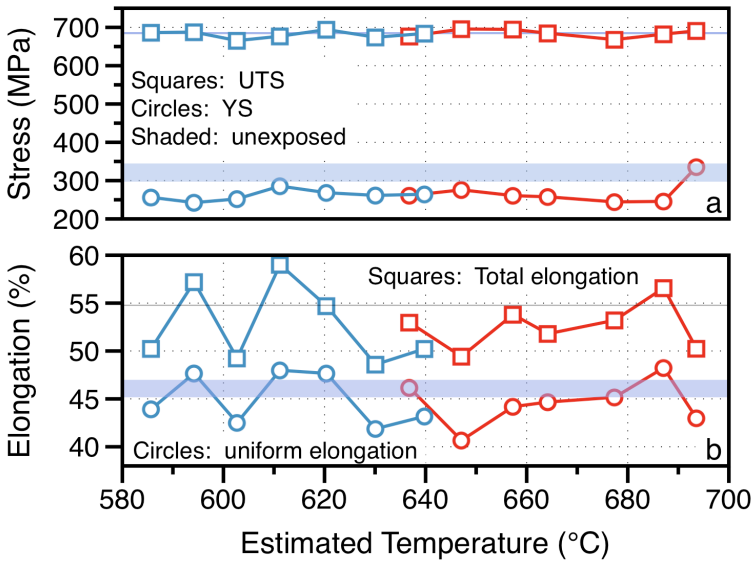

Figure 40. Room temperature tensile properties with a 10^{-3} s^{-1} strain rate for alloy 600 specimens after 1,000 h exposures in flowing purified industrial-sourced salt + 0.04%Mg identified by their estimated temperature in the hot leg (HL) or cold leg (CL). (a) 0.2% yield stress (YS) and ultimate tensile stress (UTS) and (b) uniform and total elongation. The shaded region shows the range of values for unexposed specimens. Minimal degradation in properties was observed.

Task 1.3: Second thermal convection loop test.

Table 7. Project Evaluation Criteria for Task 1.3

Task	Description	Criteria	Measured values	Goal Met?	Supporting data
1.3	Complete second loop test of 1000 h (goal changed from adding mitigation to increased peak temperature)	1. Specimen mass loss 2. < 15µm/yr 3. >30 specimens exposed	Figure 42	No. Only ~110 h operation	Figure 43

This task was originally planned to deploy a getter can from SRNL and a sensor developed by ANL. In late September 2018, SRNL notified ORNL that instead of a getter can, corrosion mitigation would be achieved via a retractable Zr rod into the salt. However, based on the low mass change in the first TCL, it was decided at the end of November 2018 to change the second experiment parameters. Since the mass change in the first TCL met the < 15 µm/yr metric, the effect of a getter could not be adequately demonstrated. Instead, the peak temperature was increased to 750°C and alternating specimens of alloys 600 and C276 (Ni-16%Cr-16%Mo-4%W) were exposed in the specimen chains, Table 3. To expedite the second TCL, it was decided to use the same alloy 600 TCL from the first experiment with the ANL sensor added to the overfill tank

above the hot leg (Figure 30b) so that experience could be gained on the sensor operation.

The sensor was received at ORNL in December 2018. Approximately 2.5 kg of salt #1 was purified using the same ORNL two stage process as described before with a 0.04%Mg addition. The loop was assembled for operation in January 2019 using the same procedure as described for Task 1.2. The SS valves were replaced but the same TCL and fill and dump pots were used. In this case, the top of the hot leg was controlled at 749±1°C. After ~110 h of operation, one furnace failed during holiday weekend operation. Because of the added load to keep the TCL at the temperature setpoint, a second furnace failed about 24 h later followed by the third furnace. By the time staff returned to work, the salt had frozen. The temperature profiles during operation are shown in Figure 41 and indicated a ~175°C temperature gradient. After furnace repairs, the TCL was reheated for ~24 h but flow was not restored and the experiment was terminated. After opening the TCL, there was an empty region in the cold leg that formed during solidification. This area likely had poor thermal conductivity and may have prevented the adjacent salt from re-melting. Some of the salt was drained into the dump attack but most had to be dissolved with warm water to retrieve the specimens.

The mass change for the 40 specimens is shown in Figure 42 and compared to the results for the first TCL experiment (dashed lines). The maximum mass losses and gains were similar in both experiments because of the shorter time but higher temperature in the second experiment. Because the mass change was similar in both experiments, a limited amount of attack was expected for the second set of specimens.

A limited amount of characterization was conducted on this set of specimens for several reasons. The experiment ended near the end of Phase 1 (Year 1) of the project and it was decided to not continue studying the two stage purified salt. Also, the salt composition was changed for Year 2, increasing the NaCl content. Thus, Figures 43 and 44 show light microscopy images of coupon specimens from the hot and cold legs for

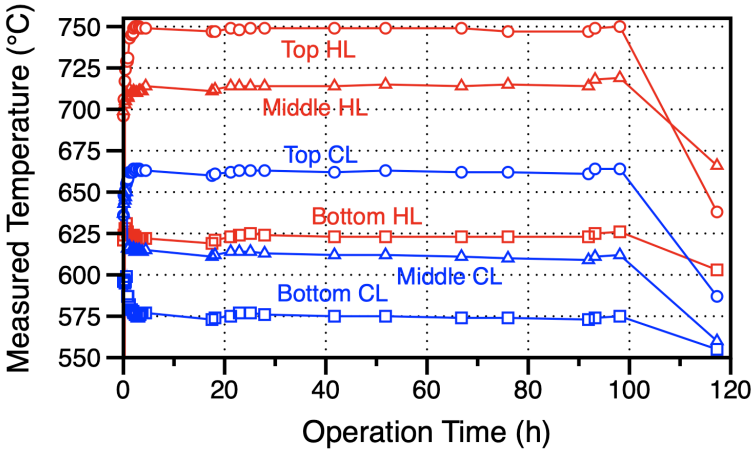

Figure 41. Measured temperatures at six thermocouples around the second TCL in the hot leg (HL) and cold leg (CL) during the experiment, which ended prematurely due to a furnace failure.

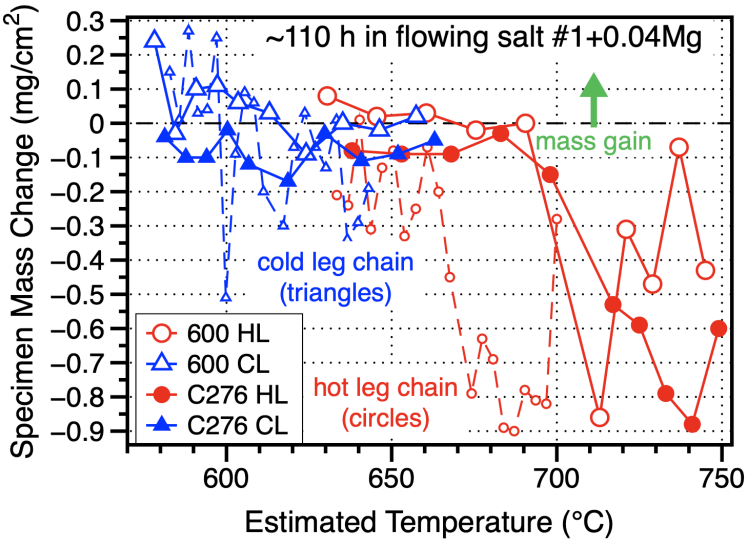

Figure 42. Specimen mass change as a function of estimated temperature for alloy 600 (open symbols) and C276 (closed symbols) specimens exposed in flowing purified salt in the first TCL experiment (dashed lines all alloy 600) and the second TCL experiment (solid lines).

C276 and alloy 600 specimens, respectively. The images are consistent with the mass change data. All of the C276 specimens exposed above 650°C show signs of surface pitting. However, none of the specimens showed a mass gain in the cold leg. Instead all but the 581°C specimen showed a ~5 μm deep surface affected zone, Figure 43. Similarly for the alloy 600 specimens, pitting was observed on the hottest specimens from the cold leg. Four alloy 600 coupons exhibited a mass gain after the exposure. The two coldest specimens in the cold leg clearly showed a layer on the surface, perhaps suggesting material deposition.

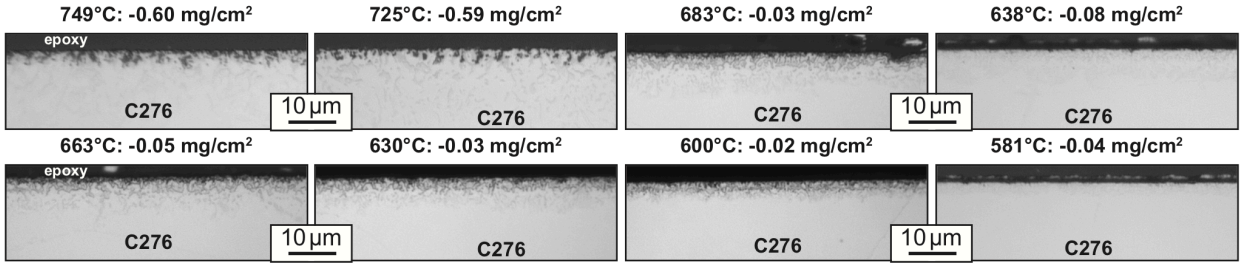

Figure 43. Light microscopy of polished cross-sections of alloy C276 coupons after 110 h exposures in flowing purified industrial-sourced salt + 0.04%Mg identified by their estimated temperature in the hot (top row) and cold leg (bottom row).

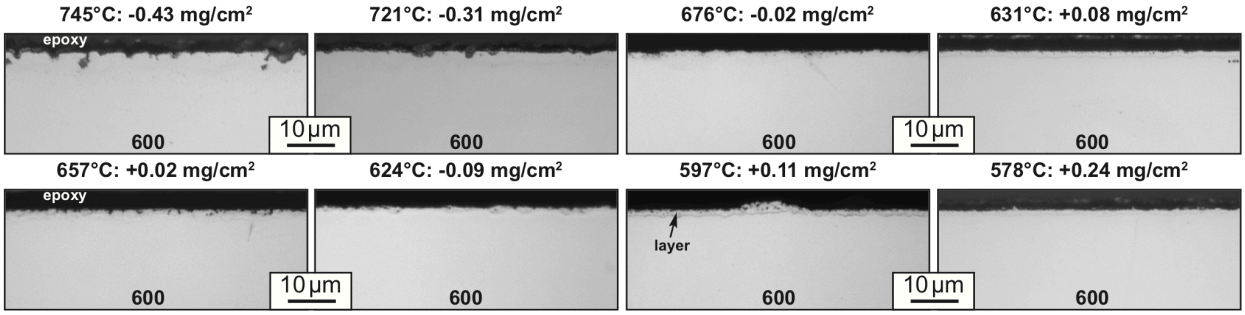

Figure 44. Light microscopy of polished cross-sections of alloy 600 coupons after 110 h exposures in flowing purified industrial-sourced salt + 0.04%Mg identified by their estimated temperature in the hot (top row) and cold leg (bottom row).

Task 2.0: Chloride corrosion facilities qualification

Table 8. Project Evaluation Criteria for Task 2.0

Task	Description	Criteria	Measured values	Goal Met?	Supporting data
2.0	Conduct crucible test and characterize alloy specimens after exposure per instructions on salt preparation, test conditions and characterization	1. Specimen mass loss 2. < 15µm/yr 3. Repeat ≥3	Figure 45	Yes, no mass loss observed	Figure 47

Similar to Task 1.0, Task 2.0 sought to statistically compare Chloride Collective participant results using a modified procedure (see Appendix A). A quartz crucible was used rather than a Ni crucible as well as a new salt composition and preparation procedure. The anhydrous ICL salt was mixed with halite to make a 40:40:20 K:Mg:Na composition. Per the procedure, the salt was heated to 650°C and 0.25% Mg was added. However, most of the added Mg appeared to float to the top or sink to the bottom and was not used in the experiment. Chunks of salt were loaded into the crucible and the three alloy 230 specimens were hung from the Ni lid, similar to what was shown in Figure 6a. The measured composition for alloy 230 is shown in Table 3. The crucible was then placed in a stainless steel bag and the bag was placed in a stainless steel container (Figure 6b) that was bolted shut inside the glove box. The stainless steel container was then removed from the glove box and heated in a box furnace at 800°C for 100 h.

After the exposure was complete, the container was opened, and the specimens were removed and cleaned in water. The mass change data is shown in Figure 45. A mass gain was observed for each of the three specimens. This mass change was higher than the 0.65±0.05 mg/cm^2 observed in Task 1.0. In that case, a Ni-Mg layer formed on the specimens [Pint 2019]. The mass gain was similar to a 800°C/100 h capsule experiment conducted in a Mo capsule (1.54 mg/cm^2), Figure 29b. Figure 46 shows SEM/EDX maps from one of the alloy 230 specimens. In this case, no Mg rich layer formed. Instead there was clear Cr depletion (observed in all of the specimens) and a surprising Fe-enrichment

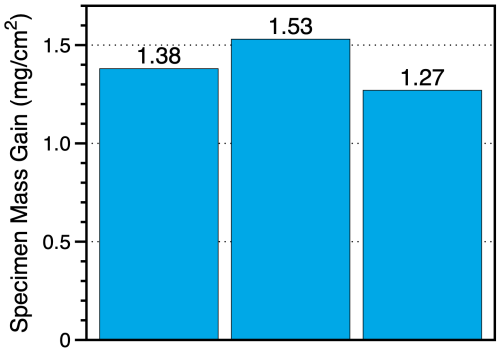

Figure 45. Specimen mass gain for alloy 230 specimens after 100 h at 800°C in industrial-sourced salt with a 0.25% Mg addition.

observed in the outer layer of the reaction product. As shown in Table 3, alloy 230 contains 1.5% Fe so it is unlikely that Fe from the alloy enriched the surface. The only source of Fe in the experiment was the stainless steel bag surrounding the quartz capsule. With the Ni lid, it seems unlikely that the bag contaminated the specimen. Previously, the salt was only found to have 4 ppm Fe, Table 2. ICP analysis of the new salt shows 90ppm Fe (Table 9) after drying the mixture of the as-received salt and halite. Figure 46 also shows that the inner layer contains MgO particles and some Al-rich areas, which is likely Al from the alloy.

Figure 47 shows EDS Cr line profiles from one specimen. The three profiles were taken at roughly ¼ increments along the length of the specimen. The average depletion depth was 16±7 μm in this specimen. The other two specimens had Cr depletions depths of 10±7 and 6±2 μm. Based on the Cr map in Figure 46b, the variability stems from the deeper Cr depletion encountered at alloy grain boundaries. For clarity, only one Fe line profile is shown in Figure 47, which corresponds to the lowest Cr depletion. This shows the Fe enrichment in the outer layer of the reaction product. About 40%Fe and 40%Ni

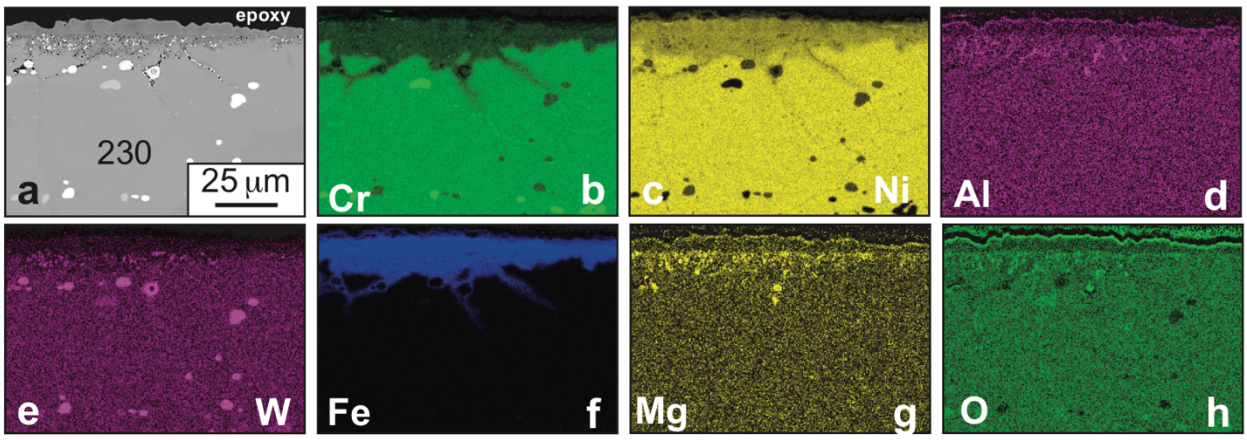

Figure 46. (a) SEM backscattered electron image of a polished section of alloy 230 after exposure to ICL salt for 100 h at 800°C, (b-h) EDX maps of the same region.

Table 9. Chemical composition of the industrial-sourced salt determined by ICP for each of the salt variations and acid-base titration of the O^{2-} content of the dried salt.

	K (%)	Mg (%)	Na (%)	Ca (%)	Br (%)	S (ppm)	Ni (ppm)	Fe (ppm)	Cr (ppm)	Mn (ppm)	W (ppm)	Al (ppm)	O^{2-} (µmol/kg)
As-rec.	20.6	12.2	4.8	0.09	0.14	79	0.3	67	0.2	4	0	2	
Halite	7.9	0.02	31.9	0.26	0.01	6618	0.1	82	0.1	5	0	104	
Dried	18.5	11.2	7.1	0.12	0.14	344	0.4	90	0.04	5	0	4	>20,000
After loop	19.2	11.5	6.8	0.13	0.14	15	**56**	94	**229**	37	44	1	

was detected in the outer layer. However, the outer layer was not uniform on the surface. In some areas, this layer was minimal. It is not clear how such a large amount of Fe formed but NREL and SRNL also observed Fe enrichment after similar exposures.

ORNL was not able to conduct ICP analysis in-house nor the NREL-developed MgOHCl titration without significant investment in standards and equipment. Therefore, specimens were sent to NREL and an outside laboratory generated the results in Table 9. The ORNL acid-base titration was used to determine that a very large O content remained in the salt after drying, very different from the purified salt in Phase 1, Table 2.

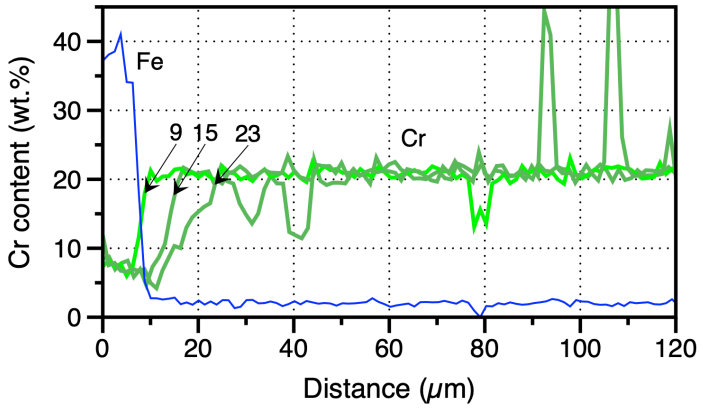

Figure 47. Three EDS line profiles from one of the 230 specimens exposed to ICL salt for 100 h at 800°C. The Cr profiles came from three different parts of the specimen. For clarity, only one Fe profile is shown. The Cr peaks are from the W-rich carbides.

Task 2.1: Capsule testing to support loop experiment

Table 10. Project Evaluation Criteria for Task 2.1

Task	Description	Criteria	Measured values	Goal Met?	Supporting data
2.1	10 capsule experiments: Investigate 3 different Mg additions in 500-1000 h exposures at 600°-800°C in alloy 600 capsules; select Mg level for Task 2.2, process 5kg and determine chemistry	1. Depth of attack 2. < 100 µm at 1000 h	Figure 53	Yes	Figure 52 Table 9

This task had two objectives. First, to help identify an optimal Mg content in the starting salt and second, as a safety requirement to demonstrate reasonable salt-structural alloy compatibility prior to the flowing salt test for Task 2.2. Since the salt composition (higher Na content) and preparation process were changed compared to Phase 1, it was necessary to reconfirm compatibility. The capsule test results also created a baseline for comparison with the flowing experiment results.

Task 2.1 was planned to include at least 10 capsule experiments. The first set of experiments explored 3 Mg addition levels with 500 h exposures at 600° and 700°C with alloy 600 specimens (600S in Table 3). Based on Phase 1 results (Figure 29), the use of a Mo capsule can cause excess reaction of Mg in the salt with the specimen because the Mo container is relatively inert to reaction with Mg. Therefore, 25 mm diameter by 100 mm tall alloy 600 capsules were fabricated for this task made from the same tubing material used to construct the loop (600T in Table 3). In order to create additional Mg levels for this task, a new batch of commercially-sourced dried salt was made with no Mg addition and 0.05 or 0.1%Mg was added to those capsules with the Mg-free salt. Salt from Task 2.0 was used for the experiments with 0.25%Mg in the salt.

Typical capsules with the outer stainless steel capsule are shown in Figure 5. In each case, chunks of salt were loaded into the capsules in an Ar-filled glove box. The alloy 600 capsules were then welded inside outer stainless steels capsules and these were then placed in a box furnace for 500 h at 600° or 700°C. At the conclusion of the experiment, the capsules were inverted to allow the salt to drain away. The capsules were then opened and the specimens cleaned ultrasonically in 40°C de-ionized water. The capsule procedure has been described previously in Tasks 1.0/1.1 [Pint 2019].

The mass change results for these first 6 experiments are shown in Figure 48. One specimen showed a mass gain while the others showed mass losses. These values correspond to ~0-20 µm/yr losses. The mass losses were different from the Task 2.0 result where a mass gain was observed for alloy 230 specimens at 800°C, Figure 45.

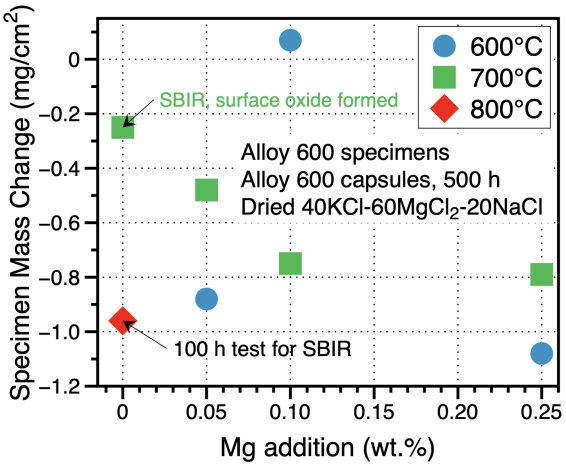

Figure 48. Specimen mass change for alloy 600 specimens after 500 h at 600°-800°C in industrial-sourced dried salt with a Mg addition in an alloy 600 capsule. Additional results are shown for an SBIR project.

Figure 48 also shows results from two capsule experiments funded by a DOE Nuclear Energy SBIR project. Since the goal of the SBIR was to non-destructively characterize tube materials, no Mg addition was added with the goal of maximizing attack. A higher mass loss was observed after 100 h at 800°C in one experiment. However, a much lower mass loss was observed after 500 h at 700°C. In the latter case, the specimen had a green appearance after testing and XPS analysis indicated an oxide layer was present which may account for the lower mass loss with no Mg addition in Figure 48.

Polished cross-sections of the 6 specimens are shown in Figure 49 in addition to a similar alloy 600 specimen exposed for 500 h at 700°C with salt with 0%Mg from the SBIR project. All of the specimens at 600°C looked similar as did the 700°C specimens. Figure 2 quantifies the depth of internal attack in these specimens using box and whisker plots of ~30 measurements from each specimen. Very little effect of Mg content was observed.

The lack of a consistently different behavior in depth of attack among the three Mg levels did not help with the down selection process. However, to scale up to larger salt quantities, it was decided to use the 0.05% Mg addition for the second round of experiments and Task 2.2. A batch of this salt was prepared for the 2nd round of

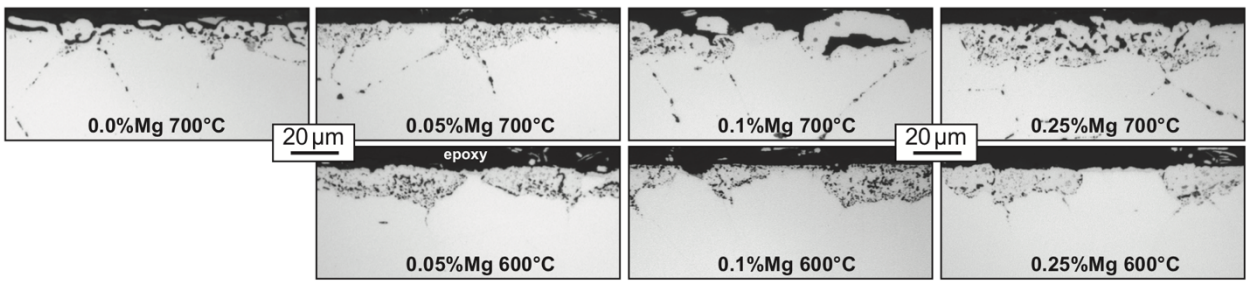

Figure 49. Light microscopy of alloy 600 specimens exposed to dried industrial-sourced molten salt for 500 h at 600° and 700°C with different levels of Mg additions.

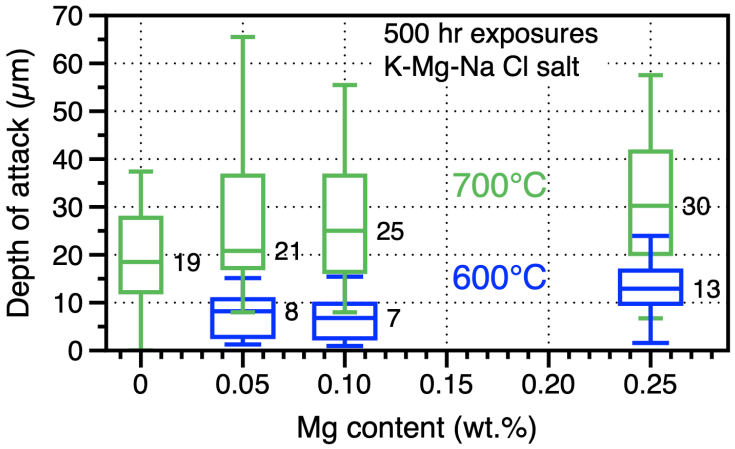

Figure 50. Box and whisker plots of the depth of attack measured for alloy 600 specimens exposed for 500 h at 600° and 700°C in dried industrial-sourced salt as a function of the Mg addition in the salt. The whiskers show the maximum and minimum values measured and the boxes mark the 25% and 75% values with the median value noted.

capsule experiments (Table 9), which were exposed for 1000 h at 600°, 700° and 800°C, again using alloy 600 capsules. No C276 capsules were fabricated since the C276 loop fabricated during Phase 1 was not used for this project. Figure 51 shows the mass change results for alloy 600 and C276 specimens. The composition of this heat of C276 is shown in Table 3. Not unlike the 500 h results, the mass loss was greater at 600°C than at 700°C. The C276 specimen exposed at 800°C exhibited a mass gain similar to the alloy 230 specimens in Task 2.0.

Figure 52 shows metallographic cross-sections of the specimens after the 1000 h exposures. A higher magnification was used for the C276 specimens, which showed

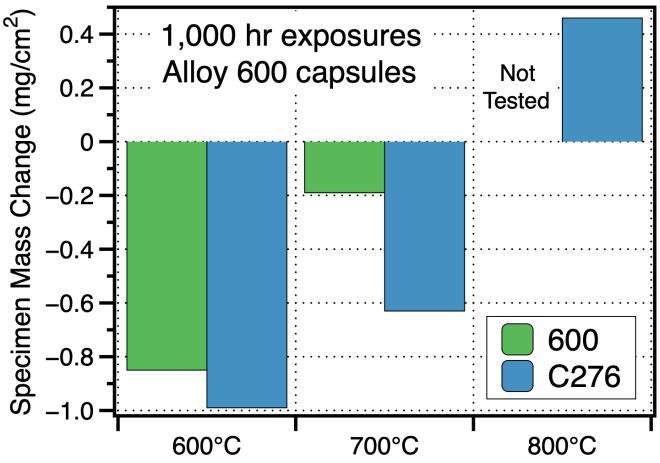

Figure 51. Specimen mass change for alloy 600 and C276 specimens after 100 h at 800°C in dried industrial-sourced salt with 0.05%Mg. Specimens were exposed in individual alloy 600 capsules.

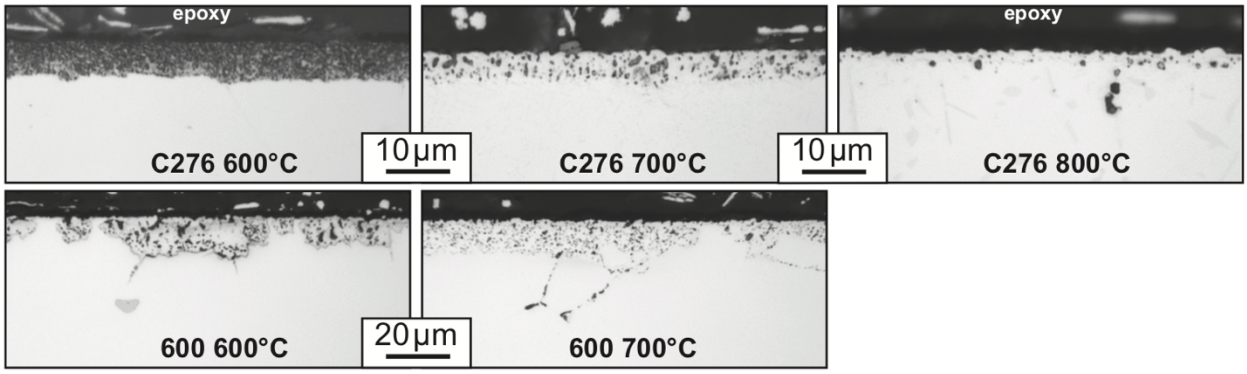

Figure 52. Light microscopy of alloy 600 and C276 specimens exposed to dried industrial-sourced molten salt with 0.05%Mg for 1,000 h at 600°-800°C. A higher magnification was used for the C276 specimens.

higher mass losses at 600° and 700°C than the alloy 600 specimens but showed more uniform attack. Figure 53 quantifies the differences observed with less attack and smaller boxes for the C276 specimens. For the alloy 600 specimens, the attack at 600°C was somewhat consistent with the median depth of attack increasing from 8µm at 500 h in Figure 50 to 10µm after 1000 h. However, at 700°C, the median attack depth dropped from 21µm at 500 h to 11µm at 1000 h. Nevertheless, the attack was relatively low for all of the specimens and provides confidence for Task 2.2 and baseline results for comparison.

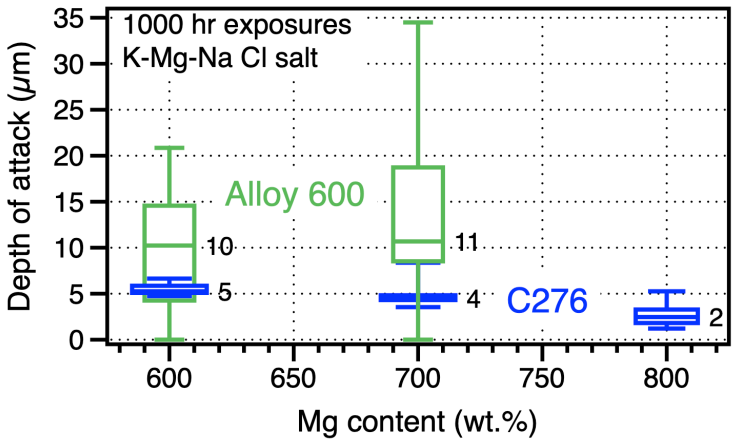

Figure 53. Box and whisker plots of the depth of attack measured for the alloy 600 specimens exposed for 1000 h in dried industrial-sourced salt with 0.05%Mg as a function of exposure temperature. The whiskers show the maximum and minimum values measured and the boxes mark the 25% and 75% values with the median value noted.

Task 2.2: Third thermal convection loop test

Table 11. Project Evaluation Criteria for Task 2.2

Task	Description	Criteria	Measured values	Goal Met?	Supporting data
2.2	Run alloy 600 loop using salt parameters developed in Task 2.1 and include sensor and Mg in melt tank and Mg in cold leg. Peak temperature of 700°C and 40 specimens exposed.	1. Specimen mass change 2. < 15µm/yr 3. >30 specimens exposed 4. Include Mg metal at cold leg bottom	Figure 56	Yes	Figure 54 Figures 58-59

This TCL experiment followed a similar procedure as Task 1.2 [Pint 2019] with a peak temperature of 700°C but used the 40:40:20 dried salt with a 0.05%Mg addition. A similar set of specimens was used as Task 1.3 with chains of 20 alternating alloy 600 and C276 specimens hanging in both the hot and cold legs. The majority of specimens were 25 mm long SS-3 type tensile specimens with a few coupons (25x19x1.8 mm). In addition to the specimens, alloy 600 spacers were added to keep the chain centered in the tube (immediately above the Mg coupon in Figure 54b). The loop design was changed to include a tank at the top of the hot leg to better integrate the ANL sensor into the flowing salt, compare Figures 30 and 54a. Two ports were used to insert 8 tungsten rods for the ANL sensor (the sensor performance will be reported by ANL). A piece of Mg metal was machined to hang at the bottom of the cold leg chain, arrow in Figure 54b. A vacuum throughput was added to the top of the tank so that a Mg rod could be inserted into the tank if the salt potential increased during the 1000 h experiment. (It was not deployed in this experiment.). Because of the larger tank, 5 kg of salt was dried for the experiment.

Similar to the previous procedure, the alloy 600 TCL was cleaned with nitric acid and then rinsed with alcohol and evacuated to ensure a lack of leaks. As before, the temperature of the flowing salt in the TCL was monitored using type K thermocouples in 6 thermowells at the top, middle and bottom of the hot and cold legs that were inserted ~3 mm into the flow path, Figure 30b. The loop temperature was controlled at the top of the hot leg to 700±2°C for 1000 h and the bottom of the cold leg was 550-570°C with an average temperature of 565°C, Figure 55. Several events occurred during the experiment: (1) at ~196 h the temperature dropped inside the pot, (2) at ~230 h, the sensor began to detect an increasing Cr signal in the salt and (3) at ~590 h the top furnace failed and it was repaired the next day (shaded area in Figure 55) such that the experiment was continued for an extra 27 h to make up for the time when the peak temperature was below ~700°C. After removing the insulation, it was discovered that the Ni gasket of the pot above the hot leg leaked and shorted out the heat tape around the pot at ~196 h. The increase in the Cr signal at 230 h may have coincided with the dissolution of the Mg coupon, which was not found after the experiment. It is possible that the two events are related. It is also possible that the leak contributed to the furnace failure. After the experience with

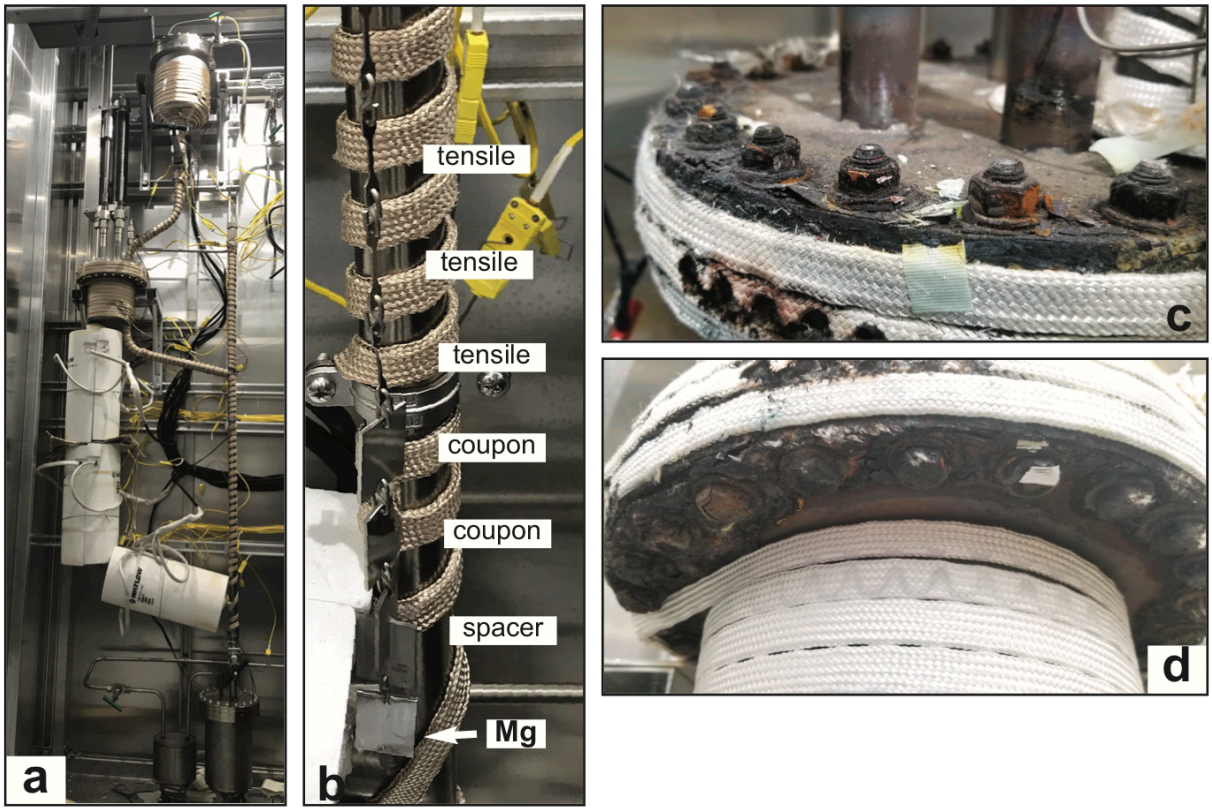

Figure 54. (a) Image of the thermal convection loop (TCL) before operation, without heat tape or insulation including fill tank at top and dump tank at the bottom and intermediate tank at the top of the hot leg. (b) cold leg chain hanging outside loop showing Mg specimen at the bottom of the chain (arrow). (c,d) Flange of top leg pot after operation.

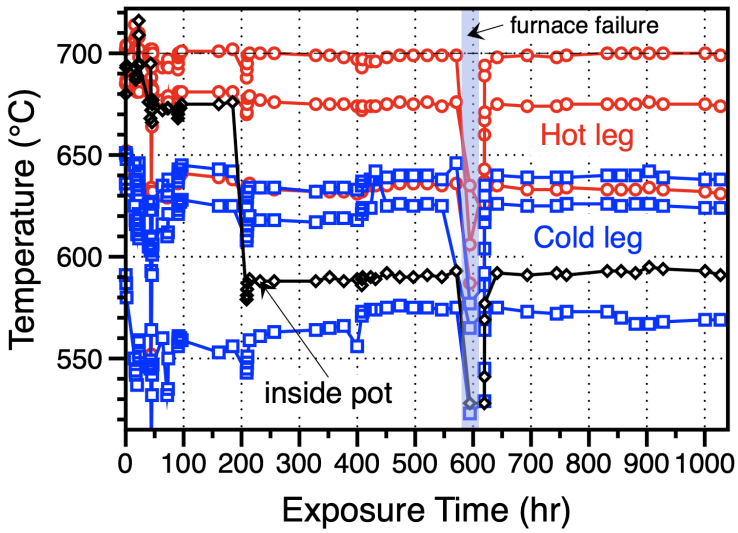

Figure 55. Measured temperatures at six thermocouples around the TCL in the hot leg (HL) and cold leg (CL) during the 1000 h experiment. A furnace failure caused a drop in the peak temperature at ~590°C and required ~27 h to repair and return to temperature.

the second loop furnace failures, all of the furnace controllers were set to prevent the other furnaces from overheating when one failed.

Similar to the procedure reported for tasks 1.2 and 1.3, a similar flow rate was measured for 2.4 cm/s. At the end of the experiment, the salt was dumped and the loop was cleaned using deionized water at 40°C. Figure 56 compares the mass change of the alternating C276 and alloy 600 specimens to the mass change measured in the Task 1.2 loop with purified salt. In general, all of the measured masses were slightly higher than the previous experiment with more specimens experiencing a mass gain in this experiment. Both the alloy 600 and C276 specimens experienced a mass loss at the highest temperatures, >670°C. Unlike the Task 1.2 specimens, the highest temperature specimen did not show obvious porosity on the surface. However, many of the specimens showed indications of surface deposits. For example, Figure 57a shows a plan view SEM image of the alloy 600 specimen exposed at ~639°C. The figure also includes SEM/EDX maps from the same region which indicate that the surface deposit is rich in Mg, O and Cl.

All of the coupons were cross-sectioned for analysis and the alloy 600 and C276 specimens from the HL and CL are shown in Figures 58 and 59, respectively. While the depth of attack was small in all cases, it was surprising to see in the cold leg evidence of both deposits and internal attack. In Figures 34, 43 and 44, the CL specimens tended to have minimal attack and only evidence of deposits. In Figures 58 and 59, only the specimens exposed below ~600°C showed no internal attack. Also, regarding the surface deposits, both metallic and non-metallic deposits were evident on the CL specimens. Figure 60 is a box and whisker plot where an attempt was made to quantify the deposit thickness and depth of internal attack for all of the coupon specimens of C276 and alloy 600. All of the median depths were <16 μm but attack was as deep as 20-28 μm.

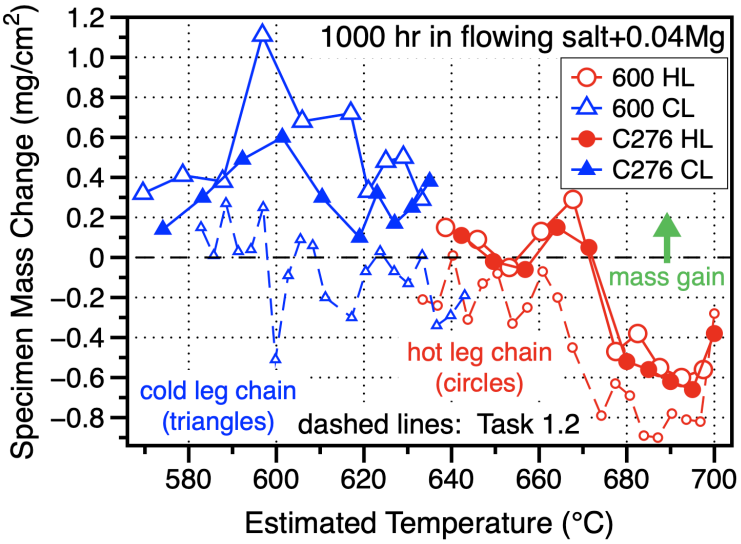

Figure 56. Specimen mass change as a function of estimated temperature for alloy 600 and C276 specimens exposed in flowing purified salt. Solid lines for Task 2.2, dashed lines for Task 1.2.

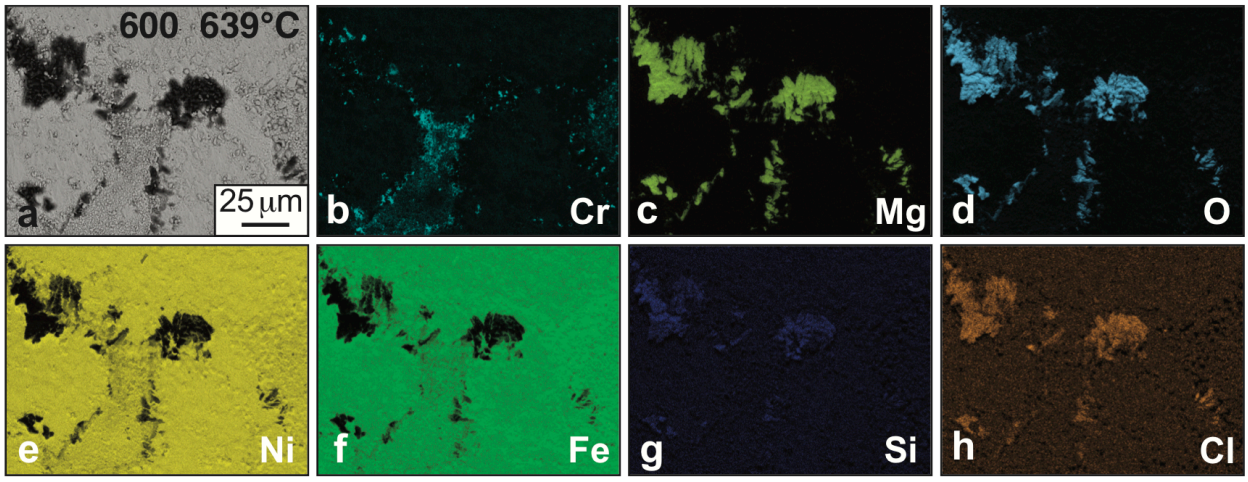

Figure 57. (a) SEM secondary electron plan view image of alloy 600 specimen after 1,000 h exposure in flowing dried industrial-sourced salt + 0.04%Mg at ~639°C. Associated SEM EDX maps of (a): (b) Cr, (c) Mg, (d) O, (e) Ni, (f) Fe, (g) Si and (h) Cl.

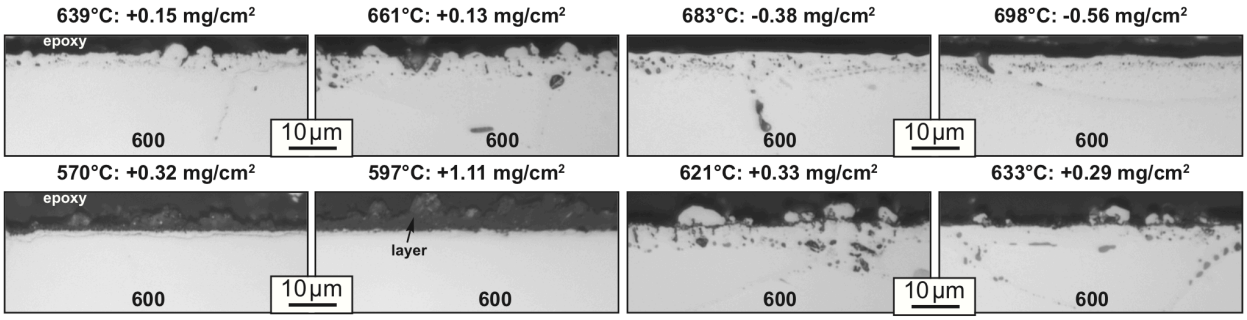

Figure 58. Light microscopy of polished cross-sections of alloy 600 coupons after 1000 h exposures in flowing dried industrial-sourced salt + 0.05%Mg identified by their estimated temperature in the hot (top row) and cold leg (bottom row).

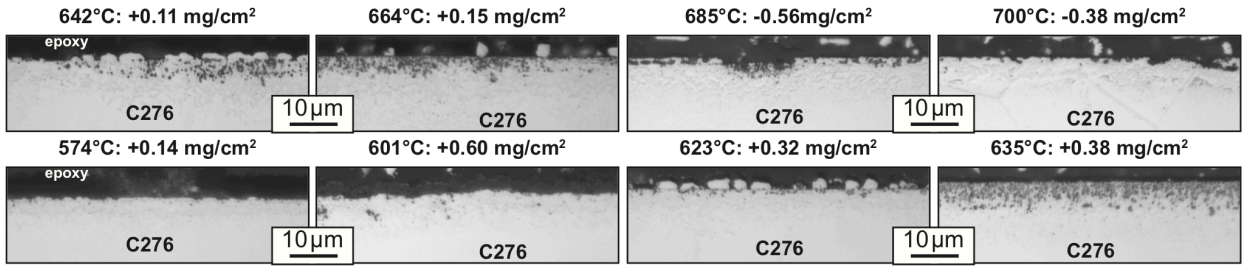

Figure 59. Light microscopy of polished cross-sections of alloy C276 coupons after 1000 h exposures in flowing dried industrial-sourced salt + 0.05%Mg identified by their estimated temperature in the hot (top row) and cold leg (bottom row).

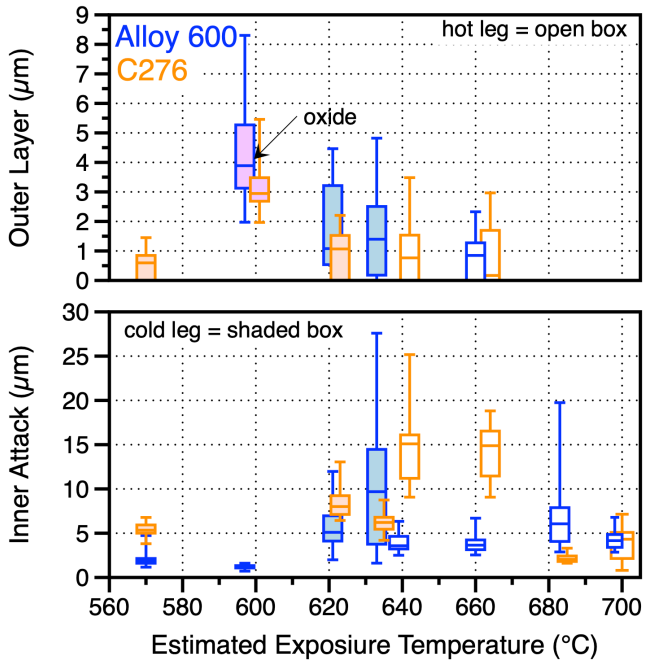

Figure 60. Box and whisker plots of the depth of attack and outer layer thickness measured for the alloy 600 and C276 coupon specimens exposed for 1000 h in dried flowing industrial-sourced salt with 0.05%Mg as a function of estimated exposure temperature. The whiskers show the maximum and minimum values measured and the boxes mark the 25% and 75% values with the median value noted.

Figures 61-64 show SEM images and associated EDX maps of several alloy 600 specimens from the HL and CL. At 683°C, Cr dissolution and Fe enrichment were evident

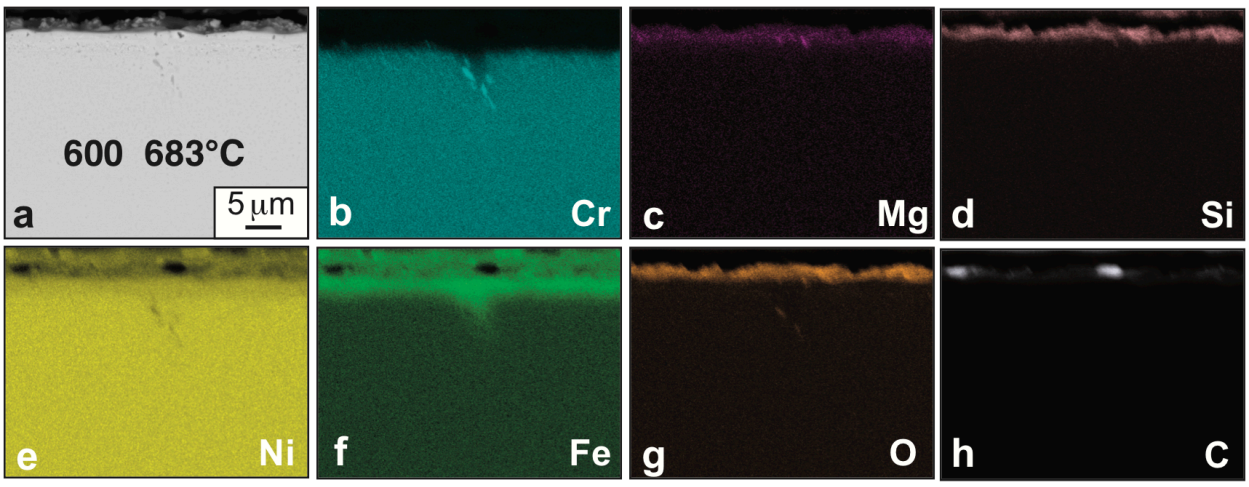

Figure 61. (a) SEM backscattered electron image of polished section of alloy 600 after 1000 h in the hot leg at ~683°C in flowing dried industrial-sourced salt + 0.05%Mg and EDX maps of the area in (a): (b) Cr, (c) Mg, (d) Si, (e) Ni, (f) Fe, (g) O and (h) C.

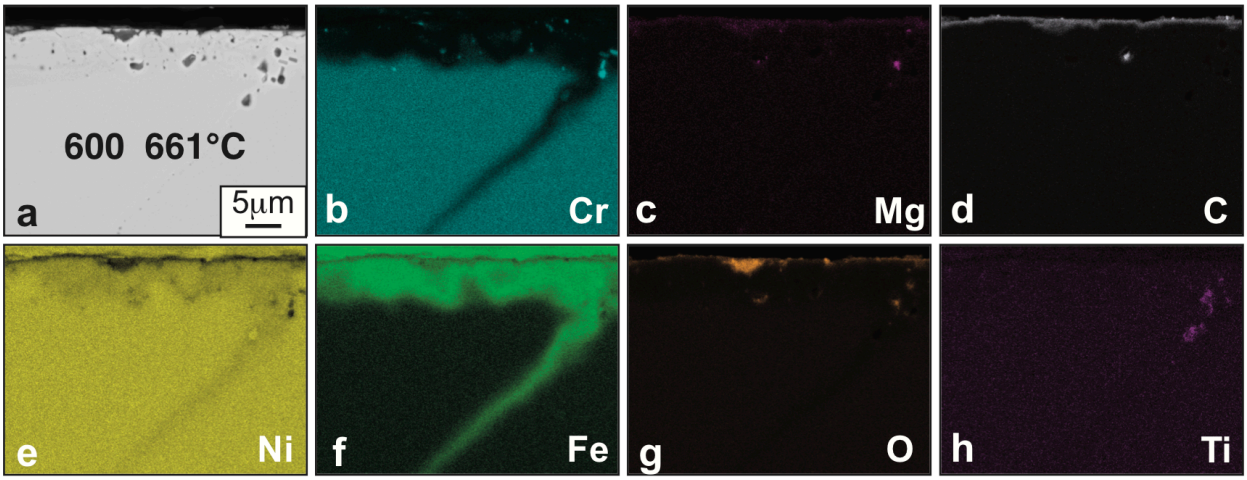

Figure 62. (a) SEM backscattered electron image of polished section of alloy 600 after 1000 h in the hot leg at ~661°C in flowing dried industrial-sourced salt + 0.05%Mg and EDX maps of the area in (a): (b) Cr, (c) Mg, (d) C, (e) Ni, (f) Fe, (g) O and (h) Ti.

but were accompanied by a thin O-rich surface layer containing Si and Mg, Figure 61. EDX line profiles from the same specimens are shown in Figure 65a and quantify the change in Cr and Fe at the surface as well as some Si enrichment. At 661°C, the specimen surface was similarly depleted in Cr and enriched in Fe, Figure 62, particularly along an alloy grain boundary where diffusion is expected to be faster. The Cr and Fe levels are shown in EDX line profiles in Figure 65b. In this case, a C- and O-rich layer was observed with less Mg detected. Precipitates on the grain boundary were Ti-rich, Figure 62h. In the CL at 633°C, the Cr depletion was not as uniform but the O-rich layer was more evident in the EDX maps in Figure 63. The line profiles from this specimen

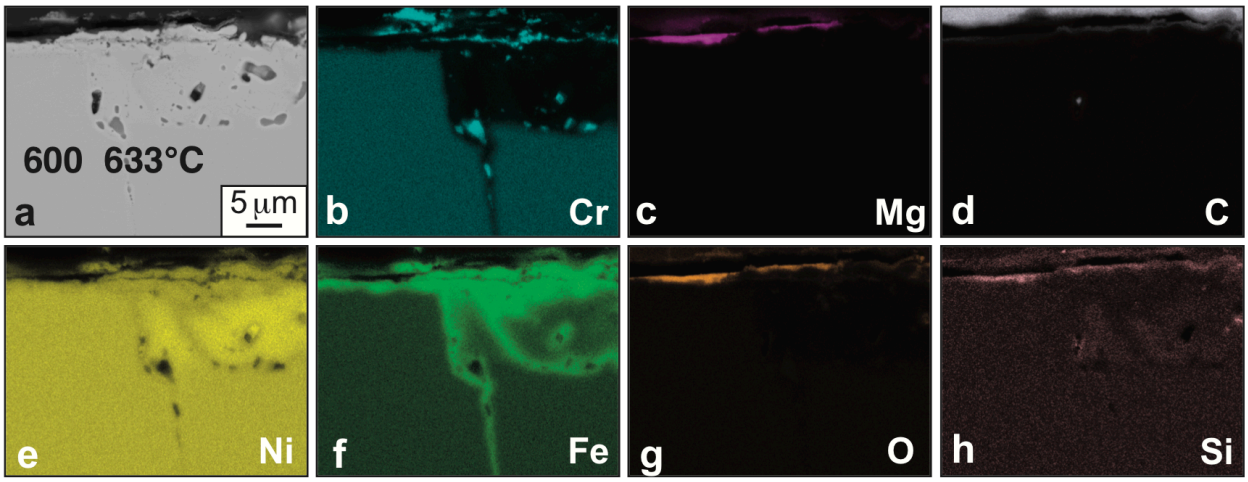

Figure 63. (a) SEM backscattered electron image of polished section of alloy 600 after 1000 h in the cold leg at ~633°C in flowing dried industrial-sourced salt + 0.05%Mg and EDX maps of the area in (a): (b) Cr, (c) Mg, (d) C, (e) Ni, (f) Fe, (g) O and (h) Si.

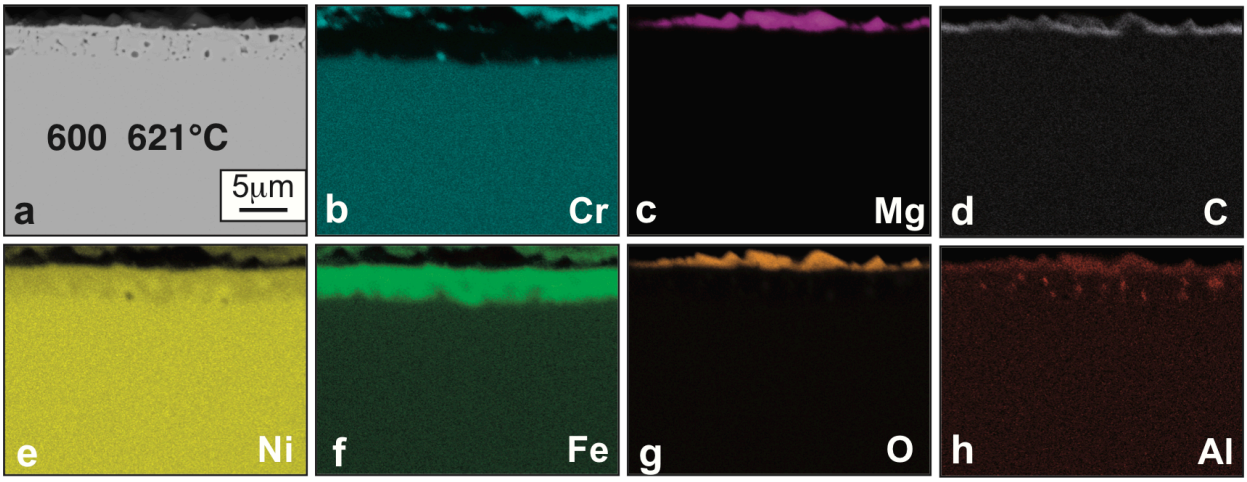

Figure 64 (a) SEM backscattered electron image of polished section of alloy 600 after 1000 h in the cold leg at ~621°C in flowing dried industrial-sourced salt + 0.05%Mg and EDX maps of the area in (a): (b) Cr, (c) Mg, (d) C, (e) Ni, (f) Fe, (g) O and (h) Al.

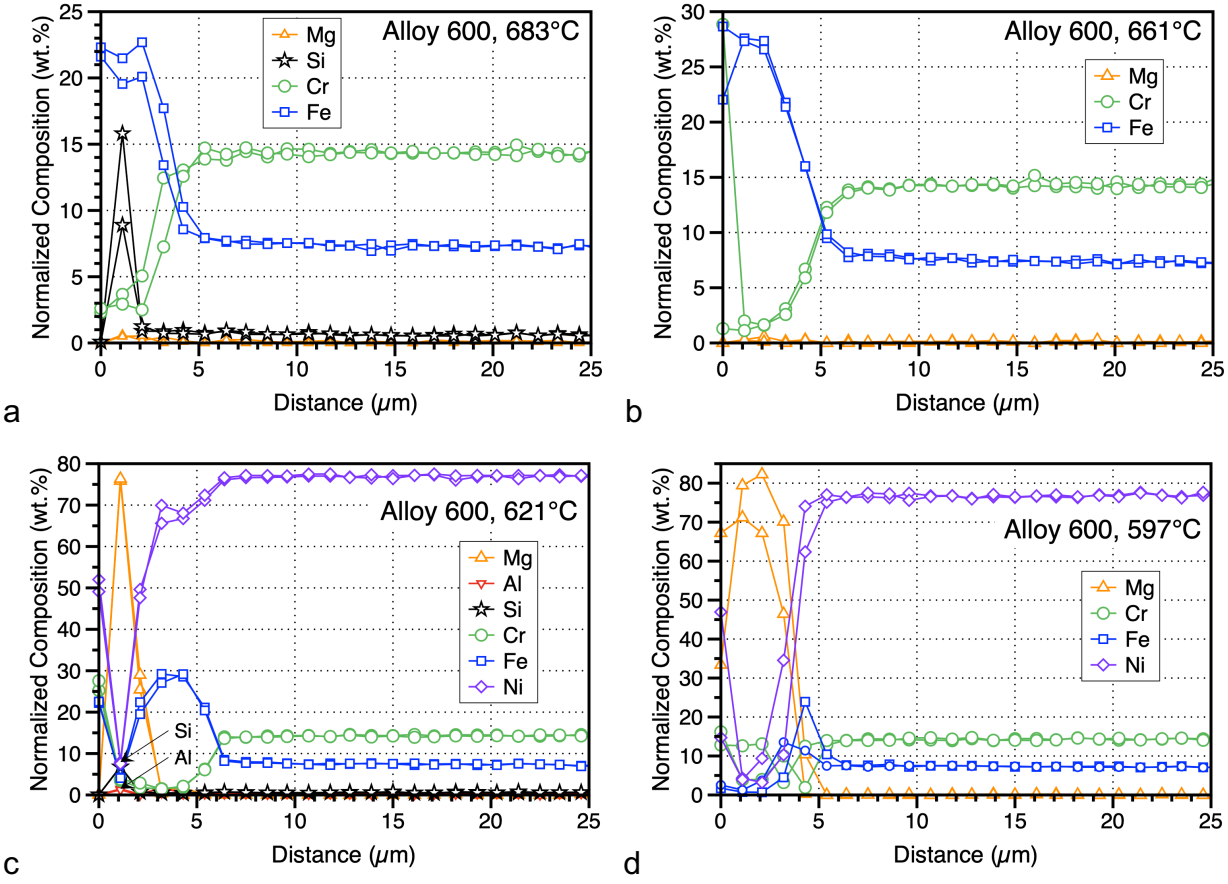

Figure 65. EDS line profiles from alloy 600 coupon specimens exposed to dried industrial-sourced salt for 1000 h at estimated temperatures of (a) 683°C HL (hot leg), (b) 661°C HL, (c) 621°C CL (cold leg) and (d) 597°C CL.

showed a very high Mg level in one case but still significant Cr depletion and Fe enrichment at the surface, Figure 65c. The specimen exposed at 621°C in the CL also showed Fe enrichment and a thicker O-rich surface layer, Figure 64. Figure 65d shows the very high Mg levels detected and less Fe enrichment and Cr depletion beneath. The strong surface Fe enrichment in these specimens suggests that some Ni may have been removed as well as Cr but it may be simply due to Cr loss.

Less characterization was conducted on the C276 specimens as the project was concluding. Figure 66 shows EDX line profiles from two coupon specimens shown in Figure 59. Similar to the alloy 600 specimens, there was Fe enrichment and Cr depletion in both the HL specimen exposed at 700°C and in a CL specimen exposed at 635°C. For this alloy, Mo and W were enriched at the surface to some degree. Also, Mg enrichment was observed for the CL specimen where an O rich layer formed. While only a few line profiles were measured for C276, the depth of Cr depletion was actually deeper at 635°C than at 700°C, perhaps because of faster diffusion at the higher temperature resupplied Cr from the bulk of the specimen. Diffusion simulations are needed for further study.

All of the tensile specimens were broken after exposure at room temperature and the results are summarized in Figures 67 and 68 and plotted versus the estimated exposure temperature. As with the mass change data, the results from the previous TCL experiment (Figure 40) are included for comparison along with as-received values in the shaded areas in each case. For alloy 600 in Figure 67, only slight drops in YS and UTS were noted after exposure. Perhaps slightly lower UTS values were observed compared to the first TCL experiment but very similar YS values were measured. In Figure 67b, the total elongation was decreased to a larger degree than in the previous experiment but still retained 35-50% ductility.

Figure 68 shows similar room temperature tensile data for the C276 specimens compared to baseline data for unexposed C276 (shaded areas). In general, the as-received UTS and YS are higher for this alloy (due to the Mo/W solution strengthening) but the post-exposure values appear to decrease with increasing estimated exposure temperature. In

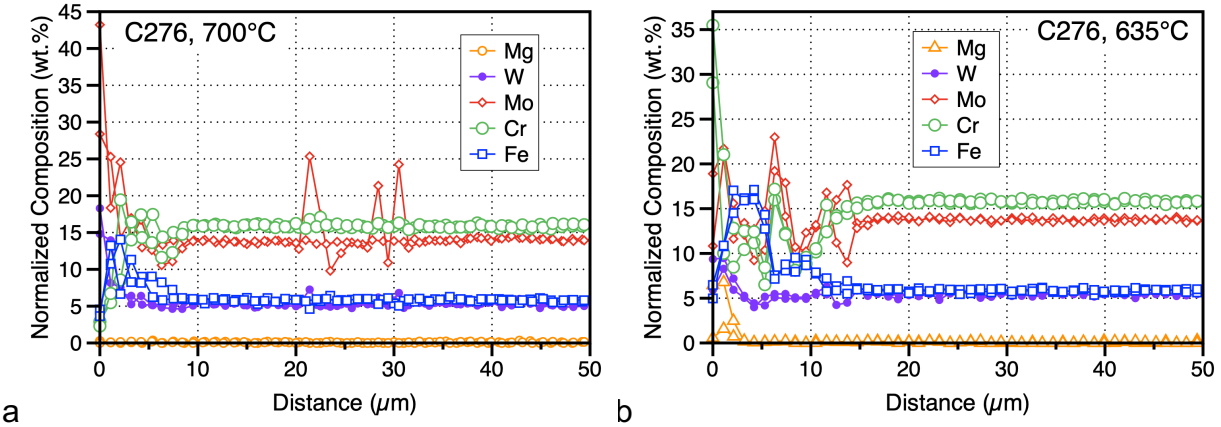

Figure 66. Two EDS line profiles from C276 specimens exposed to dried industrial-sourced salt for 1000 h at estimated temperatures of (a) 700°C HL and (b) 635°C CL.

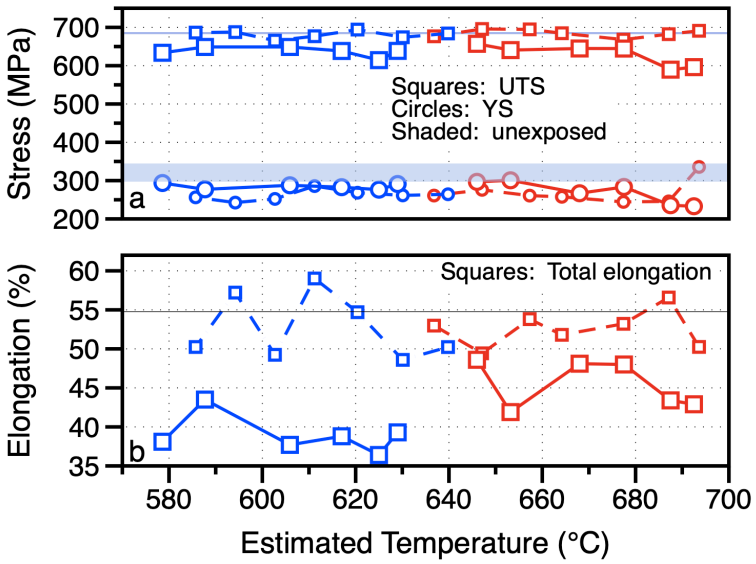

Figure 67. Room temperature tensile properties with a 10^{-3} s^{-1} strain rate for alloy 600 specimens after 1,000 h exposures in flowing dried industrial-sourced salt + 0.05%Mg identified by their estimated temperature in the hot leg (red) or cold leg (blue). (a) 0.2% yield stress (YS) and ultimate tensile stress (UTS) and (b) total elongation. The shaded regions show the range of values for unexposed alloy 600 specimens. The dashed lines are data from the Task 1.2 loop.

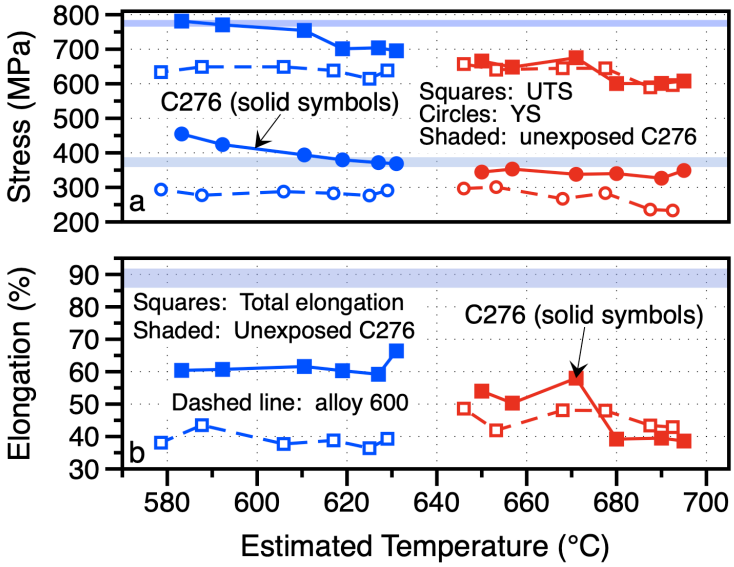

Figure 68. Room temperature tensile properties with a 10^{-3} s^{-1} strain rate for C276 specimens after 1,000 h exposures in flowing dried industrial-sourced salt + 0.05%Mg identified by their estimated temperature in the hot leg (red) or cold leg (blue). (a) 0.2% yield stress (YS) and ultimate tensile stress (UTS) and (b) total elongation. The shaded regions show the range of values for unexposed C276 specimens. The dashed lines are data for alloy 600 specimens from Figure 67.

particular, the total elongation dropped significantly, especially at the highest exposure temperatures. However, even the lowest values are ~40% ductility so this is not cause for concern. Unfortunately, time and budget constraints did not allow a better baseline comparison to be developed. Vacuum anneals at 600°-700°C would provide some information on how these material react to the 1000 h thermal exposure, independent of the environmental effects. For example, the drop in C276 ductility after exposure in Figure 68, may be a result of thermal embrittlement rather than the salt environment.

Finally, returning to Table 9, the salt chemistry was measured after the loop was operated. It was interesting to note that the Cr, Ni, Mn and W levels increased after exposure indicating dissolution. The W may be from the W rods of the sensor which are periodically cleaned during operation. The S and possibly the Al levels decreased suggesting a possible reaction with the metallic components. The Fe level in the salt did not change but many of the specimens showed Fe enrichment at the surface, which may be explained by both Cr and Ni being selectively attacked in alloy 600, leaving behind an Fe-rich surface. Thermodynamic modeling of activities and relative diffusivities is needed to understand the post-exposure line profiles.

Significant Accomplishments and Conclusions

During this two year project, considerable progress was made in understanding chloride salt compatibility. Contrary to the recent literature, low mass losses could be achieved for Ni-based alloys 600 and C276 after 1000 h flowing salt experiments at ~560-700°C and the performance metric was met. Contrary to the older MSRE literature, good compatibility was observed for both commercially-sourced KCl-$MgCl_2$-NaCl salt that was purified to low O levels and salt that was dried and still contained relatively high O content. The low attack results with dried salt suggest that H_2O (or OH^-) is the main impurity that needs to be controlled for compatibility to 700°C. Overall, the success is attributed to a return to the MSRE paradigm of focusing on salt handling, impurity control and lowering the Cl potential. In all of the flowing experiments, Mg was added to the salt. In earlier capsule experiments without Mg, significantly more attack (including pitting and Cr depletion) was observed. This is a good example that the observations from the isothermal experiments (crucibles and capsules) also were critical to the success. These experiments along with the thermodynamic calculations and additional exposures showed the importance of the container material and not relying on mass change to quantify the attack. Many of the results point to the importance of solubility and thus the need for flowing experiments with a temperature gradient to truly understand salt compatibility.

As noted above, the project pivoted in the second year from purified (i.e. low O) industrial-sourced salt to dried (low H_2O) salt. However, the purified salt result created an important baseline to compare the later results. In particular, the 0.04%Mg addition to the purified salt left no significant Mg or O deposition to the specimens in the Task 1.2 and 1.3 flowing experiments and very limited attack in the cold leg. However, with the dried salt, Mg and O deposits were observed along with Cr depletion in the majority of the coupons analyzed from Task 2.2.

These successful flowing experiments may help to change the general perception of chloride salts as being too corrosive for the Generation 3 CSP application. However, a handful of experiments are not sufficient to answer all of the important questions. Nevertheless, these results can change the focus of future work. Now that 700°C appears possible, higher temperatures can be a new goal. With this methodology, the materials exist to build a series of TCL experiments using 740H tubing to test compatibility at 700° and even 800°C, if warranted.

The TCL experiments also provided a test bed for successfully deploying the ANL sensor. While not described in this report, the sensor was successful in noting the ingress of impurities and the onset of Cr in the salt. The gasket leak in the last TCL experiment also confirmed that salt leaking out of the loop is likely far more corrosive than salt inside the loop. The lid of the pot where the gasket leaked was significantly damaged with more metal wastage observed (Figure 54).

The alloy C276 loop that was built in Phase 1 was not operated in Phase 2 where additional tasks were eliminated due to overspending in Phase 1. Thus, only a limited amount of corrosion data for C276 was generated in this project relevant to the pumped loop being built at ORNL using C276. Also, the TCL experiment with a peak temperature of 750°C only operated for ~110 h before failing. The mass changes were similar to the 1000 h/700°C experiment suggesting an increased rate of attack with increasing temperature. However, considerably more work is needed to understand the effect of temperature in Cl salt compatibility for this application.

Publications

B. A. Pint, J. W. McMurray, A. W. Willoughby, J. M. Kurley, S. R. Pearson, M. J. Lance, D. N. Leonard, H. M. Meyer, J. Jun, S. S. Raiman and R. T. Mayes, (2019) “Reestablishing the paradigm for evaluating halide salt compatibility to study commercial chloride salts at 600°-800°C,” Materials and Corrosion, 70 (2019) 1439-1449.

B. A. Pint, S. S. Raiman and J. R. Keiser, “Lifetime modeling for a supercritical CO_2-molten salt CSP power block,” AIP Conference Proceedings 2126 (2019) 160005; presented at SolarPaces 2018, Casablanca, Morocco, Oct. 2018.

Path Forward

While these results may have changed the perception of chloride salts as being “too corrosive” to use, the next phase of experiments needs to establish an engineering basis for operation including determining degradation kinetics as a function of temperature for the leading structural materials. Since only one time was operated at each condition, no kinetic rate law could be determined to extrapolate these results to longer operating times. Unfortunately, the 750°C TCL experiment only ran for ~110 h, limiting the information learned from that experiment. Also, the third TCL experiment with the dried salt in Phase 2 had several differences from the Phase 1 experiments: different salt chemistry and purification process, the addition of a Mg coupon in the

flowing salt and the gasket leak, which possibly allowed some air ingress. Thus, there is still uncertainty about how these variables affected the final observation.

New project tasks are recommended to address:

(1) Quantifying the effects of salt composition (e.g. NaCl content), impurities (e.g. O, OH, Br, S content) and additives (e.g. Mg in the salt vs. solid additions (rod or coupon)). For example, running a flowing test with and without a Mg coupon.

(2) Reliable salt chemistry measurements. A task is needed to develop a standard procedure for measuring the salt chemistry and impurities, including Br, S, O and OH, followed by round robin testing to assure accuracy. The industrial salt vendors appear to have exceptional capabilities to measure ppm levels of impurities in Cl salts.

(3) Materials for 800°C salt compatibility. No compatibility work has been conducted on alloy 740H and very little has been performed on low Cr alloys (e.g. Figure 24a). Higher temperature alloys are typically γ' strengthened and contain Al and Ti, which are more stable chlorides than Cr (Figure 1a) and may be selectively attacked. Also, high Cr alloys have a higher Cr activity and are more susceptible to deeper attack than lower Cr alloys (e.g. Figure 24a).

(4) Thermodynamic and kinetic (diffusion) modeling. To further understand the EDX line profiles (Figures 65 and 66) and support #3 above, thermodynamic and kinetic modeling is needed to understand the relative activities of, for example, Ni, Cr and Fe, to understand if the Fe enrichment is due to only Cr dissolution or if Ni dissolution also occurs.

References

J. Ambrosek, (2011) “Molten Chloride Salts for Heat Transfer in Nuclear Systems,” Ph.D. Thesis, University of Wisconsin, Madison, WI, 2011.

S. Boghosian, A. Godo, H. Mediaas, W. Ravlo, T. Ostvold, (1991) “Oxide Complexes in Alkali Alkaline-Earth Chloride Melts,” Acta Chem. Scand. 45 (2), 145-157.

R. W. Bradshaw, (1987) “Thermal-Convection Loop Study of the Corrosion of Incoloy 800 in Molten $NaNO_3$-KNO_3,” Corrosion 43(3), 173-178.

G. S. Chen, I. W. Sun, K. D. Sienerth, A. G. Edwards, G. Mamantov, (1993) “Removal of Oxide Impurities from Alkali Haloaluminate Melts Using Carbon-Tetrachloride,” Journal of the Electrochemical Society 140 (6) 1523-1526.

J. H. DeVan, (1979) “Compatibility of Structural Materials with Fusion Reactor Coolant and Breeder Fluids,” Journal of Nuclear Materials 85-86, 249-256.

W. Ding, H. Shi, Y. Xiu, A. Bonk, A. Weisenburger, A. Jianu, T. Bauer, (2018) “Hot corrosion behavior of commercial alloys in thermal energy storage material of molten $MgCl_2$/KCl/NaCl under inert atmosphere,” Solar Energy Materials and Solar Cells 184, 22–30.

L. F. Epstein, (1957) “Static and Dynamic Corrosion and Mass Transfer in Liquid Metal Systems,” Liquid Metals Technology, Chem. Eng. Prog. Symp. Ser. 20, 53, 67-81.

J. C. Gomez-Vidal, A. G. Fernandez, R. Tirawat, C. Turchi, W. Huddleston, (2017) “Corrosion resistance of alumina-forming alloys against molten chlorides for energy production. I: Pre-oxidation treatment and isothermal corrosion tests,” Solar Energy Materials and Solar Cells, 166, 222-233.

P. N. Haubenreich and J. R. Engel, (1970) “Experience with the Molten-Salt Reactor Experiment,” Nuclear Applications and Technology, 8(2), 118-136.

J. E. Indacochea, J. L. Smith, K. R. Litko, E. J. Karell, (1999) “Corrosion performance of ferrous and refractory metals in molten salts under reducing conditions,” Journal of Materials Research 14, 1990-1995.

M. Ito and K. Morita, (2004) “The solubility of MgO in molten $MgCl_2$-$CaCl_2$ salt,” Mater. Trans. 45, 2712-2718.

J. R. Keiser, J. H. DeVan and E. J. Lawrence, (1979) “Compatibility of Molten Salts with Type 316 Stainless Steel and Lithium,” Journal of Nuclear Materials 85-86, 295-298.

N. Klammer, C. Engtrakul, Y. Zhao, Y. Wu and J. Vidal, (2020) “Method To Determine MgO and MgOHCl in Chloride Molten Salts,” Anal. Chem., 92, 3598–3604. doi.org/10.1021/acs.analchem.9b04301

M. J. Lance, D. N. Leonard and B. A. Pint, (2018) “The Use of Glow Discharge Optical Emission Spectroscopy to Quantify Internal Carburization in Supercritical CO_2,” in Proceedings of the 6th International Symposium on Supercritical CO_2 Power Cycles, Pittsburgh, PA, March 2018, Paper #117.

H. Mediaas, J. E. Vindstad, T. Ostvold, (1997) “Solubility of MgO in mixed chloride-fluoride melts containing $MgCl_2$,” Acta Chem. Scand. 51, 504-514.

D. Olander, (2002) “Redox condition in molten fluoride salts: Definition and control,” Journal of Nuclear Materials 300, 270–272

T. Ostvold, (1972) “Emf-Measurements of Change in Chemical Potential of One Component on Mixing in Fused Binary Alkali-Alkaline Earth Halide Systems,” High Temperature Science 4 (1), 51.

S. J. Pawel, (2012) “Compatibility Assessment of Advanced Stainless Steels in Sodium,” Fusion Science and Technology 61:1T, 369-374.

S. J. Pawel and K. A. Unocic, (2017) “Compatibility of an FeCrAl Alloy with Flowing Pb-Li in a Thermal Convection Loop,” Journal of Nuclear Materials 492, 41-51.

B. A. Pint, S. J. Pawel, M. Howell, J. L. Moser, G. Garner, M. Santella, P. F. Tortorelli, F. W. Wiffen and J. R. Distefano, (2009) “Performance of MHD Coatings in Flowing Li at 700°C,” Journal of Nuclear Materials 386-388, 712-715.

B. A. Pint, J. W. McMurray, A. W. Willoughby, J. M. Kurley, S. R. Pearson, M. J. Lance, D. N. Leonard, H. M. Meyer, J. Jun, S. S. Raiman and R. T. Mayes, (2019) “Reestablishing the paradigm for evaluating halide salt compatibility to study commercial chloride salts at 600°-800°C,” Materials and Corrosion 70, 1439-1449.

S. S. Raiman and S. Lee, (2018) “Aggregation and data analysis of corrosion studies in molten chloride and fluoride salts,” Journal of Nuclear Materials 511, 523-535.

S. S. Raiman, R. T. Mayes, J. M. Kurley, R. Parrish and E. Vogli, (2019) “Amorphous and partially-amorphous metal coatings for corrosion resistance in molten chloride salt,” Solar Energy Materials and Solar Cells 201, 110028.

H. Sun, J. Wang, Z. Lia, P. Zhang, X. Su, (2018) “Corrosion behavior of 316SS and Ni-based alloys in a ternary NaCl-KCl-$MgCl_2$ molten salt,” Solar Energy 171, 320–329.

H. Susskind, F. B. Hill, L. Green, S. Kalish, L. E. Kukacka, W. E. McNulty and E. J. Wirsing, Jr., (1960) “Corrosion Studies for a Fused Salt-Liquid Metal Extraction Process for the Liquid Metal Fuel Reactor,” Brookhaven National Laboratory Report BNL 585 (T-146) Upton, NY (1960). And Chemical Engineering Progress 56, 57-63.

P. F. Tortorelli, (1992) "Dissolution Kinetics of Steel Exposed in Lead-Lithium and Lithium Environments," Journal of Nuclear Materials 191-194, 965-969.

K. Vignarooban, P. Pugazhendhi, C. Tucker, D. Gervasio, A. M. Kannan, (2014) “Corrosion resistance of Hastelloys in molten metal-chloride heat-transfer fluids for concentrating solar power applications. Solar Energy 103, 62–69

J. E. Vindstad, H. Mediaas, T. Ostvold, (1997) “Hydrolysis of $MgCl_2$-containing melts,” Acta Chem. Scand. 51, 1192-1200.

D. F. Williams, (2006) “Assessment of Candidate Molten Salt Coolants for the Advanced Highi-Temperature Reactor (AHTR),” ORNL/TM-2006/69, ORNL, Oak Ridge, TN.

J. P. Young, G. Mamantov, J. E. Coffield, S. Dai, (1990) “In-line Sensors for Electrolytic Magnesium Cells,” project report, Oak Ridge National Laboratory, Oak Ridge, TN.

G. Zheng and K. Sridharan, (2018) “Corrosion of Structural Alloys in High-Temperature Molten Fluoride Salts for Applications in Molten Salt Reactors,” JOM 70, 1535-1541.

Appendix A. Salt Purification Protocol of Anhydrous Carnallite (AC)

Version 5/10/2019

This protocol is aimed at providing a unified procedure for handling and purifying anhydrous carnallite at 1-5 kg scale. The goal is to ensure the quality of the purified salt in order for the Salt Collective to perform consistent corrosion tests, thermophysical property measurements, etc. Hence the material selection, furnace design, salt storage method, etc. may not be suitable for salt purification at >10 kg or >100 kg scale. For future scale-up to >100 kg, discussion with NREL's Topic 1 team is highly encouraged.

1. Store the as-received ICL anhydrous carnallite (AC) and SPK halite (from Albemarle) in an inert glove box or any airtight container, e.g., in a glove box with ultra-high-purity (UHP) N_2 or Ar (≤ 20 ppm O_2 and ≤ 10 ppm H_2O).
2. Perform ICP-MS/AES/OES analysis on AC and SPK halite to determine salt compositions. Measure at least the following elements[1]: Na, K, Mg, Br, Ca, Fe, Cr, Mn, Ni, Zn, Cu, P, S (or SO_4^{2-}), As, Sr, Si, and Mo. These elements are relevant based on ICP measurements from ICL and NREL (see Table 2 at the end of this document) and because of the use of quartz and/or Mo components. If your ICP instrument cannot measure SO_4^{2-} and Br^- content, ion chromatography can be used. Perform titration to determine initial MgOHCl content (Titration procedure sent by NREL). Perform a separate vacuum-drying process for 2 h at 150°C using 5-10 g of as-received salt to estimate the content of physically absorbed moisture.
    a. Samples for these measurements should not come from directly taking a few grains of AC salt. Mortar and pestle at least 25 g of AC randomly picked from the inventory. After thorough mixing, sample from the mixture for measurements.
3. Quartz crucible will be used for purification. Clean quartz crucible with ethanol, isopropanol, or acetone before use. Large volume quartz crucible[2] can be sourced from AdValue Technology and Technical Glass Product.
4. Purification vessel setup:
    a. Figure A1 gives the schematic of the purification vessel showing the crucible with salt, locations of gas sparger, gas inlet and outlet. A zoom-in of gas outlet design is shown in Figure A2.
        i. The sparger is made of Mo or quartz[3] with

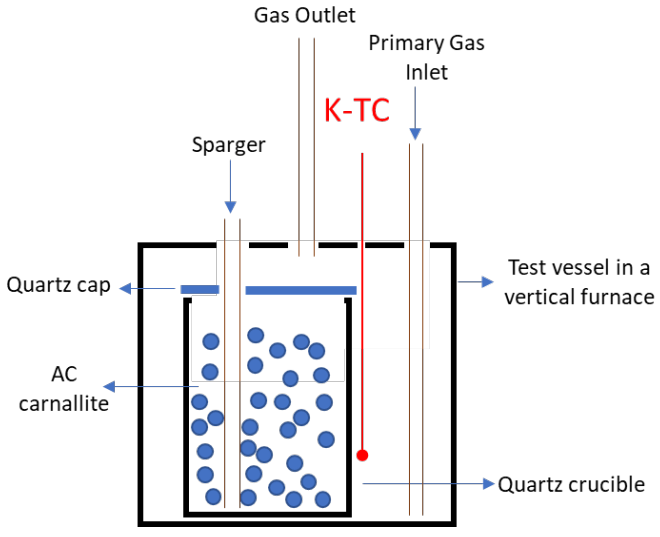

Figure A1 Schematic of the test vessel. Not to scale.

[1] Certain ICP-MS/AES/OES gives a large number of elements for each sample.
[2] For example, NREL sourced a 6-inch OD by 14-inch height (i.e., >6 L in volume) quartz crucible from AdValue for $315. The lead time was ~50 days because the crucible was custom-made to fit NREL's furnace vessel. Crucibles with smaller volume or non-custom dimensions might be shipped faster.
[3] Please remember to use ICP to check either Mo or Si if using either material for the sparger.

size compatible with the furnace port (ideally 1/8 inch OD or larger). Mo tubing can be sourced from Eagle Alloys https://www.eagleralloys.com/molybdenum/. Quartz can be sourced from AdValue Technology and Technical Glass Product. The sparger will remain in the salt until furnace cooldown starts. Sparging inside molten salt has been observed to be effective at carrying out HCl gas during purification in a recent experiment at NREL. As a precaution, a desiccator should be used to pre-dry inlet gas. The inlet gas of Ar or N_2 should be of at least UHP grade (i.e., ≤1 ppm moisture and oxygen). Since Mo can oxidize above 550°C and Mo oxide is highly volatile, low oxygen level must be ensured by performing a leak check (step 6d) of the test vessel and the section of Mo tubing exposed to air just outside the furnace should be cooled (by cooling fans, for example).

ii. The primary gas inlet is made of stainless steel 316 (or other compatible metals) with size compatible with the furnace port (ideally 1/4 inch OD or larger). A desiccator should be used as a precaution to pre-dry inlet gas (it can be the same desiccator use for sparging gas). The inlet gas of Ar or N_2 should be of at least UHP grade (i.e., ≤1 ppm moisture and oxygen).

iii. The gas outlet is made of stainless steel 316 (or other compatible metals) with size compatible with the furnace port (ideally 1/2 inch OD or larger).

iv. Other than the thermocouple(s) that controls the furnace, at least one more thermocouple (type-K or other high-temperature, chemically resistant type) should be inserted inside the test vessel and as close as possible to the outside of quartz crucible to record salt temperature. Use thermocouples that are sheathed in chemically resistant metals (such as Inconel) or ceramics. Do not use bare thermocouple wires without protection. Thermocouple sheathed in a closed-one-end Mo tube or quartz tube can be placed directly inside the salt to have better temperature measurement. This thermocouple needs to be pulled out before salt solidification starts.

v. A crucible cap (with a hole to insert the sparger) made of quartz should be used to prevent reflux and dripping of corrosion products back into the salt melt. If machining on quartz is not available, other compatible materials (such as a Ni plate or a refractory plate) can be considered since the cap is not in direct contact with the salt.

b. Gas outlet: to avoid condensation of corrosive species such as HCl at the gas outlet, heating tape wrapped around the metal tube should be used.

i. The metal outlet tube should be as short as the furnace setup allows to minimize possible exposure to corrosion while

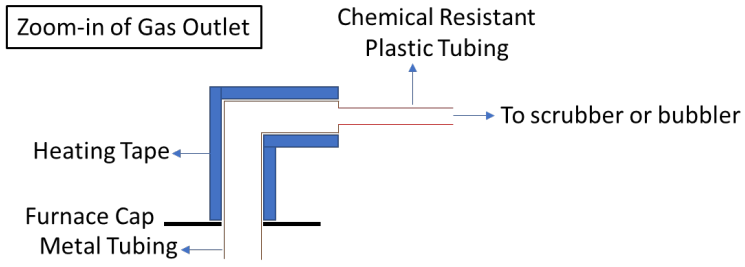

Figure A2 Schematic of the recommended gas outlet design to avoid excessive condensation of corrosive species. Not to scale

ensuring the connection between the metal outlet tube and plastic tubing (see below) remains below 200°C. The goal is to keep HCl above its boiling point of 108°C everywhere in the metallic tube using the heating tape until HCl gas transitions to the chemically resistant plastic tubing.

ii. Chemical resistant plastic tubing (e.g. PFA, PTFE) should be connected to the metal tubing. Optional heating tape can be used around the plastic tubing until the gas species is collected in a scrubber or bubbler. If a bubbler is used, make sure the gas flow rate (see step 6f) is on the high side to prevent back diffusion of solvent (especially for aqueous-based solution).

5. Weigh AC salt, SPK halite and Mg before purification
    a. AC loading: load as-received AC without grinding. Each grain of AC salt is >2 mm.
    b. Mg recipe: 2.5 g of Mg for each 1 kg of AC salt. Mg can be either chips or wafer. If using chips, they can be purchased at Sigma-Aldrich (e.g., 99.98% trace metals basis, 6-35 mesh, part # 245118-250G). If using wafer, it will be provided by SRNL (contact Brenda Garcia-Diaz brenda.garcia-diaz@srnl.doe.gov or Luke Olson Luke.Olson@srnl.doe.gov).
    c. Halite recipe: 65 g of SPK halite for each 1 kg of AC salt.
6. Purification procedures:
    a. Make sure the test vessel is clean and dry before purification. A bakeout of the test vessel under vacuum (< -25 inHg or -0.085 MPa) at 700°C for 1 h prior to purification is recommended.
    b. Load AC salt, Mg and SPK halite into the quartz crucible in the inert glove box.
    c. Quickly transfer loaded salt/crucible to furnace vessel. Minimize exposure time of salt to ambient atmosphere (including loading of crucible/salt, closing and sealing of vessel, etc.).
    d. With crucible cap, sparger, thermocouple(s) and gas inlet in place, close the test vessel and leak check. One example method to check for leakage is to vacuum or pressurize the vessel and see if vessel can hold the pressure. Other methods[4] include He sniffer if the lab has the equipment, as well as liquid leak detectors such as Snoop©.
    e. Vacuum to < -25 inHg (-0.085 MPa) and refill the vessel with UHP or higher-grade nitrogen (or Ar) at least three times before next step.
    f. Flow cover gas through primary gas inlet at >500 sccm and through sparger at 150 sccm with a vessel pressure at 1 psig (pressure above ambient[5]) for at least

[4] These methods all have different sensitivities and not all labs have the same equipment. The procedure for leak check is therefore aimed at providing a guideline that requires a step for leak check and repair of your furnace setup with your best effort if a leak is detected, instead of providing an absolute required leak rate. With high flow rate given in step 6f, impact of minor leaks should be mitigated.

[5] Make sure there a pressure gauge connected to the furnace vessel. To achieve 1 psig vessel pressure, one example is to place a needle valve in the gas outlet line (away from where corrosion can occur). Adjust the valve until the pressure gauge reads about 1 psi. Manual adjustment of the needle valve may be necessary during the

30 min before heating up (step 6h). The slight over-pressure of 1 psig is used to prevent air ingress. The higher end of the flow rate range is preferred for both the primary gas inlet and sparger in order to reduce the gas residence time in the furnace. An even higher flow rate can be considered if deemed necessary in your setup. A recent experiment at NREL using high flow rate[6] to purify 350 g of AC showed almost no sign of corrosion on the furnace vessel (cap, vessel body, quartz liner, and outlet gas tube). See Figure A5.

g. The grains of as-received AC salt are >3 mm in size and weigh >500 mg each. High flow rate through the sparger should not entrain the salt grains.

h. Heating schedule: keep the flow rate of cover gas during the entire purification process. High flow rate is used to carry out HCl and water generated during purification as fast as possible to avoid corrosion at the gas outlet. If you use a different thermocouple than the thermocouple located next to the quartz crucible to control the furnace, make sure you adjust your furnace set point to achieve the actual temperature seen by the salt/Mg mixture (heating schedule below). The hold time of 3 h at 670°C was determined at NREL by performing a purification with 300-500 g of salt. For larger scale, the hold time needed may vary and it can be determined by monitoring the release of HCl. A bubbler[7] filled with 2.9 M acetic acid (pH ~4.4) as buffer solution was installed after the furnace gas outlet at NREL where a pH sensor was used to monitor the pH drop and pH plateau of the buffer during purification which indicates HCl formation and end of HCl formation (see Figure A6). NREL determined the hold time of 3 h at 670°C for ~350 g of salt using this simple setup. Therefore, it is recommended to use a similar setup to determine the true hold time with >1 kg of salt (if other than 3 h).

Table 1 Heating schedule for AC salt purification

Salt Temperature	Ramp rate	Hold Time	Note
R.T. to 120°C	The ramp rate your equipment is capable of, or 0.5-1°C/min	2 h	
120°C to 670°C*		3 h or determined by pH monitoring	Sparger should remain in molten salt
670°C to R.T.	~1°C/min	NA	Pull out sparger (and thermocouple if it's placed inside the melt) at the beginning of this step to avoid agitation Mg when Mg should settle down

*120°C instead of 100°C for physical moisture removal and 670°C instead of 650°C for Mg purification provide 20°C of margin if the sample temperature is slightly lower than the thermocouple temperature.

purification process. In case of pressure buildup due to clogging of the valve, a check valve is recommended to ensure safety.

[6] The actual rate was not available because it was out of range on the flow meter. Rough estimate is on the order of liter/min range. For a 20-h purification including slow heating, holding for 2 h, and slow cooling,

[7] Install a gas diffuser if high flow rate is used.

i. Heat the gas outlet metal tube at 110-150°C with heating tape during entire purification process. If heating tape is used for plastic tubing (e.g., PFA or PTFE which is stable at 200+°C), heat at 110-150°C during entire purification process without damaging the plastic tubing. The purpose is to keep HCl/water from condensing on the metal tube section to cause corrosion.

7. Salt removal

a. After furnace is cooled down to R.T., open the test vessel and transfer quartz crucible/salt into the inert glove box

b. The easiest way to remove large amount of salt in the quartz crucible is to carefully break the quartz crucible with a hammer.

c. Find the approximate location of the interface between the sludge and clean salt. See Figure A3 for an example of AC re-melted at 620°C for 2 h (without addition of halite and Mg and no sparging) in quartz crucible where a sludge phase can be easily identified. Cut at a location that is 2-3 times of the sludge height above the interface with a chisel or saw. Make sure not to include any sludge phase and excess Mg. 0.5 wt.% Mg is not in excess at small-scale (<10 g) as shown by NREL's experiments. For larger-scale, this amount may be in

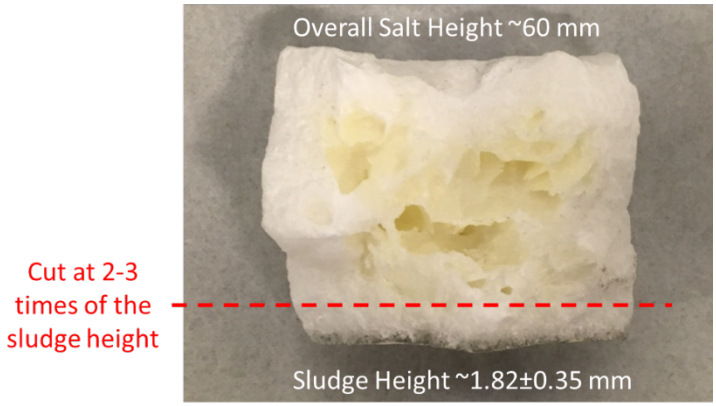

Figure A3 Example of AC salt re-melting (without addition of halite and Mg) showing sludge formation and where to cut the salt after salt purification

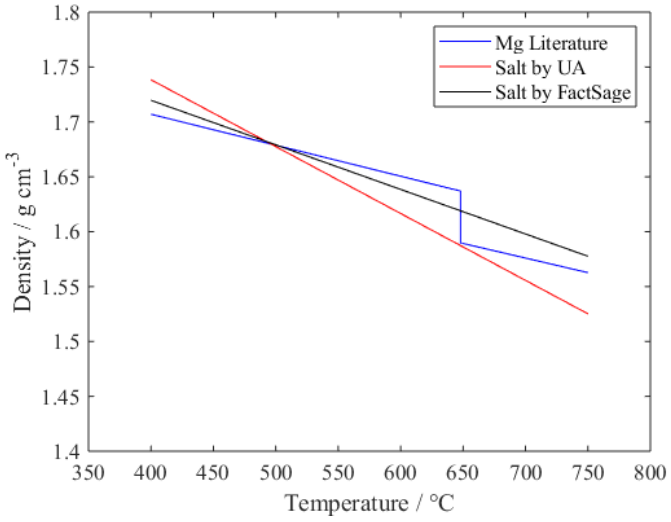

Figure A4 Density of Mg in both solid and liquid state and density of molten chlorides measured by UA and calculated by FactSage

excess. In a separate experiment at NREL with 0.5 wt.% of Mg (chips) in 350 g of AC (no sparging), excess Mg appeared at the crucible bottom as well as surface of salt. No Mg was discovered in the bulk of the salt. Hence the Mg removal may require additional cutting to remove top surface of salt too using the same margin (i.e., 2-3 times of the height of that top layer that contains excess Mg). Another experiment using 0.1 wt.% of Mg (chips) in 350 g of AC (sparging inside molten salt at 150 sccm) showed no excess Mg at either bottom or top of the salt. Only sludge was formed at the bottom. Therefore the protocol chooses 0.25 wt.% of Mg instead of 0.5 wt.% based on NREL's experiments with 350 g of AC (i.e., two experiments with 0.5 wt.% and 0.1 wt.% of Mg, respectively) and order-of-magnitude estimation based on hydrate content in AC. In case of excess Mg, cutting at a location that is 2-3 times of the sludge height should provide enough margin such that no excess Mg is included. Slow cooling rate specified in Table 1 should also help solid Mg sink to the bottom during the temperature window of 500-650°C when Mg is solid and salt is liquid. Figure A4 gives the density of Mg and molten salt. Between 400°C (i.e., the expected melting point of salt) and 500°C, solid Mg has lower density than molten chlorides which may slightly complicate the removal process. If concerns with excess Mg removal persists, Mg wafer instead of chips can be used.

d. Keep purified salt sealed in a gas-tight container in inert glove box for future use.

8. Perform ICP-MS/AES/OES to determine final salt composition and perform titration to determine final MgOHCl.
    a. Sample for MgOHCl titration should not come from taking a few grains of purified AC salt. Mortar and pestle at least 25 g of AC randomly picked from the purified salt. After thorough mixing, sample from the mixture for ICP and titration.

Table 2 ICP from ICL and NREL on anhydrous carnallite

Salt	Source	Mg	K	Na	Br	Li	Ca	B	Fe	Cr	Mn	Ni	SO_4^{2-}	Zn	Cu	P	S	As	Sr	Oxide	H_2O
		wt %				ppm															wt %
AC	ICL	11.7	21.1	5.12	0.38				43.3		3.5	<1	193	1.55	<1						0.575
		11.4	20.8	4.9	0.39				46.2	<1	3.36	<1	203	<1							0.76
	NREL	12.02	18.58	4.64			1008.5		77.23	2.03	6.1			12.21		432.2	136.19		16		
		12.3	20.07	4.87			844.04		112.59		5.6			8.49	14.87	375.37	148.66	37	20.86		
		11.56	19.25	4.3			862.31		64.96	2.16	4.47	10.25		7.31		336.47	162.89	31.85	24.17		

Figure A5 Furnace cap after purification of 350g of AC and 1.75g of Mg with high flow rate of N_2 cover gas (no sparging inside salt) showing negligible sign of corrosion. The green residue and sign of damage on the lower right corner were corrosion damage from previous purifications.

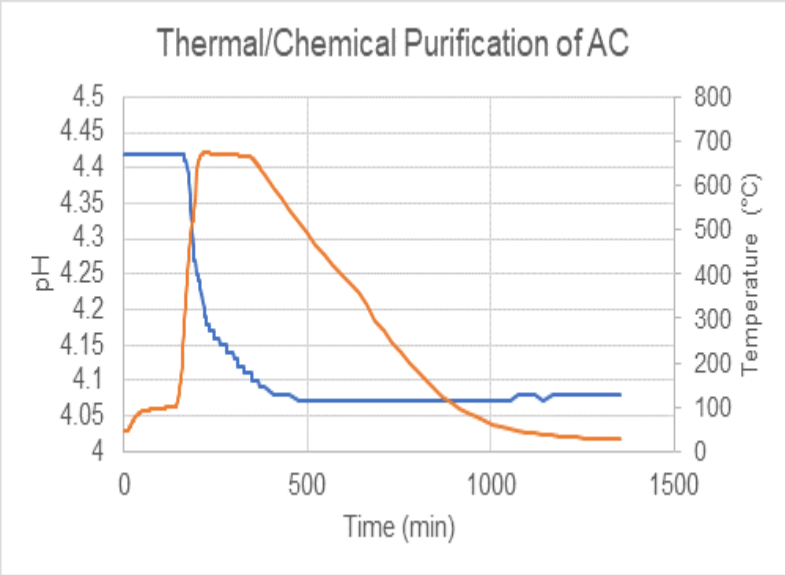

Figure A6 Variation of pH (blue) and sample temperature (orange) as a function of time during purification of 350 g of AC at NREL. Roughly 168 min is needed for the pH drop to stabilize indicating finish of HCl production, or end of purification.

Corrosion Testing Protocol

9. Prepare corrosion vessel.
    a. Use a quartz crucible with 250-500 ml total volume (e.g., FQ-1250 or FQ-2500 from AdValue Technology, or BLF300 from Technical Glass Product) and a Ni crucible cover[8] (Sigma-Aldrich Z245700-1EA) as the corrosion vessel. Crucible and cover are used as-received with no special treatment. Drill a ~3.1-mm-diameter hole at the center of the cover. Use ethanol to remove organic residues

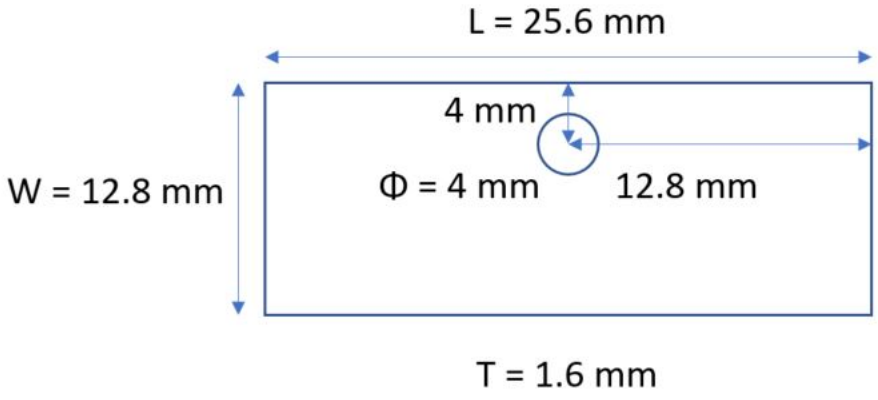

Figure A7 Schematic showing the dimensions of the machined Haynes 230 coupons

[8] Quartz cover can be used too, although machining is much more difficult.

after machining.

b. Machine Haynes 230 coupons (by waterjet cutting or EDM) into dimensions with position of a hole given by the following schematic in Figure A7. Use no special treatment on the coupons except normal ethanol cleaning after machining. Polish coupons with 120 grit sand paper with water.

c. Measure initial dimensions and record weight of each coupon. Use a scale with a minimum of four significant digits, although five or six significant digits is preferred (i.e., x.xxxxx or x.xxxxxx gram).

d. Connect three Haynes 230 coupons with a Ni wire (e.g. 99.98%, 1-mm diameter, Goodfellow NI005171) following the schematic in Figure A8 and the photo in Figure A9. Note that Figure A9 shows four coupons from a previous experiment instead of three.

e. Use an alumina tube, an alumina plate and a quartz disc (with a 3.2-mm-diameter center hole, e.g. AdValue Technology FQ-D-1N-N1/16) as described in Figure A8 to prevent electrical contact and galvanic coupling between coupons and Ni cover[9]. SRNL suggests using an alumina washer or disc instead of the quartz disc because quartz can be attacked by salt.

    i. The alumina tube should be long enough to sheath the total distance from the alumina plate to the top of the Ni hanger triangle without sliding. If the alumina tube is too short so that it slides down during corrosion test, then potential electrical contact between Ni cover and the unsheathed portion of the Ni wire can occur.

    ii. Check if there is any potential electrical contact between Ni wire and Ni cover.

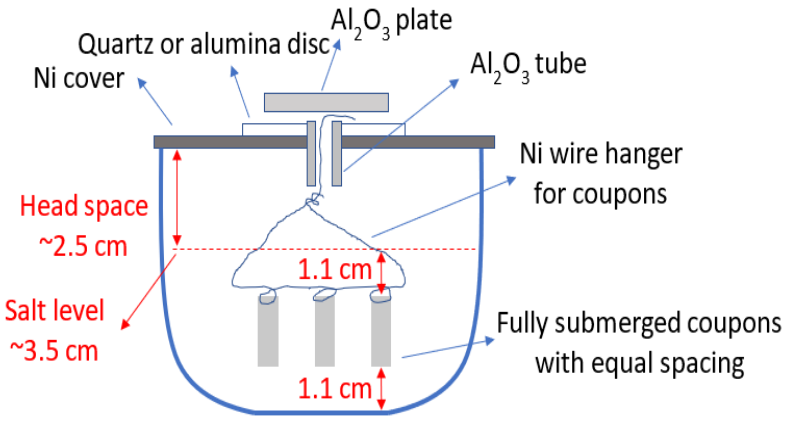

Figure A8. Schematic of corrosion test setup showing all components and spatial arrangement of metal coupons inside the corrosion vessel

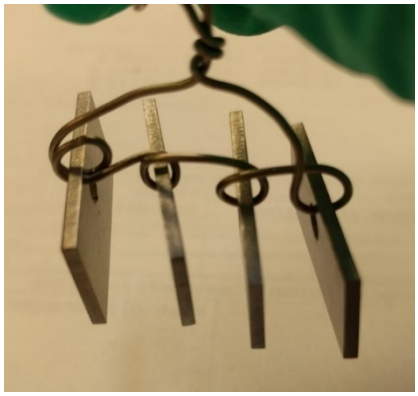

Figure A9. Picture showing the Haynes 230 coupons connected by Ni wires. Note that this picture shows four metal samples instead of three.

[9] Concerns of galvanic coupling are greatly reduced by using quartz crucible. Electrical insulation used here is a precaution.

f. In the glove box, weigh 200-250 g of salt collected from step 7d and place them around coupons in the quartz crucible (as shown in Figure A10 where a Ni crucible was used in the past). 200-250 g of salt for each corrosion test should provide ample salt volume to fully submerge three or four Haynes 230 coupons.

Figure A10. Photo showing placement of salt pieces around Haynes 230 coupons inside the corrosion vessel before corrosion test. Note that a quartz crucible is used instead of Ni crucible as shown in the picture.

g. Depending on the height of the quartz crucible you ordered, adjust the vertical position of the coupons to be about 1.1 cm from the bottom of the crucible, as shown in Figure A8, to assure full immersion of coupons and avoid contact with crucible. Headspace can vary if your crucible does not have the same dimensions as shown in Figure A8. The salt level can also vary depending on the exact amount of salt used (please use around 200-250 g). Adjust the spacing between coupons to be about 1 cm.

10. Place the corrosion vessel with coupons and salt inside a stainless-steel bag (e.g., McMaster 3438K13 or 3438K27) with a Ta foil as oxygen getter (http://beantownchem.com/products/07-ELEMENT@@2c%20ALLOY/07-TANTALUM-ZIRCONIUM/07-TANTALUM/07%20TA-THIN%20FOIL.aspx). Additional Ta foil can be used to wrap the stainless-steel bag. Fold the opening of the stainless-steel bag several times to avoid excess release of salt vapor from the corrosion setup into the stainless-steel test vessel used to host the corrosion setup.
11. Make sure the furnace test vessel is clean and dry before purification. A bakeout of the test vessel under vacuum (< -25 inHg or -0.085 MPa) at 700°C for 1 h prior to purification is recommended.
12. Transport the corrosion setup into the test vessel as quickly as possible.
    a. Make sure the corrosion setup is leveled.
    b. Place SS bag/corrosion vessel at the center of the furnace.
    c. Set up thermocouple, primary gas inlet, gas outlet following the schematic in Figure A1. No sparger is used during corrosion test.
    d. With thermocouple(s) and primary gas inlet in place, close the test vessel and leak check (as described in step 6d).

e. Vacuum to < -25 inHg (-0.085 MPa) and refill the furnace vessel with UHP or higher-grade nitrogen (or Ar) at least three times before next step.

13. Use the following heating schedule for the corrosion test shown in Table 3. All temperatures given in the following table are actual salt temperature instead of furnace control temperature. Temperature fluctuation at 800°C should be less than 10°C. Test vessel pressure is ~1 psig.

Table 3 Heating schedule for corrosion test

Temperature range, °C	Ramp rate, °C/min**	Hold time, h	Gas flow rate
RT–117	The rate your furnace is capable of, or 0.5-1°C/min	8	150 sccm
117–800		100	
800–RT	~1°C/min	NA	

14. Remove post-corrosion products

a. After furnace is cooled down to room temperature, transport the corrosion vessel with the metal coupons and salt to the glove box as quickly as possible.

b. Invert the quartz corrosion vessel with the solidified surface facing the floor and tap the vessel with a mallet. The salt should fall out with a few taps. Otherwise carefully break the quartz crucible with a hammer. Break the salt and retrieve post-corrosion coupons. Be careful not to damage the corrosion surfaces on the coupons.

Post Exposure Coupon Cleaning

1. Remove post-corrosion coupons from the Ni hanger.
2. Immerse coupons in deionized (DI) water and ultra-sonicate for 15 min to remove residual salt. Visually inspect sample and, if necessary, repeat for another 15 min.
3. After ultrasonication, rinse coupons with ethanol and allow to dry, followed by storage in an inert glove box, under vacuum or in a desiccator.
4. Measure post-corrosion dimensions and weigh coupons with the same scale used for initial weight measurement.
5. Convert weight loss to μm/year corrosion rate and mg/cm^2 based on initial coupon dimensions.

Sample Cross-Sectioning and Preparation for Scanning Electron Microscopy/Energy-Dispersive X-ray Spectroscopy (SEM/EDS)

1. Use a diamond saw to cut the sample along the red dashed line shown in Figure A11. The cut surface should be about 6–7 mm from the short edge.
2. Perpendicularly mount the cut piece with cut side facing down. Polish the mounted surface to a mirror finish.

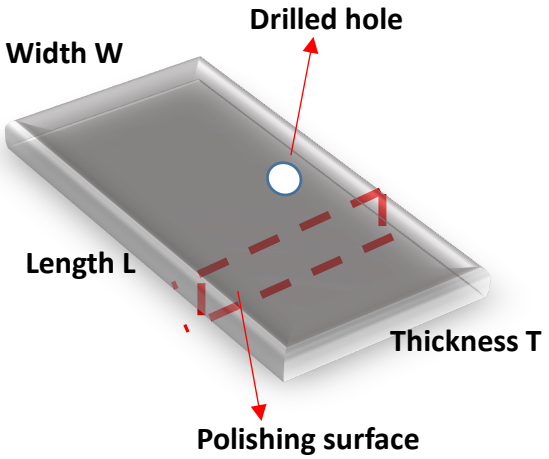

Figure A11 Schematic showing the cut and polishing surface

Cr-depletion Determination with EDS

1. Parameters for EDS analysis

a. Use >20-kV accelerating voltage.

b. EDS scan dwell times can vary, but they generally need a long enough time for sufficient counts for good statistics.

c. Do not use EDS with a variable-pressure SEM unless operating at high-vacuum setting.

d. One-minute dwell time is usually adequate for point scans. Look for the following elements: Na, K, Mg, Br, Ca, Fe, Cr, Fe, Mn, Mo, Ni, Zn, Cu, P, W, Si (which are major constituents from either the salt or the Haynes 230 coupons). Note that there is a well-known EDS peak overlap between Mo and S.

e. A minimum of one EDS point scan of the surface is needed. Three or more scans at least 10 microns away from previous scans is preferred for better statistics.

f. A sample without a coating is acceptable although a coating with carbon, Au, or Pd can be used.

g. An example of sample mounting is shown in Figure A12.

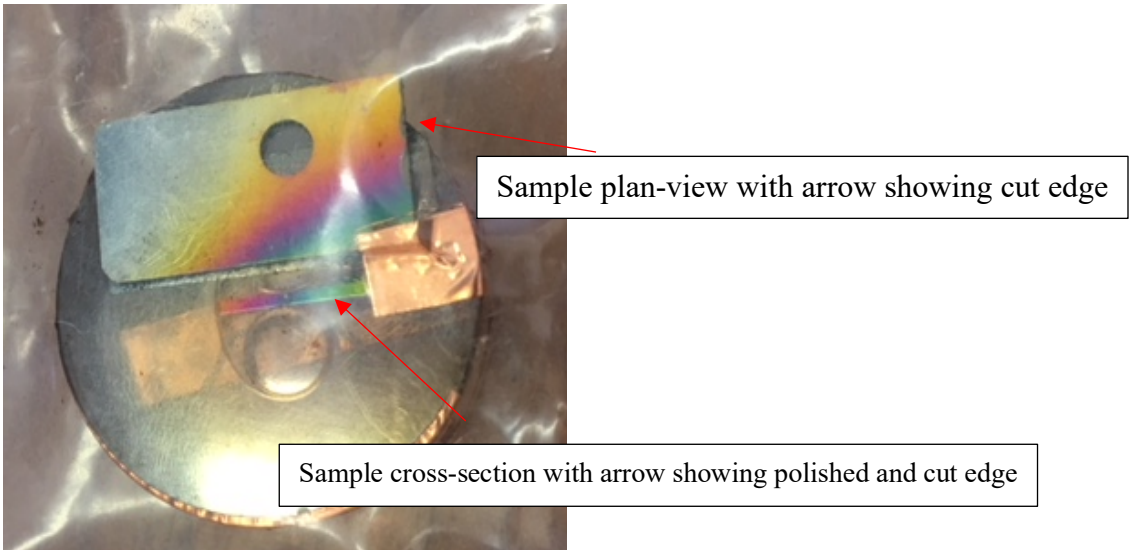

Figure A12 Mounted and polished cross-section, with plan-view sample taped on top of mount so data can all be taken during one SEM session.

2. EDS line-scans should be performed at three locations on the coupon cross-section surface as shown in Figure A13. If more than one line-scan is performed at each location, they should be at least 50 microns apart.

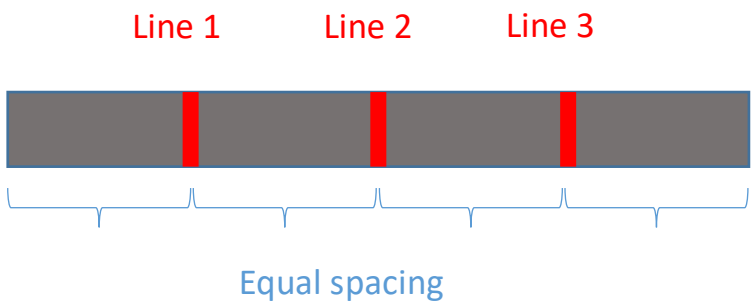

Figure A13 Schematic showing the locations of three EDS line-scans

3. If grain-boundary attack occurs, then three additional, 10-micron-long (maximum) line scans should be made over the grain-boundary region at 5 microns, 25 microns, and 100 microns into the coupon surface. This should give some quantification of grain-boundary attack.